UNIVERSITÀ DEGLI STUDI DI NAPOLI FEDERICO II

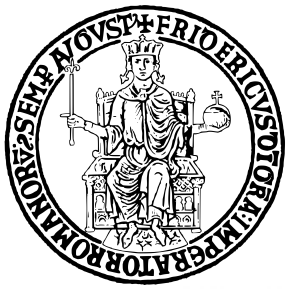

Consiglio Nazionale
delle Ricerche

Università di Camerino

PhD program in
QUANTUM TECHNOLOGIES
XXXVI cycle

Josephson currents in Superfluids and Supersolids

Settore scientifico disciplinare FIS/03

PhD dissertation by
Beatrice Donelli

Tutors
Dr. Augusto Smerzi
Dr. Luca Pezzè

Academic year 2022/2023

To my sisters Elisabetta and Eleonora

"What we need is imagination,
but imagination in a terrible strait-jacket."
R. Feynman

Contents

Introduction

Quantum mechanics behaves completely different from the classical world we are used to experience everyday. That is why macroscopic quantum effects are damnly fascinating at our eyes. Quantum gases at really low temperatures can behave contemporarly as a wave and a particle: this is the De Broglie hypothesis at the basis of the discovery of quantum mechanics [1]. At the same low temperatures and also low densities, bosons occupy macroscopically the same state, creating a Bose-Einstein condensate (BEC) [2–4], a state of matter behaving as a unique "body", whose behavior is described by a single wave-function [5–7]. These systems have provided an outstanding platform for conducting fundamental research [8–10], both from an experimental point of view, thanks to the high level of control and customization, and in theoretical terms due to the diluite and weakly interacting nature of these atomic systems, which enables accurate description. BECs are already interesting by themselves, but they also exhibit exotic properties such as superfluidity [11] and supersolidity [12]. Superfluidity consists in the ability of a fluid to flow without any friction and when stirred, it forms vortices that continue to rotate indefinitely [13]. This phenomenon combined with the properties of a solid, like the crystal periodical structure, gives rise to the supersolidity. This seems so counterintuitive that for many years was only theoretically predicted [14, 15], but now it has been observed in a dipolar BEC [16–18]. Not only it has been observed, but in this thesis we are going to study its phase coherence through the observation of the Josephson effect in it [19].

The Josephson effect is one of the most striking examples of macroscopic coherence in quantum systems [20]. This phenomenon has been observed in a wide range of experimental platforms using superconductors or superfluids connected through a tunneling junction [21–23]. In superconductors, a Josephson junction (JJ) can be created by a thin insulating barrier, a short section of non-superconducting metal, or a physical constriction that weakens superconductivity at the point of contact

[20, 21]. In liquid He, an effective JJ is obtained by an array of narrow channels in porous media whose dimensions are of the order of the superfluid healing length [24–26]. In the realm of quantum gases, both bosonic and fermionic, stable JJs can be created using repulsive optical potentials, such as a double well, with the central peak serving as the insulator in the superconducting JJ [27–29]. JJs have a wide range of applications in devices such as qubits for quantum computing [30, 31], SQUIDs for measuring magnetic fields [32] and voltage measurement [33].

In this thesis we are going to study Josephson currents in both superfluid and supersolid systems. In Chapter 1 we are going to describe the quantum states of matter known as superfluidity and supersolidity. We will start from the broader field of ultracold quantum gases following the history of quantum mechanics, thus trying to give an idea of how these phenomena were discovered and introducing also the theoretical instruments needed to derive the equations that describe their behaviours. Superfluids and their properties are described and then, with the introduction of dipolar interaction, also the history of supersolid dipolar quantum gas is developed.

Knowing the matter we are dealing with, we must know the phenomenon, so in Chapter 2 we describe the Josephson effect. We will start from its discovery in superconducting systems, following Feynman mathematical description, then extending it to superfluids and BECs. Exploring the various phenomena linked to this effect, such as the self-trapping, we will develope the theoretical modelling of it, needed for subsequent chapters.

In Chapter 3, we predict the occurrence of the Josephson effect in the absence of an external weak link within a supersolid realized with a dipolar quantum gas. It has been observed experimentally that a quantum gas already in the superfluid phase can become supersolid changing the strength of the short-range contact interaction with respect to the long-range dipolar one. This quench of the interaction induces a density modulation in the system adding the solid behaviour to it and creating zones of low density between clusters of atoms that act as self-induced weak links between adjacent reservoirs, offering support for Josephson currents. We develop a theoretical model predicting the presence of the sinusoidal Josephson current and macroscopic quantum self-trapping, analogue to the BEC case. We observe both regimes with numerical simulations and compare it with the theoretical model, discovering a novel type of Josephson junction.

Chapter 4 stems from the collaboration with the experimental group at CNR (Consiglio Nazionale delle Ricerche) in Pisa led by G. Modugno. We propose and demonstrate an innovative method to measure the superfluid fraction of a supersolid based on the Josephson effect [19]. We perform this study comparing experimental data with numerical simulations and theoretical model. The experiment is carried out on a cold-atom dipolar supersolid, for which we discover a relatively large sub-unity superfluid fraction, which was not assesed yet.

The last Chapter 5 stems from a different collaboration with the experimental group based at LENS (European Laboratory for Non-Linear Spectroscopy) in Florence, led by G. Roati. We study an atomtronic Josephson junction necklace consisting in a superfluid constrained in a ring geometry with a series of Josephson barriers [34]. Currents applied to the system by phase imprinting are found to be stabilized by the increase of the number of barriers, which is the opposite trend with respect to the superfluid fraction of the system. We predict theoretically and observe experimentally and numerically this increased stability.

1

What's the Matter: Ultracold Quantum Gases

In this chapter, we explore the fundamental concepts underlying the study of ultracold dipolar gases and their intriguing quantum behavior. Beginning from the very basics, we explore what distinguishes a gas that exhibits quantum characteristics. We then proceed to investigate the phenomenon of Bose-Einstein condensation, which is a hallmark of degenerate quantum states of matter. In doing so, we examine the short-range interactions present in Bose-Einstein Condensate (BEC). Our journey continues with an exploration of superfluidity, an essential prerequisite for the formation of supersolids. Finally, we unravel the fascinating world of dipole-dipole interactions, which give rise to distinctive features leading to the formation of supersolids.

1.1 Quantum Gases: A Dual Nature

Quantum mechanics emerged in a period of clarity in physics and revolutioned the notion of world that we had before. At the end of the nineteenth century, matter and radiation were treated as separated entities governed by completely distinci laws. The behaviour of material bodies was described by Newton's laws of classical mechanics. On the other hand, the theory of electromagnetism explained that radiation follows Maxwell equations. This division was undermined by the study

of the blackbody radiation which leds Planck to formulate the hypothesis of the energy quantization in 1900. After 5 years, Einstein generalized this idea using the discretization of energy to explain the photoelectric effect. This means that Newton was right saying that light is made of particles, now called photons. However Young, with his double-slit experiment, observed interference demonstrating that light behaves as a wave. The only solution to explain both behaviours of light is wave-particle duality. Speaking of matter, wave-particle duality for particles with non-zero mass was first postulated by Louis De Broglie in 1925 [1] and experimentally proved by Thomson in 1927 [35]. De Broglie introduced the idea that every particle of mass m and momentum p has associated a wave whose wavelength, now called the De Broglie wavelength, is given by:

$$\lambda = \frac{h}{p} = \frac{h}{mv} \tag{1.1}$$

where h is the Planck constant.

In the context of an ideal gas composed of N atoms at a temperature T, we need to define the De Broglie thermal wavelength defined as:

$$\lambda_{DB} = \frac{h}{\sqrt{2\pi m k_B T}} \quad , \tag{1.2}$$

where k_B is the Boltzmann constant. This parameter characterizes the extension of wave packets and reflects the position uncertainty associated with a thermal particle having energy $k_B T$ [36]

$$\frac{h}{\lambda_{DB}} \sim p_{rms} \sim \sqrt{2 m k_B T} \tag{1.3}$$

where p_{rms} is the root main square momentum. We can determine when a gas exhibits classical or quantum behavior by examining the phase space density, which is defined as the number of particles per unit space and momentum volume:

$$\rho \equiv n p_{rms}^{-3} \sim n \lambda_{DB}^3 \sim \frac{\lambda_{DB}^3}{d^3} \tag{1.4}$$

where $n \sim d^{-3}$ is the real space density and d is the mean inter-particle distance. If $\rho \ll 1$, meaning that wave packets are highly localized compared to the inter-particle distance, particles behave classically. Conversely, when $\rho \sim 1$, implying overlapping wave packets and indistinguishable particles, the gas displays quantum behavior. To observe quantum effects in a gas, it is necessary to increase the phase space density ρ either by increasing the real space density n or by decreasing the temperature T to enhance λ_{DB}.

1.2 Bose-Einstein Condensation

In 1924, the Indian physicist Bose proposed a novel derivation of Planck's law for black body radiation [2]. He viewed thermal radiation as a gas of indistinguishable particles (photons), thus changing the number of microscopic states corresponding to a macroscopic state. Bose sent his paper to Einstein that found his work intriguing and assisted in its publication. Moreover, Einstein made a publication predicting the emergence of a novel state of matter: a Bose-Einstein condensate (BEC) [3, 4]. Bose-Einstein condensation is a pure quantum phenomenon consisting in the macroscopic occupation of a single-particle state by an ensemble of identical bosons in thermal equilibrium at finite temperature. The key to understanding BEC is the Bose-Einstein distribution, which describes the occupation of energy states by particles. Einstein counted the microscopic states of an ideal gas of identical atoms considering them indistinguishable, as Bose did with the light quanta. The only difference was that Bose fixed only the total energy, while with atoms Einstein fixed also the total atom number which introduces an additional Lagrange multiplier, the chemical potential μ. The mean number of bosons in a state of energy ϵ_i found by Einstein is [6–9]

$$N_i = \frac{1}{\exp(\beta(\epsilon_i - \mu)) - 1} \tag{1.5}$$

where $\beta = 1/k_B T$, with k_B the Boltzmann constant and T the temperature of the gas. For a gas of N bosons, this distribution can be expressed as

$$N = \sum_i g_i N_i = \sum_i g_i \frac{z}{e^{\beta\epsilon_i} - z} \quad , \tag{1.6}$$

where g_i is the degeneracy associated to the energy ϵ_i, and $z \equiv \exp(\beta\mu)$ is the fugacity, which must be less than $e^{\beta\epsilon_i}$ to avoid negative occupation numbers. For a non-degenerate ground state ($g_0 = 1$,$\epsilon_0 = 0$), the upper limit for the fugacity is $z_{max} = e^{\beta\epsilon_0} = 1$ and the total atom number is:

$$N = \frac{z}{1-z} + \sum_{i\neq 0} g_i \frac{z}{e^{\beta\epsilon_i} - z} \equiv N_0 + N_{exc} \tag{1.7}$$

where N_0 and N_{exc} are the number of atoms in the ground state and the excited states. Note that the number of atoms in the ground state N_0 can increase indefinitely as z approaches 1, while the number in excited states N_{exc} approaches an

upper limit given by $\sum_{i\neq 0} \frac{g_i}{e^{\beta\epsilon_i}-1}$. This means that, when T and V are fixed and the total number of atoms is increased over N_{max}, the thermal cloud (N_{exc}) saturates to N_{max} and all the extra atoms occupy the ground state, forming the BEC.

The experimental realization of a BEC is done by decreasing T below a critical temperature T_C while the number of atoms N and the volume V are fixed. The value of T_C can be obtained by equating the saturation value N_{max} with the total N. For a 3D box, it gives [6–9]:

$$n \equiv \frac{N}{V} = \zeta(3/2)\left[\frac{mk_BT_C}{2\pi\hbar^2}\right]^{3/2} \tag{1.8}$$

where ζ is the Riemann zeta function and $\zeta(3/2) \simeq 2.6124$. Using the definition of De Broglie thermal wavelength Eq. (1.2), this equation can be rewritten as:

$$n\lambda_{DB}^3(T_C) \equiv \rho = \zeta(3/2) \tag{1.9}$$

recovering the condition $\rho \sim 1$ for which we have found the quantum behaviour of a gas.

For a gas of ^{87}Rb atoms at room temperature and pressure ($P = 105$Pa, $T = 300$K), the de Broglie wavelength $\lambda_{DB} \sim 0.01$nm, and the density $\rho \sim 10^{-8}$ [8]. To achieve Bose-Einstein condensation (BEC), it is necessary to increase the phase-space density ρ by eight orders of magnitude. This can be accomplished by reducing the temperature, not by increasing the particle density n. In fact, the critical temperature, as described by Eq. (1.8), is so low that under standard pressure, all known interacting systems, with the exception of helium, undergo a phase transition to the solid phase well before reaching quantum degeneracy. To avoid this transition, it is imperative to work with dilute gases. A typical BEC density is approximately $n \sim 10^{14}\text{cm}^{-3}$, which is significantly lower than, for example, the density of air at approximately $n \sim 10^{19}\text{cm}^{-3}$. In 1995, a research team led by Eric Cornell and Carl Weiman at the National Institute of Standards and Technology in Boulder successfully produced the first atomic BEC using ^{87}Rb atoms [37]. The group achieved this by cooling the gas to a few hundred nanokelvin through laser cooling techniques and then magnetically trapping it. In the same year, Ketterle and his team at MIT also achieved BEC with ^{23}Na atoms, having ten times as many atoms and 100 times higher density [38]. In 2001, Eric Cornell, Carl Wieman, and Wolfgang Ketterle were honored with the Nobel Prize in Physics for their groundbreaking work in creating and studying BECs [36, 39]. The realization of this new

state of matter marked the beginning of an interdisciplinary field of research that explores the fundamental properties of quantum fluids, such as superfluidity and superconductivity, and the potential of coherent matter waves in atom optics [6, 7] Since then, BECs have found diverse applications in the realm of scientific and technological domains, ranging from precision measurements to the development of atom lasers and quantum simulators [10, 40]. Researchers have also expanded their explorations into the domain of ultracold molecules and mixtures, thereby opening up new avenues for quantum chemistry and quantum information processing [41, 42]. BECs continue to be a captivating and pivotal area of research within the field of atomic and molecular physics.

1.3 Weakly interacting bosons

The interaction of N neutral bosons is described by a potential that is strongly repulsive at small distances because of the overlap of the electronic clouds of each atom, while it is weakly attractive at large distances due to Van der Waals interactions [9]. In a BEC, we can get under the assumption of dilute gas because the inter-particle distance is higher than the range of atoms interaction r_0:

$$d \sim n^{-1/3} \sim 200\ nm \gg r_0 \sim \text{Å}. \tag{1.10}$$

In this ultra-cold regime, scattering theory explains that only the lowest order of the scattering amplitude can be considered in the so-called Born approximation. Only s-wave scattering between atoms take place and can be fully characterized by the scattering length a_s. It is therefore admitted to replace the exact interaction potential V with a simpler pseudo-potential V_{pseudo}, written such that its first-order Born scattering amplitude reproduces the complete one. This pseudo-potential is short-range and isotropic and it can be shown to have the following expression [43]:

$$V_{pseudo}(\mathbf{r}) = g\delta(\mathbf{r}), \qquad g = \frac{4\pi\hbar^2 a_s}{2m} \tag{1.11}$$

where m is the atomic mass and $\delta(\mathbf{r})$ is the Dirac delta function. The most interesting aspect of this contact interaction is that it can be experimentally tuned and even suppressed using an external magnetic field, like the magnetic Feshbach resonances [44–47] or optical ones [44, 48–50].
This interaction gives rise to a scaling length in a BEC. Consider a BEC in a box with hard walls. At the wall, the wavefunction must go to zero but far from the

wall it has a bulk value given by the competition between kinetic and interaction energies. Calling ξ the distance over which the BEC makes this variation, we have $\hbar^2/2m\xi^2 = gn$, that is [7]

$$\xi = (8\pi n a_s)^{-1/2} \tag{1.12}$$

where n is the density. This length is the so-called *healing length*, because it describes the distance over which the wave function tends to its bulk value when subjected to a localized perturbation. For this reason, it gives also the size of the vortices that can form in the system. It needs to be smaller than any other length in the system.

1.4 Superfluidity

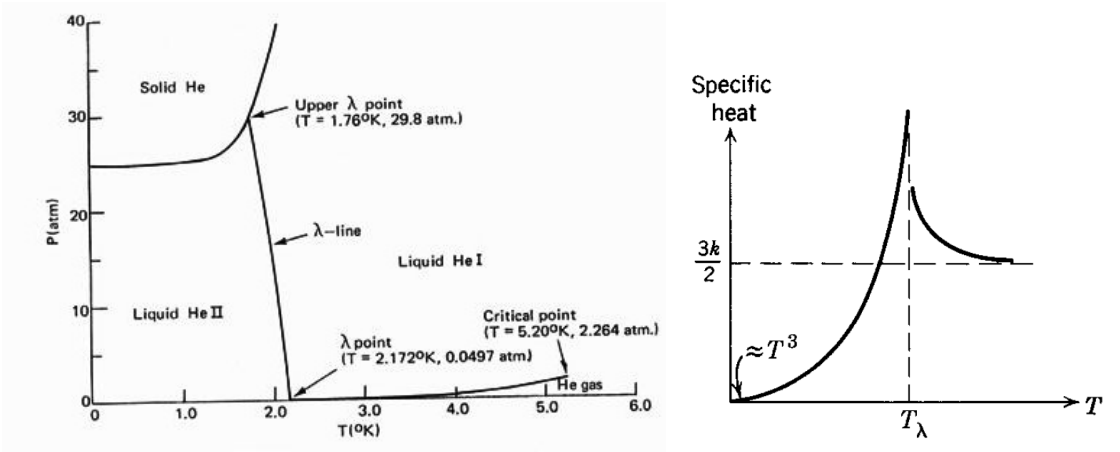

Figure 1.1: a) The phase diagram of superfluid ^{4}He, from [11]. b) The divergence of the specific heat of superfluid ^{4}He, from [51].

Superfluidity is a remarkable manifestation of quantum mechanics at a macroscopic level, characterized by the ability of a fluid to flow without friction through narrow channels. This phenomenon occurs in ^{4}He, an isotope that remains liquid even at the absolute zero temperature, as long as the pressure is kept below $25atm$. At low temperatures, the kinetic energy of the atoms becomes insufficient to confine them within lattice sites, leading to the formation of a solid in all other elements. The qualitative reason why Helium remains liquid consists in its weak internal interactions because it is a noble gas and the small atomic mass, indeed is the noble gas with the smaller one. These two factors lead to a large zero-point motion of the

atoms, which therefore does not solidify.
The phase diagram of helium is illustrated in Figure 1.1. There are two phase transitions in helium, with the liquid gas transition occurring below the temperature of $4.2K$, and another transition at a lower temperature of around $2.17K$. The specific heat of helium exhibits a discontinuity at this transition point, which is referred to as the λ point. The two phases of liquid helium are called "helium I" and "helium II". The superfluid properties of helium below the λ point were experimentally established by P. Kapitsa in 1938 [52], and independently by J.F. Allen and A.D. Misener in the same year [53]. Kapitsa also coined the term "superfluidity" and received the Nobel Prize in Physics for this discovery in 1978 [54]. [1].

1.4.1 Landau's criterion for superfluidity

In 1941, Landau proposed an explanation for the superfluid behaviour of liquid helium by treating the quantum states of the liquid as a gas of phonons with a linear dispersion relation [55]

$$\epsilon_k = \hbar k c \tag{1.13}$$

where c is the sound velocity in the medium and k is the momentum of the phonon. The main idea is that the motion of a body through helium at low temperatures excites collective quanta as phonons, similar to the vibrations of a crystal. The energy transferred from the body to the helium is not transferred to the individual atoms, but to the phonons. This phenomenon occurs under conditions where the energy transfer is favourable.
Consider a fluid at rest and a body moving through it with momentum $\mathbf{p}$. The difference in kinetic energy of this body before and after exciting a phonon of momentum $\mathbf{k}$ is

$$\Delta E_k = \frac{\mathbf{p}^2}{2m} - \frac{(\mathbf{p} - \hbar\mathbf{k})^2}{2m} = \frac{\mathbf{p}\cdot\hbar\mathbf{k}}{m} - \frac{\hbar^2\mathbf{k}^2}{2m} \tag{1.14}$$

where m is the mass of the moving body. In the reference frame moving with the phonon, the excitation energy is

$$\Delta E'_k = \Delta E_k + \frac{\hbar^2\mathbf{k}^2}{2m} = \frac{\mathbf{p}\cdot\hbar\mathbf{k}}{2m}. \tag{1.15}$$

[1] Interestingly, Kapitsa won the Nobel Prize together with Penzias and Wilson who received it for the completely unrelated discovery of the cosmic microwave background radiation

This energy needs to be higher than the linear phonon spectrum in order to be energetically favourable

$$\begin{aligned} \Delta E'_k = \frac{\mathbf{p}\cdot\hbar\mathbf{k}}{2m} \geq \epsilon_k = \hbar c k \\ vk \geq |\mathbf{v}\cdot\mathbf{k}| \geq ck \\ v \geq c \equiv \frac{\epsilon_k}{\hbar k}. \end{aligned} \tag{1.16}$$

This relation means that a body moving in a superfluid helium can excite a phonon only if it travels at a speed higher than a critical value that is the sound velocity of the fluid.
The group of W. Ketterle at MIT conducted an experiment stirring a blue-detuned laser within a BEC at varying speeds (as in Fig. 3.15a), and observed this critical velocity threshold for the initiation of dissipative flow within the condensate [56].
The whole curve of the helium dispersion relation can be experimentally measured by cold neutron scattering [57, 58] and has the following trend (see Figure 1.2 from [51]):

$$\begin{aligned} \epsilon_k &= \begin{cases} \hbar c k, & k \ll k_0 \\ \Delta + \frac{\hbar^2(k-k_0)^2}{2\sigma}, & k \sim k_0 \end{cases} \\ c &= (239 \pm 5) m/s \\ \frac{\Delta}{k_B} &= (8.65 \pm 0.4) K \\ k_0 &= (1.92 \pm 0.01) \text{Å}^{-1} \\ \sigma &= (0.16 \pm 0.01) m_{He} \end{aligned} \tag{1.17}$$

where k_B is the Boltzmann constant, m_{He} is the mass of an helium atom and k_0 is the position of the minimum where there are rotons, quasi particles which behave as particles with mass σ and require a minimal energy Δ for their creations. Unlike phonons, rotons are excitations with an energy gap Δ.

In the same way as phonons, at energies around the rotonic minimum k_0, a body moving in the superfluid loses energy by emitting one roton:

$$\begin{aligned} \hbar v k_0 \geq \hbar \mathbf{v}\cdot\mathbf{k}_0 \geq \epsilon_{k_0} = \Delta \\ v \geq v_c \equiv \frac{\Delta}{\hbar k_0}. \end{aligned} \tag{1.18}$$

Roton effects are negligible at low temperatures due to the Boltzmann factor $e^{-\Delta/(k_B T)}$, but in an intermediate interval of temperature they change the critical

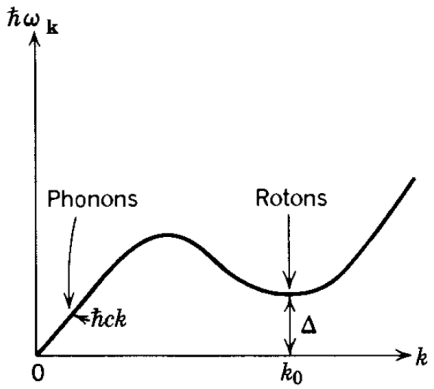

Figure 1.2: The dispersion relation of superfluid ^4He, from [51]. For small k, there is a linear trend that represents phonons, while the portion near k_0 corresponds to rotons.

velocity. In fact, considering a purely phonon spectrum the critical velocity of He is $c = 239m/s$, while when rotons are included it drops to $v_c = 58m/s$.

1.4.2 Quantized circulation and vortices

The other remarkable property of a superfluid is its quantized circulation. Consider a classical fluid with a non-zero viscosity in a rotating bucket. The velocity field is

$$v(r) = \omega r \tag{1.19}$$

where r is the radial coordinate and ω is the rotating frequency of the bucket. The integration of this velocity field along a closed path γ is

$$\oint_\gamma \mathbf{v} \cdot \mathbf{r} = \omega r \; 2\pi r|_{r=a} = 2\pi\omega a^2 \neq 0 \tag{1.20}$$

where we have considered the path along a circle of radius a centered in the middle of the bucket, see Figure 1.3a.

A superfluid, on the other hand, is described by a macroscopic wave function [6]

$$\psi(\mathbf{r}) = \sqrt{n(\mathbf{r})}e^{i\phi(\mathbf{r})} \tag{1.21}$$

where $n(\mathbf{r}) \equiv |\psi(\mathbf{r})|^2$ is the density distribution and $\phi(\mathbf{r})$ is the macroscopic phase of the superfluid. The field velocity assumes the form

$$\mathbf{v} = \frac{\hbar}{m}\boldsymbol{\nabla}\phi \tag{1.22}$$

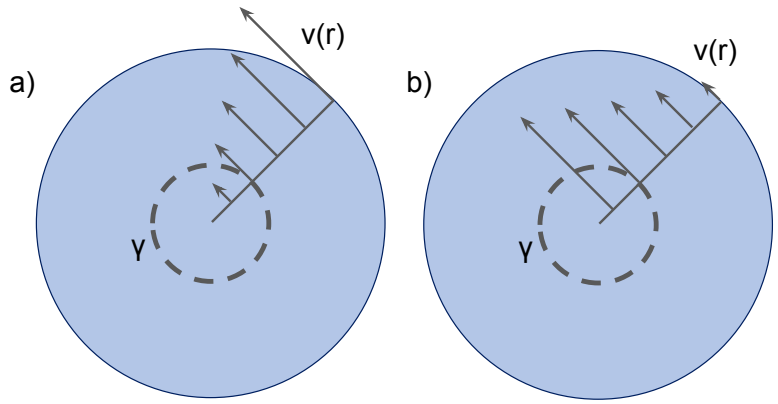

Figure 1.3: Top view of velocity fields v in a rotating bucket as a function of the radial coordinate r in case of a) normal fluid and b) superfluid. Dashed line is the path γ along which the circulation integral is performed.

where m is the atomic mass. This expression can be demonstrated from an hydrodynamic point of view writing the probability density current

$$\mathbf{J} = \frac{\hbar}{2mi}(\psi^* \boldsymbol{\nabla}\psi - \psi \boldsymbol{\nabla}\psi^*) \tag{1.23}$$

Substituting Eq. (1.21) in it, we obtain

$$\mathbf{J} = n\frac{\hbar}{m}\boldsymbol{\nabla}\phi. \tag{1.24}$$

Expressing this current as a function of the velocity $\mathbf{J} = n\mathbf{v}$, we have immediately the velocity field given in Eq. (1.22). Intuitively, we can explain it considering a plane wave with phase $\phi = k\mathbf{r}$. The associated velocity is $\mathbf{v} = \frac{\hbar}{m}\boldsymbol{\nabla}\phi = \frac{\hbar k}{m}$, that is the propagation velocity of the plane wave.
Considering the same rotating bucket, as for the classical fluid, for a superfluid the integration of this velocity field along the same closed path γ is

$$\oint_\gamma \mathbf{v}\cdot\mathbf{r} = \frac{\hbar}{m}\oint_\gamma \boldsymbol{\nabla}\phi \cdot d\mathbf{r} = \frac{\hbar}{m}\int_S (\boldsymbol{\nabla}\wedge\boldsymbol{\nabla}\phi)\cdot\hat{n}dS = 0 \tag{1.25}$$

where we have used the Stoke theorem. The last integral is performed over the surface S enclosed by γ and with normal versor $\hat{n}$. The use of the Stoke theorem needs a continuos function, thus when there is a singularity in the phase, we have

$$\oint_\gamma \mathbf{v}\cdot\mathbf{r} = \frac{\hbar}{m}\oint_\gamma \boldsymbol{\nabla}\phi \cdot d\mathbf{r} = \frac{\hbar}{m}(\phi_f - \phi_i) = \frac{h}{m}l \quad , \quad l \in \mathbb{N}. \tag{1.26}$$

The total phase difference $(\phi_f - \phi_i)$ needs to be an integer multiple of 2π because the phase must return to its same value after closing the path, otherwise the wavefunction is not single-valued. The phase singularity internal to our path γ can exist only if the density is zero. This implies the presence of a *vortex* with a quantized circulation[2] lh/m. Quantization of circulation was first proposed in the context of superfluid Helium by Onsager [59]. Feynman independently proposed quantization of circulation and investigated its consequences for flow experiments [60].

In order to conclude the story of the circulation, we should notice that, considering for example one quanta ($s = 1$), we have an expression for the circulation along the same path of the classical case γ

$$\frac{h}{m} = \oint_\gamma \boldsymbol{v} \cdot d\boldsymbol{r} = v 2\pi a \ . \tag{1.27}$$

The velocity can therefore be expressed as

$$v(r) = \frac{\hbar}{mr} \tag{1.28}$$

which has an inverse proportionality dependency on the radius r, opposite to the classical case, see Figure 1.3b.

[2]The magnitude of the quantum of circulation is approximately $4 * 10^{-7}(m_p/m)m^2/s$, where m_p is the proton mass.

1.5 Theoretical Framework: Quantum Field operators

1.5.1 Introduction to Quantum field operators

The wavefunction of N identical particles, denoted as $\psi(\mathbf{r}_1, \mathbf{r}_2, ..., \mathbf{r}_N)$, is defined such that its square modulus gives the probability of finding the N particles in the positions $\{\mathbf{r}_1, \mathbf{r}_2, ..., \mathbf{r}_N\}$. However, when N is large, treating this wavefunction within the standard quantum mechanics becomes arduous. It is more useful to make use of the compact and efficient formalism of the quantum field theory (QFT). In fact, QFT associates the system with a field operator $\hat{\psi}(\mathbf{r})$ that depends on a single set of three spatial coordinates instead of the standard $3N$:

$$\psi(\mathbf{r}_1, \mathbf{r}_2, ..., \mathbf{r}_N) \rightarrow \hat{\psi}(\mathbf{r}) \tag{1.29}$$

The field operator can be written as a sum of single-particle wave functions [61]:

$$\hat{\psi}(\mathbf{r}) = \sum_k \psi_k(\mathbf{r})\hat{a}_k \tag{1.30}$$

where $\hat{a}_k$ are the corresponding annihilation operators in the occupation number state, or Fock state. The bosonic creation $\hat{a}_k^\dagger$ and annihilation $\hat{a}_k$ operators satisfy the commutation relations:

$$\left[\hat{a}_k, \hat{a}_{k'}^\dagger\right] = \delta_{kk'} \quad \left[\hat{a}_k, \hat{a}_{k'}\right] = 0 \quad \left[\hat{a}_k^\dagger, \hat{a}_{k'}^\dagger\right] = 0 \tag{1.31}$$

Let us define the total number operator $\hat{N}$, which is expressed as a sum of the number operators for each mode, given by:

$$\hat{N} = \sum_k \hat{n}_k = \sum_k \hat{a}_k^\dagger \hat{a}_k \tag{1.32}$$

Using the commutation relations for the annihilation and creation operators, we can prove the standard relations that describe the behavior of the creation and annihilation operators in terms of the number operator. Specifically, we have:

$$\begin{aligned} \hat{a}_k \left|n_1 \dots n_k \dots\right\rangle &= \sqrt{n_k} \left|n_1 \dots n_k - 1 \dots\right\rangle \\ \hat{a}_k^\dagger \left|n_1 \dots n_k \dots\right\rangle &= \sqrt{n_k + 1} \left|n_1 \dots n_k + 1 \dots\right\rangle \end{aligned} \tag{1.33}$$

where n_k is the occupation number of the k-th state and the vector $|n_1 \dots n_k \dots\rangle$ represents a system with n_1 particles in the first state, n_k in the k-th and so on. The integers n_k form the spectrum of the number operator.

The commutation rules Eq. (1.31) for the field operators $\hat{\psi}$ and $\hat{\psi}^\dagger$ are directly inherited from the definition Eq. (1.30):

$$\left[\hat{\psi}(\mathbf{r}), \hat{\psi}^\dagger(\mathbf{r}')\right] = \delta(\mathbf{r} - \mathbf{r}') \quad \left[\hat{\psi}(\mathbf{r}), \hat{\psi}(\mathbf{r}')\right] = 0 \quad \left[\hat{\psi}^\dagger(\mathbf{r}), \hat{\psi}^\dagger(\mathbf{r}')\right] = 0 \tag{1.34}$$

where $\hat{\psi}^\dagger(\mathbf{r})$ is the conjugate transpose of the field operator. These boson field operators can be interpreted as creators and annihilators of particles at the position $\mathbf{r}$. In fact, in QFT, particles are "excitations" over the ground state, the vacuum. Again, let us introduce the total number operator:

$$\hat{N} = \int d\mathbf{r} \hat{\psi}^\dagger(\mathbf{r}) \hat{\psi}(\mathbf{r}). \tag{1.35}$$

Using the rules Eq. (1.34), similarly to before, we have:

$$\hat{\psi} \left|\psi_N\right\rangle = \sqrt{N} \left|\psi_N\right\rangle \quad \hat{\psi}^\dagger \left|\psi_N\right\rangle = \sqrt{N+1} \left|\psi_N\right\rangle \tag{1.36}$$

where $|\psi_N\rangle$ is an eigenvector of the number operator.

1.5.2 Many-body Hamiltonian and the Heisenberg equation

In many cases of interest, the hamiltonian contains one-body and two-body operators. An operator $\hat{U}$ is called a one-body operator if its action on a state $|\alpha_1 \dots \alpha_N\rangle$ of N particles is the sum of the action of $\hat{U}$ on each particle:

$$\hat{U} \left|\alpha_1 \dots \alpha_N\right\rangle = \sum_{i=1}^{N} \hat{U}_i \left|\alpha_1 \dots \alpha_N\right\rangle \tag{1.37}$$

that in a general basis can be rewritten as [62]:

$$\hat{U} = \sum_{\alpha\beta} \left\langle \alpha \right| \hat{U} \left| \beta \right\rangle \hat{a}_\alpha^\dagger \hat{a}_\beta. \tag{1.38}$$

For example, this is the case of the kinetic energy term and the external trapping potential. On the other hand, an operator $\hat{V}$ is called a two-body operator if its

action on a state $|\alpha_1 \dots \alpha_N\rangle$ of N particles is the sum of the action of $\hat{U}$ on all distinct pairs of particles:

$$\hat{V}\,|\alpha_1 \dots \alpha_N\rangle = \frac{1}{2} \sum_{1 \leqslant j \neq k \leqslant N}^{N} \hat{V}_i\,|\alpha_1 \dots \alpha_N\rangle \tag{1.39}$$

where the factor 1/2 is needed to avoid double counting. In a general basis it can be rewritten as [62]:

$$\hat{V} = \frac{1}{2} \sum_{\alpha\beta\gamma\delta} \langle\alpha\beta|\,\hat{V}\,|\gamma\delta\rangle\,\hat{a}^\dagger_\alpha \hat{a}^\dagger_\beta \hat{a}_\delta \hat{a}_\gamma. \tag{1.40}$$

This kind of term takes into account the interaction between particles. With these ingredients, we can write the general many-body hamiltonian:

$$\hat{H} = \sum_{\alpha\beta} \langle\alpha|\,\hat{U}\,|\beta\rangle\,\hat{a}^\dagger_\alpha \hat{a}_\beta + \frac{1}{2} \sum_{\alpha\beta\gamma\delta} \langle\alpha\beta|\,\hat{V}\,|\gamma\delta\rangle\,\hat{a}^\dagger_\alpha \hat{a}^\dagger_\beta \hat{a}_\delta \hat{a}_\gamma \tag{1.41}$$

and reformulate using boson field operators:

$$\hat{H} = \int d\mathbf{r} \hat{\psi}^\dagger(\mathbf{r}) U(\mathbf{r}) \hat{\psi}(\mathbf{r}) + \frac{1}{2} \int d\mathbf{r_1} \int d\mathbf{r_2} \hat{\psi}^\dagger(\mathbf{r_1}) \hat{\psi}^\dagger(\mathbf{r_2}) V(\mathbf{r_1}, \mathbf{r_2}) \hat{\psi}(\mathbf{r_2}) \hat{\psi}(\mathbf{r_1}). \tag{1.42}$$

To prove it, just replace the definition Eq. (1.30) into the new expression Eq. (1.42) of the hamiltonian and obtain the old one Eq. (1.41). This is called the hamiltonian in *second quantization*. In fact, in the first quantization the energy became an operator, while, this time, fields become operators and energy becomes a function again. The time evolution of the field operator $\hat{\psi}$ is governed by the Heisenberg equation:

$$i\hbar \frac{\partial}{\partial t} \hat{\psi}(\mathbf{r}, t) = \left[\hat{\psi}(\mathbf{r}, t), \hat{H}\right] \tag{1.43}$$

Using the Hamiltonian Eq. (1.42) and the commutaion rules Eq. (1.34), we obtain the time evolution of the field operator $\hat{\psi}$:

$$i\hbar \frac{\partial}{\partial t} \hat{\psi}(\mathbf{r}, t) = \left[U(\mathbf{r}) + \int d\mathbf{r}' \hat{\psi}^\dagger(\mathbf{r}') V(\mathbf{r}, \mathbf{r}') \hat{\psi}(\mathbf{r}')\right] \hat{\psi}(\mathbf{r}) \tag{1.44}$$

where we have used the symmetry of the two-body operator $\hat{V}$ under exchange of two indistinguishable particles, that is under exchange of **r** with **r'**. This is the Heisenberg equation describing a system of N interacting bosons.

1.6 Mean-field description: the Gross-Pitaevskii equation

At very low temperatures $T \ll T_C$, the full quantum description of the Heisenberg equation can be simplified by means of a semiclassical (mean-field) approach in terms of the quantum expectation of the field operator $\phi \equiv \langle\hat{\psi}\rangle$:

$$\hat{\psi} = \phi + \delta\hat{\psi} \tag{1.45}$$

where $\delta\hat{\psi}$ are the quantum fluctuations whose expectation value is vanishing by construction, $\langle\delta\hat{\psi}\rangle = 0$. At equilibrium, the expectation value $\phi = \langle\hat{\psi}\rangle$ is a complex number and its square modulus is the occupation number of the ground state that becomes nonzero for $T < T_C$. It therefore plays the role of the *order parameter* associated to the phase transition for Bose-Einstein condensation. From a dynamical point of view, this order parameter can be interpreted as the macroscopic wavefunction of the condensate, that describes the collective behavior of the bosonic sample. The fluctuation term $\delta\hat{\psi}$ is instead associated to the particles that are not condensed, the so-called *quantum depletion*. At very low temperatures, the latter gives a really not significant contribution, and can be therefore neglected. This correspond to the so-called *mean-field approximation*. Using this approximation, the Heisenberg equation Eq. (1.44) becomes:

$$i\hbar\frac{\partial}{\partial t}\phi(\mathbf{r},t) = \left[U(\mathbf{r}) + \int d\mathbf{r}' V(\mathbf{r},\mathbf{r}')|\phi(\mathbf{r}',t)|^2\right]\phi(\mathbf{r},t) \tag{1.46}$$

with the normalization condition to the total number of atoms N:

$$\int d\mathbf{r}\phi^*(\mathbf{r})\phi(\mathbf{r}) = N. \tag{1.47}$$

Consider a gas of N neutral atoms spatially trapped by an external potential. When the interaction is contact type, Eq. (1.46) becomes the famous time dependent Gross-Pitaevskii equation (GPE), from the name of Gross [63] and Pitaevskii [64] who first derived it:

$$i\hbar\frac{\partial}{\partial t}\phi(\mathbf{r},t) = \left[-\frac{\hbar^2}{2m}\nabla^2 + V_t(\mathbf{r}) + g|\phi(\mathbf{r},t)|^2\right]\phi(\mathbf{r},t) \tag{1.48}$$

The GPE is one of the most important theoretical tools to describe and study the mean-field behaviour of BECs. It has been applied with success to describe a large variety of experiments exploring dynamical and static properties of BEC in the dilute limit [5, 7, 9].

1.6.1 Mean-field energy spectrum

Back to the general many-body hamiltonian Eq. (1.41), instead of studying the dynamics, we can study the energy spectrum of the ground states. To do this, let us start by putting ourselves in the base of the impulses. The field operator changes with the rule Eq. (1.30):

$$\hat{\psi}(\mathbf{r}) = \frac{1}{\sqrt{V}} \sum_k e^{-i\mathbf{k}\cdot\mathbf{r}} \hat{a}_k \tag{1.49}$$

because the single particle wave-functions in the momentum space are plane waves. In this representation, the $\hat{a}_k$ operators assume the meaning of annihilation operators of a particle with momentum k. Considering a 3D homogeneous system, i.e. the system of N bosons described by the hamiltonian Eq. (1.42) but without the external trap, the Eq. (1.42) in momentum space becomes:

$$\begin{aligned}
\hat{H}_0 &\equiv \int d\mathbf{r} \hat{\psi}^\dagger(\mathbf{r}) T(\mathbf{r}) \hat{\psi}(\mathbf{r}) = \\
&= \frac{1}{V} \int d\mathbf{r} \sum_k e^{i\mathbf{k}\cdot\mathbf{r}} \hat{a}_k^\dagger \left[-\frac{\hbar^2}{2m} \nabla^2 \sum_{k'} e^{-i\mathbf{k}'\cdot\mathbf{r}} \hat{a}_{k'} \right] = \\
&= \sum_{k,k'} \underbrace{\frac{1}{V} \int d\mathbf{r} e^{i(\mathbf{k}-\mathbf{k}')\cdot\mathbf{r}}}_{\delta_{\mathbf{k},\mathbf{k}'}} \hat{a}_k^\dagger \hat{a}_{k'} \frac{\hbar^2 k'^2}{2m} = \\
&= \sum_k \frac{\hbar^2 k^2}{2m} \hat{a}_k^\dagger \hat{a}_k \equiv \sum_k E_k^0 \hat{a}_k^\dagger \hat{a}_k
\end{aligned} \tag{1.50}$$

$$\begin{aligned}
\hat{H}_1 &\equiv \frac{1}{2} \int d\mathbf{r} \int d\mathbf{r}' \hat{\psi}^\dagger(\mathbf{r}) \hat{\psi}^\dagger(\mathbf{r}') V(|\mathbf{r}-\mathbf{r}'|) \hat{\psi}(\mathbf{r}') \hat{\psi}(\mathbf{r}) = \\
&= \frac{1}{2V^2} \int d\mathbf{r} \int d\mathbf{r}' \sum_{i,j,t,s} e^{i\mathbf{k_i}\cdot\mathbf{r}} \hat{a}_{k_i}^\dagger e^{i\mathbf{k_j}\cdot\mathbf{r}'} \hat{a}_{k_j}^\dagger V(|\mathbf{r}-\mathbf{r}'|) e^{-i\mathbf{k_t}\cdot\mathbf{r}'} \hat{a}_{k_t} e^{-i\mathbf{k_s}\cdot\mathbf{r}} \hat{a}_{k_s} = \\
&= \frac{1}{2V^2} \sum_{i,j,t,s} \hat{a}_{k_i}^\dagger \hat{a}_{k_j}^\dagger \hat{a}_{k_t} \hat{a}_{k_s} \int d\mathbf{r} \int d\mathbf{r}' e^{i(\mathbf{k_i}-\mathbf{k_s})\cdot\mathbf{r}} e^{i(\mathbf{k_j}-\mathbf{k_t})\cdot\mathbf{r}'} V(|\mathbf{r}-\mathbf{r}'|) = \\
&= \frac{1}{2V} \sum_{i,j,t,s} \hat{a}_{k_i}^\dagger \hat{a}_{k_j}^\dagger \hat{a}_{k_t} \hat{a}_{k_s} \int d\mathbf{R} \underbrace{\frac{1}{V} \int d\mathbf{R}' e^{i(\mathbf{k_i}+\mathbf{k_j}-\mathbf{k_s}-\mathbf{k_t})\cdot\mathbf{R}'}}_{\delta_{\mathbf{k_i}+\mathbf{k_j},\mathbf{k_t}+\mathbf{k_s}}} e^{i(\mathbf{k_i}+\mathbf{k_t}-\mathbf{k_j}-\mathbf{k_s})\cdot\frac{\mathbf{R}}{2}} V(\mathbf{R}) = \\
&= \frac{1}{2V} \sum_{j,t,s} \hat{a}_{k_t+k_s-k_j}^\dagger \hat{a}_{k_j}^\dagger \hat{a}_{k_t} \hat{a}_{k_s} \int d\mathbf{R}\ e^{i(\mathbf{k_t}-\mathbf{k_j})\cdot\mathbf{R}}\ V(\mathbf{R}) = \\
&= \frac{1}{2V} \sum_{m,t,s} \hat{a}_{k_m+k_s}^\dagger \hat{a}_{k_t-k_m}^\dagger \tilde{V}(\mathbf{k_m}) \hat{a}_{k_t} \hat{a}_{k_s}
\end{aligned} \tag{1.51}$$

where we have used the integral definition of the Dirac delta function and in $\hat{H}_1$ we have made the two substitutions $\mathbf{R} = \mathbf{r} - \mathbf{r}'$, $\mathbf{R}' = \frac{\mathbf{r}+\mathbf{r}'}{2}$ and $\mathbf{k_m} = \mathbf{k_t} - \mathbf{k_j}$. Notice that the Dirac delta function represents the momenta's conservation and $\mathbf{k_m}$ has the meaning of the exchanged momentum between the two particles involved in the two-particles interaction $V(\mathbf{R})$. In addition, $\mathbf{k_m}$ can only assume values contained in the Fourier transform of the interaction $\tilde{V}(\mathbf{k})$.

Let us come back to a physical system and consider a dilute gas, so that there is only the two-body contact interaction Eq. (1.11). Decreasing the temperature T, BEC occurs increasing macroscopically the atoms number in ground state N_0. Calling N the total atoms number, the ground state can be approximated as ($N_0 \sim N$):

$$|\phi_0(N)\rangle \sim |N, 0, \dots 0\rangle \tag{1.52}$$

and therefore also creation and annihilation operators of the ground state do not change a lot the macroscopic number N:

$$\begin{aligned} \hat{a}_0 |\phi_0(N)\rangle &= \sqrt{N_0}\, |N-1, 0, \dots 0\rangle \sim \sqrt{N}\, |N, 0, \dots 0\rangle \\ \hat{a}_0^\dagger |\phi_0(N)\rangle &= \sqrt{N+1}\, |N+1, 0, \dots 0\rangle \sim \sqrt{N}\, |N, 0, \dots 0\rangle \end{aligned} \tag{1.53}$$

Hence the idea of the Bogoliubov perscription to replace operators with c-numbers:

$$\hat{a}_0 \sim \hat{a}_0^\dagger \sim \sqrt{N_0} \tag{1.54}$$

and also to consider excited states' operators as a perturbation with respect to the ground ones:

$$\hat{a}_k, \hat{a}_k^\dagger \ll \hat{a}_0, \hat{a}_0^\dagger \tag{1.55}$$

The hamiltonian in the momentum space Eq. (1.50) - Eq. (1.51) can be rewritten considering the fact that terms like $N_0^{3/2} \sim \hat{a}_0 \hat{a}_0 \hat{a}_0$ cannot exist due to the momentum conservation:

$$\hat{H} \equiv \sum_{k\neq 0} E_k^0 \hat{a}_k^\dagger \hat{a}_k + \frac{g}{2V}\left[N_0^2 + 2N_0 \sum_{k\neq 0}(\hat{a}_k^\dagger \hat{a}_k + \hat{a}_{-k}^\dagger \hat{a}_{-k}) + N_0 \sum_{k\neq 0}(\hat{a}_k^\dagger \hat{a}_{-k}^\dagger + \hat{a}_k \hat{a}_{-k})\right] \tag{1.56}$$

where we have used the pseudo potential expression Eq. (1.11) for the contact interaction, whose Fourier transform is g:

$$\tilde{V}(\mathbf{k}) = \int d\mathbf{r} V(\mathbf{r}) e^{-i\mathbf{k}\cdot\mathbf{r}} = \int d\mathbf{r}\; g\; \delta(\mathbf{r}) e^{-i\mathbf{k}\cdot\mathbf{r}} = g \tag{1.57}$$

Since the number of condensed atoms N_0 is not known, it is better to express it in terms of the total number of atoms:

$$N_0 = N - \sum_{k\neq 0} \hat{a}_k^\dagger \hat{a}_k = N - \frac{1}{2}\sum_{k\neq 0}(\hat{a}_k^\dagger \hat{a}_k + \hat{a}_{-k}^\dagger \hat{a}_{-k}) \tag{1.58}$$

so that Eq. (1.56) becomes:

$$\hat{H} \cong \frac{1}{2V}\left[gN^2 + \sum_{k\neq 0}(gN + E_k^0)(\hat{a}_k^\dagger \hat{a}_k + \hat{a}_{-k}^\dagger \hat{a}_{-k}) + gN\sum_{k\neq 0}(\hat{a}_k^\dagger \hat{a}_{-k}^\dagger + \hat{a}_k \hat{a}_{-k})\right] \tag{1.59}$$

This is a quadratic form that can be diagonalized by the linear Bogoliubov transformation [65]:

$$\begin{cases} \hat{a}_k = u_k \hat{\alpha}_k - v_k \hat{\alpha}_{-k}^\dagger \\ \hat{a}_{-k}^\dagger = u_k \hat{\alpha}_{-k}^\dagger - v_k \hat{\alpha}_k \end{cases} \tag{1.60}$$

whith $u_k, v_k \in \mathbb{R}$. This transformation introduces a new set of operators $\hat{\alpha}_k, \hat{\alpha}_k^\dagger$ to which we impose the same boson commutator of the original particle operators $\hat{a}_k, \hat{a}_k^\dagger$:

$$\left[\hat{\alpha}_k, \hat{\alpha}_k^\dagger\right] = u_k^2 - v_k^2 = 1 \tag{1.61}$$

that is satisfied, for instance, by imposing:

$$u_k = \cosh\theta_k \qquad v_k = \sinh\theta_k \tag{1.62}$$

The next step is substituting these new operators Eq. (1.60) with the condition Eq. (1.62) into Eq. (1.59) and cancelling the non-diagonal terms in the new operators. The latter requires the coefficients to take the form:

$$v_k^2 = \frac{1}{2}\left(\frac{E_k^0 + ng}{E_k} - 1\right) \tag{1.63}$$

where E_k^0 is the kinetic factor defined in Eq. (1.50), so that the new diagonalized hamiltonian is:

$$\hat{H} = E_0 + \sum_{k\neq 0} E_k \hat{\alpha}_k^\dagger \hat{\alpha}_k \tag{1.64}$$

where:

$$E_0 = \frac{1}{2}gnN + \frac{1}{2}\sum_{k\neq 0}\left[\frac{E_k}{V} - gn - \epsilon_k^0\right] \tag{1.65}$$

is the ground state energy at lowest approximation order $\frac{1}{2}gnN$, i.e. the only term left in the case $k = 0$, plus a first order correction due to terms with $k \neq 0$.

The other term of the hamiltonian is diagonal and contains the famous Bogoliubov dispersion law for the elementary excitations of the system:

$$E_k = \sqrt{E_k^{0\,2} + 2ngE_k^0} = \sqrt{\left(\frac{\hbar^2 k^2}{2m}\right)^2 + 2ng\frac{\hbar^2 k^2}{2m}} = \hbar k\sqrt{\frac{\hbar^2 k^2}{2m} + \frac{n}{m}g} \tag{1.66}$$

The ground state of the system Eq. (1.65) is no more the state Eq. (1.52) with all the atoms in the single-particle ground state with $k = 0$. The presence of the interaction, even if weak, makes the ground having some particles with nonzero momenta even at zero temperature. This phenomenon is called *quantum depletion* of the condensate. Specifically, the new ground state is the vacuum state of the quasi particles annihilated by α_k:

$$\hat{\alpha}_k \left|\phi_G\right\rangle = 0 \tag{1.67}$$

so that the number of particles N' with $k \neq 0$ is:

$$\begin{aligned} N' &= \langle\phi_G| \sum_{k\neq 0} \hat{a}_k^\dagger \hat{a}_k \left|\phi_G\right\rangle = \\ &= \langle\phi_G| \sum_{k\neq 0} (u_k\hat{\alpha}_k^\dagger - v_k\hat{\alpha}_{-k})(u_k\hat{\alpha}_k - v_k\hat{\alpha}_{-k}^\dagger) \left|\phi_G\right\rangle = \\ &= \sum_{k\neq 0} v_k^2 \equiv \sum_{k\neq 0} \langle n_k\rangle \end{aligned} \tag{1.68}$$

Substituting the sum with an integral and after some calculations, the density of these particles $n' \equiv \frac{N'}{V}$ with respect to the ones condensed n is (see Appendix A):

$$\frac{n'}{n} = \frac{8}{3\sqrt{\pi}}(na^3)^{1/2} \tag{1.69}$$

where a is the scattering length. Since we did all the math in the diluite gas limit in order to have only two-body interaction and also to have a quantum behaviour of the gas, this density is very low. To be precise, the diluite gas condition becomes:

$$na^3 \ll 1 \tag{1.70}$$

in order to have a small quantum depletion and therefore a big fraction of condensed atoms. For example, using typical values:

$$\frac{n'}{n} \propto (na^3)^{1/2} \cong (10^{14} cm^{-3}(100a_0)^3)^{1/2} \cong 10^{-2} \tag{1.71}$$

that, as we expected, is significantly less than 1.

1.6.2 Beyond Mean-field corrections

The energy of the ground state can be evaluated in a similar way to Eq. (1.68):

$$E_0 = \frac{1}{2}gnN - \sum_{k\neq 0} v_k^2 E_k \tag{1.72}$$

Notice that, in the limit of large momenta v_k^2 remain finite, while E_k increases as k^2:

$$\sum_{k\neq 0} v_k^2 E_k \sim \sum_k k^2 \tag{1.73}$$

so that the second term in Eq. (1.72) diverges. This divergence comes from the use of a delta potential. Such a shape allows the Fourier transform to assume all the possible momenta values, so atoms can exchange all the momenta. One method to eliminate the divergence is to use the delta potential with a truncation in momentum space $k \ll k_c$. The correct energy with this cut-off was derived in 1957 by Lee, Huang and Yang [66, 67]:

$$E_0 = \frac{1}{2}gnN\left[1 + \frac{128}{15\sqrt{\pi}}(na^3)^{1/2}\right] \tag{1.74}$$

This energy is composed of two terms, one due to the mean field and the other one due to quantum fluctuations. These have respectively the trends a and $a^{5/2}$ with the scattering length. By varying the latter using the Feshbach resonance, it is possible to search for the condition when the Lee-Huang-Yang (LHY) term is able to counterbalance the mean-field one. Remembering that we are in the diluite assumption that is essential in order to use the Bogoliubov prescription, quantum fluctuations are only a small correction to the mean-field energy. Despite this, its presence can be very important and even determine the difference between stability and instability of a BEC, as we will see in the formation of a dipolar supersolid. In order to arrive there, let us introduce the dipolar interaction.

1.7 Dipolar interaction

Until now, we have described a dilute gas as an ensemble of atoms interacting via elastic (point-like) collisions. However, there are also atoms with an intrinsic permanent dipole moment that makes them interact through dipole-dipole interaction

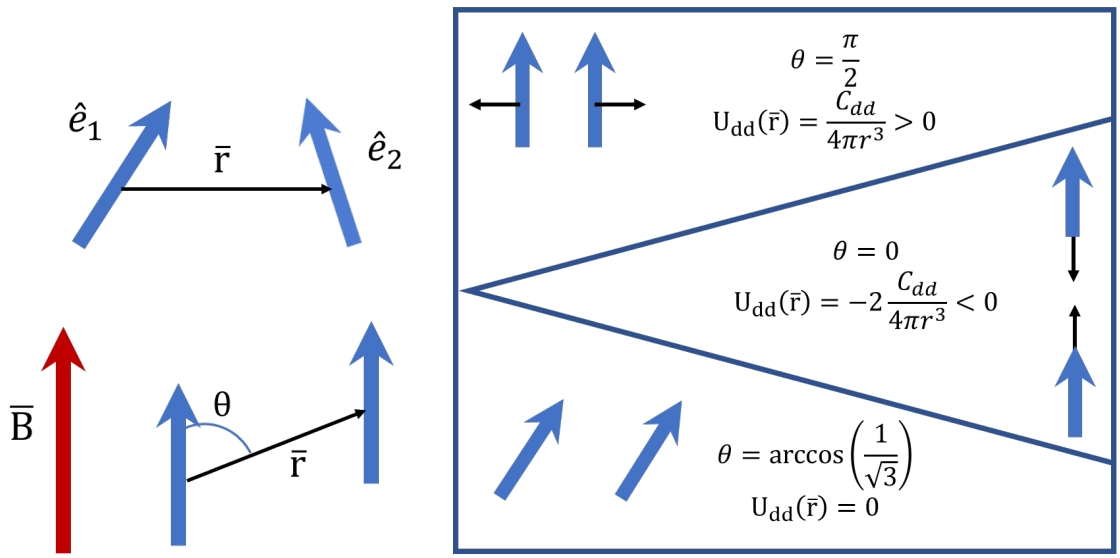

Figure 1.4: Properties of dipolar interaction. a) Two dipoles pointing in $\hat{e}_1$ and $\hat{e}_2$ directions, whose distance is defined by the vector $\bar{r}$. On the bottom they are aligned by an external magnetic field $\bar{B}$, whose angle with $\bar{r}$ is θ. b) Anisotropy of DDI. Depending on the angle θ, DDI can be repulsive, attractive and even be zero at the so-called magic angle.

(DDI). The general expression of DDI for two atoms with dipole moments oriented respectively along $\hat{e}_1$ and $\hat{e}_2$ is:

$$V_{dd}(\mathbf{r}) = \frac{C_{dd}}{4\pi}\frac{(\hat{e}_1 \cdot \hat{e}_2)r^2 - 3(\hat{e}_1 \cdot \mathbf{r})(\hat{e}_2 \cdot \mathbf{r})}{r^5} \tag{1.75}$$

where $\mathbf{r}$ is the vector connecting the two dipoles, while C_{dd} is a constant that depends on which kind of dipoles we are considering:

$$C_{dd}^{M} = \mu_0\mu^2 \quad \textit{magnetic dipoles} \tag{1.76a}$$

$$C_{dd}^{E} = \frac{d^2}{\epsilon_0} \quad \textit{electric dipoles} \tag{1.76b}$$

In the case of a quantum gas with an external field that aligns all dipoles in the same direction, Eq. (1.75) becomes:

$$V_{dd}(\mathbf{r}) = \frac{C_{dd}}{4\pi}\frac{1 - 3\cos^2\beta}{r^3} \tag{1.77}$$

where β is the angle between the dipoles direction and the $\mathbf{r}$ vector (see Figure 1.4a). The Eq. (1.77) is a long range interaction in the 3-dimensional case and is also

Atom	Momentum(M/E)	a_{dd}
Alkali	μ_B	$0.7a_0$
^{52}Cr	$6\mu_B$	$16a_0$
^{168}Er	$7\mu_B$	$65a_0$
^{162}Dy	$10\mu_B$	$130a_0$
KRb	$1D$	$2000a_0$
BaF	$6D$	10^4a_0

Table 1.1: Table of the highest dipole moments both magnetic (in Bohr magneton units) and electric (in $DeBaye \sim ea_0$).

anisotropic. In fact, as shown in Figure 1.4b, DDI can be repulsive when $\beta_m < \beta < \pi/2$, attractive when $0 < \beta < \beta_m$ and eventually cancel out at the so-called "magic angle" $\beta_m = \arccos(1/\sqrt{3})$.

In order to study properties of dipolar gases, we need DDI to be stronger than contact one. The parameter that quantify the order of magnitude of the dipolar energy is C_{dd}:

$$\left.\begin{aligned} C_{dd}^M &= \mu^2\mu_0 \simeq \mu_B^2\mu_0 = \frac{e^2\hbar^2}{4m^2}\mu_0 \\ C_{dd}^E &= \frac{d^2}{\epsilon_0} \simeq \frac{e^2a_0^2}{\epsilon_0} = \frac{e^2}{\epsilon_0}\frac{\hbar^4}{m^2e^4} \end{aligned}\right\} \quad \frac{C_{dd}^M}{C_{dd}^E} \simeq \frac{\mu_0\epsilon_0e^4}{4\hbar^2} \simeq \alpha^2 \sim 10^{-4} \tag{1.78}$$

where μ_0, μ and μ_B are the vacuum permeability, the magnetic moment of the particle and the Bohr magneton, while ϵ_0, d and a_0 are the vacuum permittivity, the electric dipole and the Bohr radius. In order to compare DDI with contact interaction, it is convenient to define a dipolar length (a_{dd}) analogous to the scattering one (a_S):

$$C_{dd} = 3\ g_{dd} = 3\ \frac{4\pi\hbar^2a_{dd}}{m} \tag{1.79}$$

Since a typical magnitude of contact scattering length is $a_s \sim 100a_0$, we can see from Table 1.1 that, in agreement with Eq. (1.78), all the electrical dipole cases are good to study DDI, while for magnetic dipoles the only good one is Dy. The main problem choosing electrical dipoles is that molecules cannot be experimentally cooled until the right degenerate regime. One possible solution could be using Rydberg atoms, but they have such a short lifetime that they cannot move inside the gas, and so they cannot collide. The most convenient solution in order to have important dipolar effects is thus to use Dy atoms.

1.7.1 Formation of Dipolar Droplets

The main condition for having the stabilization mechanism behind the formation of quantum droplets is the simultaneous presence of a slightly negative mean field and positive quantum fluctuations. This can happen only with more than one interaction in the system, because they need to quasi compensate at mean-field level. The first possibility is to have two different atomic species, giving rise to three different contact interactions (two intraspecies and one interspecies) [42, 68]. Another possibility is the use of a dipolar gas, that has both contact interaction (repulsive) and long range dipole-dipole interaction (partially attractive). In order to derive the LHY correction to the energy, we must start from the hamiltonian with one-body and two-body operators written in the momenta base Eq. (1.50)-Eq. (1.51). In order to derive the Bogoliubov spectrum in subsection 1.6.1 we considered the case of contact interaction, so that $\tilde{V}(\mathbf{k}) = g$. In the general case, we have:

$$E = \hbar k \sqrt{\frac{\hbar^2 k^2}{2m} + \frac{n}{m}\tilde{V}(\mathbf{k})} \tag{1.80}$$

so that in the dipolar case, it has the expression:

$$E = \hbar k \sqrt{\frac{\hbar^2 k^2}{2m} + \frac{n}{m}\left(g + \frac{C_{dd}}{3}(3\cos^2\alpha - 1)\right)} \tag{1.81}$$

where we have used the Fourier transform of the dipolar interaction (see Appendix F). The quantity C_{dd} is the dipolar constant defined in Eq. (1.79) that contains the dipolar scattering length a_{dd}, an analogous of the scattering length a_s which gives a measure of the intensity of the contact interaction. We can define the variable quantifying the ratio between the contact and dipolar interaction

$$\epsilon_{dd} = \frac{a_{dd}}{a_s} \tag{1.82}$$

With this definition, and the spectrum Eq. (1.81) we can search for the ϵ_{dd} values for which the dipolar BEC is unstable. In fact, the argument of the square root can be negative and makes the energy imaginary, giving rise to an instability. In the phonons limit ($k \to 0$), the kinetic contribution to the energy disappears and only the contact one remains. The BEC is always stable in the case of a modulation in the direction of the dipoles ($\alpha = 0$), because the argument of the square root is always positive. On the other side, considering a modulation in the perpendicular

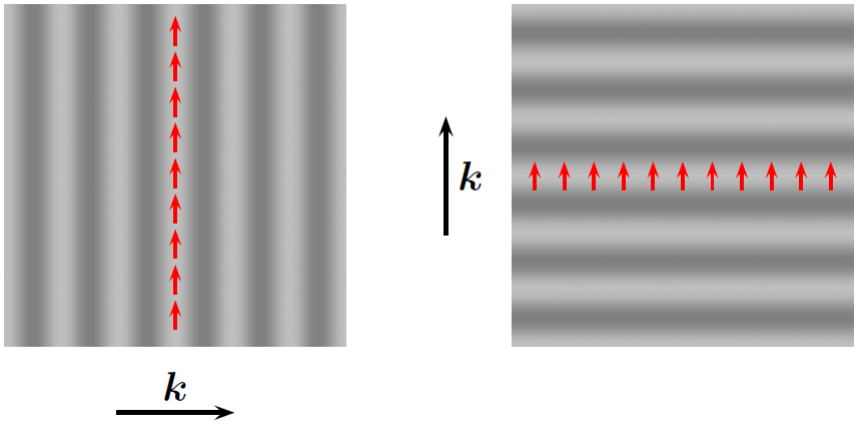

Figure 1.5: Left figure shows the case $\alpha = \pi/2$ where the perturbation is perpendicular to the dipoles alignment. In this case dipoles align themselves one above the other and the attraction is too high that they collapse. Right figure represents the $\alpha = 0$ case, so that dipoles are in the same direction of the perturbation. Therefore, they align side by side suppressing the high attractive interaction and making the system stable. Figure from [69].

direction ($\alpha = \pi/2$), there is the most unstable situation

$$\begin{aligned} \frac{n}{m}\left(g + \frac{C_{dd}}{3}(3\cos^2\alpha - 1)\right) = \frac{n}{m}\left(g - \frac{C_{dd}}{3}\right) < 0 \\ \frac{n}{m}\frac{4\pi\hbar^2}{m}(a_s - a_{dd}) < 0 \\ \epsilon_{dd} > 1 \end{aligned} \tag{1.83}$$

The physical interpretation of this condition is shown in Figure 1.5, from [69]. At first sight, this might seem counterintuitive: as dipoles side by side repel each other, one could conclude (wrongly) that the most unstable phonons correspond to those for which **k** is parallel to the dipoles. This behaviour can be intuitively understood looking at the Figure 1.5. A phonon with **k** perpendicular to the direction of dipoles $\alpha = \pi/2$ creates planes of higher density (light gray), in which the dipoles are in the plane, corresponding to an instability. For **k** parallel to the direction of dipoles ($\alpha = 0$) the dipoles point out of the planes of high density; such a perturbation is thus stable.

The above consideration shows that the behavior of a spatially homogeneous Bose gas with a strong dipole-dipole interaction is similar to that of a Bose gas

with an attractive short-range interaction characterized by a negative scattering length $a_s < 0$. In the latter case, however, the collapse of the gas can be prevented by confining the gas in a trap, provided the number of particles N in the gas is smaller than some critical value $N < N_c$ (see [42]). This is due to the finite energy difference between the ground and the first excited states in a confined gas. For a small number of particles, this creates an effective energy barrier preventing the collapse and, therefore, results in a metastable condensate. The same arguments are also applicable to a dipolar BEC in a trap with one very important difference: the sign and the value of the dipole-dipole interaction energy in a trapped dipolar BEC depend on the trapping geometry, and therefore, the stability diagram contains the trap anisotropy as a crucial parameter. As we will see in the next section, the geometry of the trap will be crucial for the roton instability, the main ingredient for supersolid.

Another interpretation of equation Eq. (1.83) is that the dipolar interaction, that is attractive, wins over the contact repulsive one ($a_{dd} > a_s$). The system should seem to collapse at mean-field level, but we have not considered the LHY term yet. The Bogoliubov approximation allows us also to find the ground state energy

$$E_0 = \frac{1}{2} n N \tilde{V}(\mathbf{k}=0) + \frac{1}{2} \sum_{k \neq 0} \left[E_k - n\tilde{V}(\mathbf{k}) - \frac{\hbar^2 k^2}{2m} \right] \tag{1.84}$$

that is the correction present in Eq. (1.65), but in the more general case, so that there is the Fourier transform of the potential $\tilde{V}(\mathbf{k})$ instead of g. In the case of dipole-dipole and contact interaction, Eq. (1.84) can be evaluated following Lima and Pelster [70, 71]. Sobstituting the sum with an integral, Eq. (1.84) diverges in the limit of big k. This divergence can be regularized by calculating the scattering amplitude at low momenta up to second order in the scattering potential $\tilde{V}(\mathbf{k})$ according to [61]

$$\frac{4\pi\hbar^2 a(\mathbf{k}=0)}{m} = \tilde{V}(\mathbf{k}=0) - \frac{m}{\hbar^2} \int \frac{d\mathbf{k}}{(2\pi)^3} \frac{\tilde{V}(-\mathbf{k})\tilde{V}(\mathbf{k})}{k^2} \tag{1.85}$$

where the scattering length a is related to the total effective interaction potential and therefore can be anisotropic such as the dipole-dipole interaction. In fact, the low-energy limit of the scattering amplitude for the dipole-dipole interaction, which can be obtained from multichannel scattering calculations, is not restricted to vanishing relative angular momentum (s-wave only), but contains all partial waves [72, 73]. This is consistent with an anisotropic scattering length, as defined

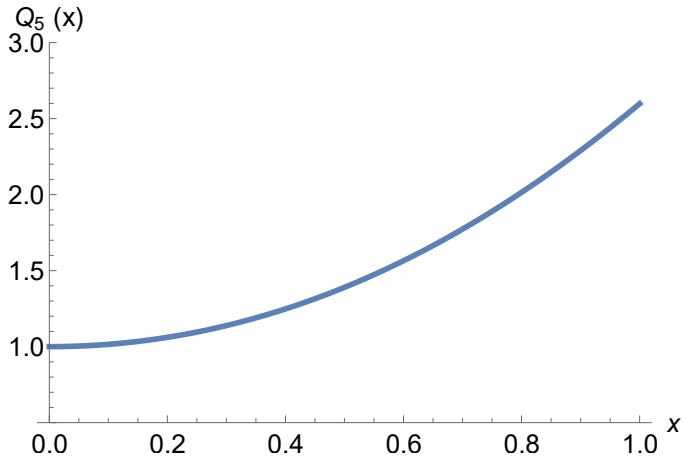

Figure 1.6: Function $Q_5(x)$ representing the DDI contribution to the LHY correction of the ground state energy. In the case $x = 0$, that is without dipolar interaction ($\epsilon_{dd} = 0$), it assumes the value 1, so that we recover the result Eq. (1.72). The more the dipolar interaction is strong, the more the $Q_5(x)$ function becomes important in the correction Eq. (1.87).

in Eq. (1.85). The ground state energy with the substitution Eq. (1.85) takes the form:

$$E_0 = \frac{1}{2}nNg\left[1+\epsilon_{dd}(3\cos^2\alpha-1)\right]+\frac{1}{2}\int\frac{d\mathbf{k}}{(2\pi)^3}\left[E(\mathbf{k})-n\tilde{V}(\mathbf{k})-\frac{\hbar^2k^2}{2m}+\frac{mn^2}{\hbar^2k^2}\tilde{V}(\mathbf{k})^2\right] \tag{1.86}$$

where we have used the invariance of $\tilde{V}(\mathbf{k})$ with respect to the replacement $\mathbf{k} \to -\mathbf{k}$. The last integral is the ground state correction due to quantum fluctuation that does not diverge anymore [71]

$$\Delta E = V\frac{1}{2}gn^2\frac{128}{15\sqrt{\pi}}(na_s^3)^{1/2}Q_5(\epsilon_{dd}) \tag{1.87}$$

This is similar to the expression Eq. (1.72) in the contact interaction case, except for the $Q_5(x)$ function that represents the DDI contribution. This auxiliary function, for $0 < x < 1$, is the special case $l = 3$ of:

$$Q_l(x) = (1-x)^{l/2}\,{}_2F_l\left(-\frac{l}{2},\frac{1}{2};\frac{3}{2};\frac{3x}{x-1}\right) \tag{1.88}$$

where ${}_2F_l(\alpha,\beta;\gamma;z)$ is the hypergeometric function [74]. Moreover, this function becomes imaginary when $\epsilon_{dd} > 1$, so it is consistent with the previous analysis of the stability of a dipolar BEC (see Eq. (1.83)). It also takes the value of one

when ϵ_{dd} is zero (see Figure 1.6), so it returns the LHY term in the case of only contact interaction Eq. (1.72). Finally, Eq. (1.87) is always positive and can counter a slightly negative mean-field, creating stable droplets.

The group of Pfau *et al.* has observed these dipolar quantum droplets using a dipolar Bose gas of ^{164}Dy in [75, 76]. This element has one of the strongest magnetic dipole moments in the periodic table with $\mu = 9.3\mu_B$ and a dipolar length $a_{dd} \sim 131a_0$, where μ_B is the Bohr magneton and a_0 is the Bohr radius. In [75], they prepared the BEC in two crossed laser beams along x and y, while dipoles were aligned along z thanks to an external magnetic field, so in the case $\alpha = \pi/2$. There was also a gradient in the magnetic field so as to counteract exactly the gravity that would drop the gas. When the lasers were turned off the gas remained in the form of a self-bound levitating cloud. In particular, the sample was prepared with an initial atom number higher than the critical one, so 3-body losses could decrease it until the right critical value. In conclusion, the cloud remained self-bound thanks to the interplay between the slightly stronger attractive long-range interaction and the repulsive contact one.

1.7.2 Roton instability in dipolar gases

In the previous section we have analyzed the instability of a dipolar gas in the limit of low momenta $\mathbf{k} \to 0$, but we do not know yet what happens for higher momenta. To do that, let us recall the case of liquid helium in which we have seen that the excitation spectrum presents a minimum between the linear trend for low k and the parabolic-like for high k (see Figure 1.2). This particular trend of the dispersion relation, that is the relation $\epsilon(k)$ between energy and momentum k, is the responsible one for the superfluid behaviour of liquid helium. The latter was firstly explained by Landau in 1941 introducing the concept of quasi-particles, elementary excitations of momentum k and energy given by the dispersion relation. The most famous are phonons, the ones corresponding to low k and linear trend, while rotons correspond to a minimum at higher k and have an energy gap.

In ^4He the roton formation mechanism is the competition between attractive van der Waals forces and repulsive Coulomb force. The momentum k_{rot} corresponding to the roton minimum, is then of the order of $d \sim < n >^{-1/3}$ and it scales as the inverse of the interatomic distance. This means that the presence of this minimum tends to create a local order in the system. As a consequence, we do not expect to find it in the field of ultracold atoms, in particular in a BEC. In fact, BECs forms

themselves in a very diluite regime with weak interparticle interactions, like the contact one, that has a range of action shorter than the mean interparticle distance and they have the usual Bogoliubov spectrum with only phonons. A way to achieve this particular trend of $\epsilon(k)$ in a BEC, consits in using dipolar atoms. Thanks to the anisotropy and long-range character of DDI, there is a competition between the partially attractive dipolar interaction and the repulsive contact interaction, giving rise to the desired roton minimum, even in a weak interacting regime [77].

There are also other systems where is expected the formation of a roton minimum, but it is imposed by external manipulations. Such systems are for example BECs with spin-orbit coupling, BECs in shaken optical lattices and BECs irradiated by off resonant laser light [78]. In the latter case, the position k_{rot} of the minimum is directly proportional to the inverse of the laser wavelength. On the contrary, dipolar BECs have rotons thanks only to internal interactions, so it is a self-induced behaviour. The peculiarity of this dipolar roton minimum consists in depending on the geometry of the trap, as emphasized both theoretically [77] and experimentally [79].

The roton instability has been discovered in 2003 by Santos *et al.* [77] in an infinite pancake trap with dipoles oriented along the z-direction perpendicular to the trap plane. They solved the Bogoliubov-De Gennes equations considering the so-called Thomas-Fermi profile along z, i.e. a parabolic shape. In the pancake trap, that is a cylindrical trap more confined along the axis of symmetry than radially (Figure 1.7d), the roton-maxon spectrum allows a visual physical interpretation. For in-plane momenta q much smaller than the inverse size l_z of the condensate in the confined direction, excitations have two-dimensional (2D) character. Hence, as the dipoles are perpendicular to the plane of the trap, they mainly repel each other and the in-plane excitations are phonons. For $q \gg 1/l_z$, particles do not "see" the end of the trap and excitations acquire 3D character, so that the interparticle repulsion is reduced. The result is a decrease in the excitation energy under an increase of q. The energy reaches a minimum and then starts to grow as the excitations continuously enter the single-particle regime. There is a critical density above which the minimum reaches the zero energy value and the excitations around the minimum become unstable, i.e. the condensate collapses [77].

Similarly, the group of Ferlaino *et al.* [79] studied the presence of the roton minimum in the case of a cigar-like geometry with trap elongation along only one

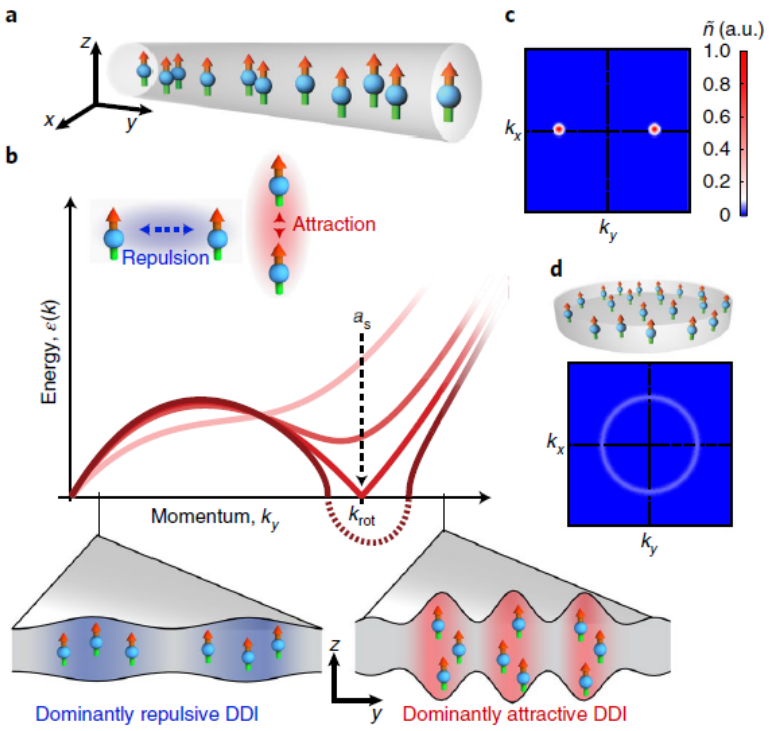

Figure 1.7: a) A cigar shaped trap with dipoles oriented in one of the two perpendicular directions and c) the corresponding roton population in momentum space, that consists in two points. b) The rotonization of the energy spectrum. d) A pancake shaped trap with dipoles oriented in the perpendicular direction and the corresponding roton population in momentum space, that is a ring. Figure taken from [79].

direction (y) perpendicular to the magnetization axis z (Figure 1.7a). The argument that visualize the formation of the roton minimum is very similar to the pancake trap. The main ingredients are the anisotropic character of the DDI (Figure 1.7b) together with the tighter confinement along z (Figure 1.7b). Consider the elementary excitations of momentum k_y that correspond in real space to a density modulation along y of wavelength $2\pi/k_y$. For low momenta, the atoms stay mainly side by side repelling each other and creating the phononic branch of the spectrum. On the other side, when $k_y > 1/l_z$ the atoms can align one above the other in a head-to-tail configuration, so that DDI becomes negative. For even higher momenta the single-particle regime wins thanks to kinetic energy. In conclusion, a strong DDI creates a minimum at $k_y = k_{rot}$ set by the geometrical scaling $k_{rot} \sim 1/l_z$. This scaling has been experimentally observed [79].

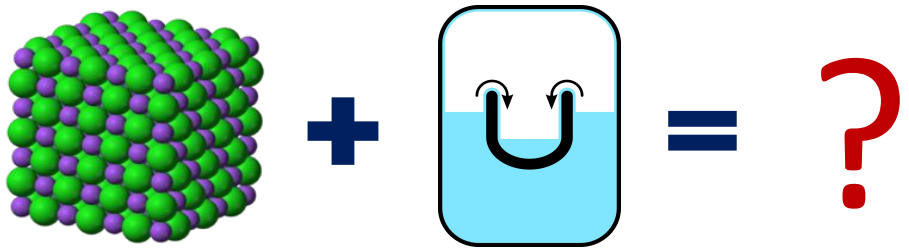

Figure 1.8: Can a solid be superfluid? [15]

In the work [79], they study also this rotonization of the spectrum from a theoretical point of view. In particular, they make an analytical model solving the Bogoliubov-De Gennes equations using an approximated density. This is homogeneous along the direction of weaker confinement but has a parabolic shape in the other two perpendicular directions. In this way, the spectrum acquires the gapped form similar to the helium case (see Figure 1.2):

$$\epsilon(k_y)^2 \simeq \Delta^2 + \frac{2\hbar^2 k_{rot}^2}{m}\frac{\hbar^2}{2m}(k_y - k_{rot})^2 \tag{1.89}$$

where Δ is the height of the gap, while k_{rot} is the position of the roton minimum, as said before. The specific expressions of the parameters can be found in [79].
In the next section we are going to see how this rotonic minimum is the key for the formation of the dipolar supersolid.

1.8 The long quest for supersolid

1.8.1 Superfluid solid ^{4}He

The most intuitive picture of a solid is a system that resists blows and twists while maintaining its shape, unlike fluids. On the other hand, a superfluid is roughly a fluid where you can have a mass flow without friction. Consequently, the idea of having a solid with the characteristics of a superfluid is striking and counterintuitive. Despit this, and even if Penrose and Onsager demonstrated that an ideal crystal cannot support BEC [80], a teorethical prediction of such a state of matter was done in the 1960s by A. F. Andreev and L. M. Lifshitz [14]. Their idea was the following: considering a quantum crystal in free space, even in the zero-temperature limit, most of the atoms would be localized at the nodes of a periodic lattice but some of the nodes would be vacant. These vacancies could tunnel very

quickly from site to site and be delocalized, which would lower the vacancy energy so much that even the ground state of the crystal would contain a nonzero density of these so-called *zero-point vacancies*. As a consequence, the crystal would be incommensurate, meaning that the atoms number would be different from the sites number of the crystal lattice. The most promising candidate was solid ^{4}He, having the largest amplitude of zero-point motion of atoms in the ground state and also having bosonic vacancies. Such motion was presumed to create a stable (repulsive) gas of zero-point vacancies undergoing Bose-Einstein condensation at low temperature. Thus, the perfect crystal would simultaneously be a solid and a superfluid, which in literature is called "supersolid"[3], as firstly suggested by Matsuda and Tsuneto [81] and Mullin [82]. A lot of effort was made in that direction by Thouless [83], Chester [84] and by Leggett [15], who even entitled his article with the provocative and also evocative question: "Can a solid be superfluid?". In this pioneering work, he suggested that such a supersolid in a rotating bucket would show a reduced rotational moment of inertia due to the finite fraction of superfluid atoms that would not participate to the classical rotation.

All these works led to a deeper understanding of supersolids. However, all these authors concentrated on crystals where the occupation number of a lattice site never exceeds 1. In these systems the estimation for the ratio between the superfluid density and the normal density was rather pessimistic ($\sim 10^{-4}$ [15]).

From an experimental point of view, the story began in 2004, when Kim and Chan at the Pennsylvania State University reported measurements of reduced rotational moment of inertia of a rotating bucket of solid-^{4}He as supporting evidences for supersolidity [85, 86]. The team followed the idea of Legget to use a torsional oscillator, a hollow disk that hangs down on a rod and oscillates by rotating clockwise and then counterclockwise at a frequency around 1 kHz, which depended on the oscillating mass. Below a temperature of order 100 mK they observed that the resonance frequency increased as if some of the mass inside the box had decoupled from the moving walls, and from this they proposed that solid helium was perhaps a supersolid. Then in 2007, Day and Beamish at the University of Alberta in Canada

[3]The name "supersolid", however, looks a bit confusing. The standard meaning of the word "super" accentuates the given property, but does not contradict it. For instance, "superradiance" means superstrong radiance. "Superconductivity" implies superstrong conductivity. "Superfluidity" signifies superstrong fluidity. Then "supersolidity" should assume superrigid solidity. However, vice versa, one talks about a solid with some superfluid properties.

published a paper that posed a tough challenge to Kim and Chan and others in the field [87]. Suppose that the solid helium was not perfectly stiff but had some "give" (elasticity) that led to a resistance to twisting. If the solid helium were to stiffen up when cooled, the oscillation period would decrease, regardless of the amount of moving mass. Many other theoretical and experimental results finally convinced Kim and Chan to redo the experiments. They redesigned the torsional oscillator, taking every precaution to eliminate space for elastic helium. This time, the changes in oscillation previously attributed to a supersolid state were completely absent [88]. It therefore seemed that helium could only exist as a superfluid or crystalline solid, but not simultaneously.

1.8.2 Search for supersolidity in BEC

Meanwhile, theorists turned their efforts in the search for supersolidity in a new system: a BEC of an atomic gas. The approach was absolutely different from all the previous attempts: the goal was no longer to create a superfluid in a solid, but to generate a density modulation (like the one in a crystal) in a superfluid. At a glance, a density modulation should not be possible in a BEC because its atoms are so dilute and have only short-range (contact) interactions. But a couple of papers from 2003 proposed a way to engineer the necessary atom interaction in the form of a long-range dipolar coupling [77, 78]. This interaction would induce a roton-maxon minimum in the energy, similar to that of helium. In particular, O'Dell *et al.* [78] found this minimum in elongated cigar-shaped condensates with laser-induced dipole-dipole interatomic interactions, while Santos *et al.* [77] studied a BEC of atoms with permanent dipole moments in an infinite pancake trap.

From an experimental point of view, in 2010 in the group of Esslinger at ETH Zurich, a lattice-supersolid was realized by shining a laser onto a BEC placed inside the optical mode of a cavity [89]. The superfluid atomic gas could scatter light from that laser into the resonator and self-organize in the resulting optical lattice potential that modulates the superfluid density. Nonetheless the cavity boundary conditions force the solid position to take only a discrete set of values, i.e. it cannot form continuously in space. In 2017, other groups achieved the necessary atom interactions by coupling the BECs to light fields, either exploiting spin-orbit coupling [90] or cavity-mediated long-range interactions [91] between the atoms.

All these experiments, however, depends on external perturbations, rather than intrinsic properties of the system. It was not until 2019 that there was the first

observation of an intrinsically supersolid system.

1.8.3 Observation of a dipolar Supersolid

The first experimental observation of a dipolar supersolid was made in 2019 by the group of Modugno *et al.* [16] in Pisa and confirmed shortly after [17, 18]. In the experiment in Pisa, the authors start from a BEC of $N = 3500$ atoms of ^{162}Dy. This is an isotope of Dysprosium with an high dipolar scattering length $a_{dd} = 130a_0$, where a_0 is the Bohr radius. The harmonic trap where the BEC is formed, is made by two crossed laser beams and has frequencies $\omega = 2\pi$ $(18.5, 53, 81)$ Hz. An external magnetic field polarizes all the atoms along the z direction. The stronger confinement along the z direction (the same of the polarization) is chosen in order to induce the roton instability discussed above. This is, however, counterbalanced by the quantum fluctuations. The weaker confinement is along x, which is therefore the direction where the array of droplets is formed. This geometry of the trap creates a one dimensional modulation of the density, so a supersolid along x.

In particular, the initial BEC is formed with a contact scattering length $a_s = 157a_0$. The tuning of it is made by slowly varying the intensity of the magnetic field, thanks to the presence of a magnetic Feshbach resonance. Then, the detected observable is the momentum distribution $n(k_x, k_y)$, which they obtain after a free expansion 62ms long. In Figure 1.9, on the top, are represented the momentum distributions for three different final scattering length. The top row is in the case $a_s = 108a_0$, which corresponds to $\epsilon_{dd} \simeq 1.2$ and the result is a pure dipolar BEC. The middle row represents the case with $a_s = 94a_0$, so $\epsilon_{dd} \simeq 1.38$. It presents side peaks, which correspond to a density modulation in real space and is the signature of a supersolid phase. From these images, the position of the peaks is $\sim 1.2\mu m^{-1}$, which is similar to the roton momentum $k_{rot} = 1.53\mu m^{-1}$ for an unconfined system in the xy plane. To be noticed that the peaks remain for several tens of milliseconds before going back to a BEC regime. This is caused by the three-body losses. Finally, the bottom row is the incoherent droplets regime with $a_s = 88a_0$, thus $\epsilon_{dd} \simeq 1.47$. This incoherence is confirmed by the irregular formation of the stripes and by the great difference between the various repetitions of the free expansion.

The phase coherence of the stripe regime has been studied in the same work [16] both theoretically and experimentally. In the experiment, the authors extract the phase from the fitting procedure of $n(k_x, k_y)$ and find that the interference phase variance remains constant over an interval of $\Delta t \sim 20ms$. The theoretical

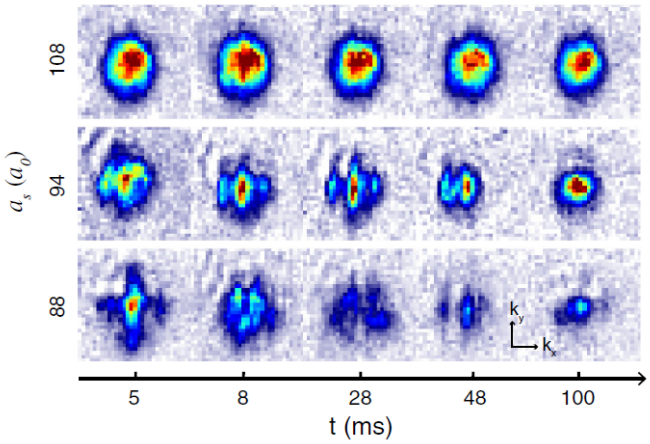

Figure 1.9: Experimental images from [16], which show the momentum distribution of the system after a free expansion. Going from left to right, there are many snapshots at increasing times. In the top row the system is in the BEC regime with $a_s = 108a_0$ ($\epsilon_{dd} \simeq 1.2$), the middle row presents the stripe modulation which highlights the supersolid regime at $a_s = 94a_0$ ($\epsilon_{dd} \simeq 1.38$) and in the bottom row there is the independent droplets regime with $a_s = 88a_0$ ($\epsilon_{dd} \simeq 1.47$).

study has been done by the group at the University of Hannover, which performed a dynamical simulation of the system using a GPE extended with a LHY correction to the mean-field energy and considering also three-body losses and finite temperature effects. Some snapshots are presented in Figure 1.10. The top row shows the case $a_s = 94a_0$ where there is a superficial modulation on a BEC background which keeps the phase coherence during the dynamic. On the contrary, in the bottom row is shown the incoherent case at $a_s = 88a_0$, which loses the phase coherence during the dynamic, as expected.

This result has been studied and confirmed also by two other groups in Stuttgart [17] and Innsbruck [18]. The first group used the same trap and atoms of [16], but they made also an *in-situ* imaging, even if the resolution was not enough to clearly distinguish the peaks of the modulation. The second one, instead, used another kind of atoms, the ^{166}Er and a more elongated harmonic trap with $\omega = 2\pi(300, 16, 222)$Hz.

Supersolidity exists in dipolar BECs.

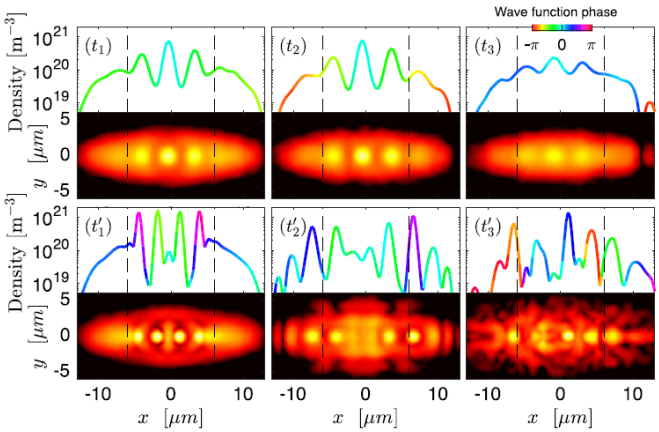

Figure 1.10: Numerical simulations from [16]: snapshots at different times of the system dynamic. Both density cuts $n(x,0,0)$ and integrated densities $\int dz\, n(x,y,z)$ are shown. The colors represents the phase of the wave function. On the top row, there is the case of the supersolid regime at $a_s = 94a_0$ and we can see the phase coherence during the dynamic. On the bottom row, there is the case $a_s = 88a_0$, which is the incoherent regime as we can see from the many different phases in the wave function.

1.8.4 Characterization of a dipolar supersolid

Many experiments have attempted to obtain further information on the characterization of the supersolid through the study of the excitation spectrum. Supersolidity has both the phase coherence at the origin of the superfluid phenomena and the lattice modulation of a solid. The first one breaks the phase invariance while the second one breaks the translational one [12]. These two spontaneous breaking symmetries are associated to two gapless excitations. The group in Innsbruck has showed that in a trapped dipolar supersolid two distinct excitation branches appear, respectively associated with crystal and superfluid excitations [92]. The group in Stuttgart has observed directly the low-energy Goldstone mode associated with the spontaneous symmetry breaking of the phase invariance [93], revealing the phase rigidity of the system. The group in Pisa has shown both theoretically and experimentally [94] that in the supersolid regime the axial breathing mode, i.e. the lowest compressional mode, bifurcates. The higher frequency mode is associated to the lattice deformation, which increase due to the dipolar repulsion between clouds [94]. On the contrary, the lower frequency mode is related to the superfluid component which is reduced increasing ϵ_{dd} until it vanishes in the indipendent droplets

regime [94]. A measure of the superfluid fraction in a dipolar supersolid has been performed through the reduced moment of inertia [95], like the original experiment of Kim and Chan [85, 86]. The experiment revealed a large superfluid fraction [95], but were not precise enough to assess its sub-unity value [96, 97].

In Chapter 3 we are going to study the phase rigidity of a dipolar supersolid through the presence of a self-induced Josephson effect in it. Furthermore, in Chapter 4, we are going to use the Josephson effect in order to propose a completely new method to measure the superfluid fraction. In this way, we are able to fully demonstrate the sub-unity superfluid fraction of the dipolar supersolid [19].

2

What's the phenomenon: Josephson effect

2.1 Introduction to Josephson Effect

The Josephson effect is a fundamental phenomenon in quantum physics discovered by Brian D. Josephson in 1962 [20]. It describes the macroscopic quantum coherence in a weak link connecting two superconductors, that is now called a Josephson junction (JJ) [21, 22]. At its core, the Josephson effect reveals an astonishing characteristic: the presence of a supercurrent in a JJ even in the absence of an applied voltage. This behavior challenges classical intuition by demonstrating that, at the quantum level, electrical currents can flow without the need for an electric field. This effect underscores the ability of many-particle quantum systems to exhibit macroscopic quantum coherence.

The central mathematical framework for understanding the Josephson effect, which will be discussed in further detail in the following section, provides a quantitative description of the relationship between the supercurrent and the phase difference across the junction. This mathematical description forms the basis for our understanding of the Josephson effect and its manifestations in various quantum systems.

The Josephson effect holds great significance and has far-reaching implications

beyond the realm of superconductors. Its relevance extends to diverse quantum systems such as superfluids [98] and BECs [27, 28]. The effect's pivotal role in linking macroscopic quantum coherence with observable phenomena has led to numerous practical applications in quantum technologies [22], including the development of ultra-sensitive detectors for electromagnetic radiation [32] and the creation of highly precise voltage standards [1] [33], which are of utmost importance in metrology and quantum computing [99, 100].

2.2 Josephson effect in superconductors

Superconductors are materials that exhibit zero electrical resistance and the expulsion of magnetic fields when cooled below a critical temperature. Being a quantum condensate, a superconductor is globally described by a single wave function $\psi(\mathbf{r}) = \sqrt{n(\mathbf{r})}\exp(i\theta(\mathbf{r}))$, where $n(\mathbf{r})$ is the probability amplitude to find an electron pair (Cooper pair) in the position $\mathbf{r}$ and $\theta(\mathbf{r})$ is the global phase of the superconductor. A JJ is a system consisting of two superconducting metals separated by a barrier, usually a layer of insulating material. If the barrier is small enough, the wave function can penetrate it, allowing Cooper pairs to tunnell the barrier to the other superconductor. This tunnelling creates a constant Josephson density current across the junction even in the absence of an external electric or magnetic field (DC Josephson effect). The presence of an applied voltage across the JJ induces an oscillating current (AC Josephson effect) and moreover an rf oscillating voltage induces a dc current through the JJ. A superconducting loop with two JJs in either arm is very sensitive ($10^{-14}T$) to the magnetic flux enclosed (SQUID, superconducting quantum interference device).

2.2.1 Josephson Equations

Let us consider two superconductors at the two sides of the insulating barrier (figura). They are described by the two wavefunctions:

$$\psi_R(\mathbf{r}) = \sqrt{n_R(\mathbf{r})}\exp(i\theta_R(\mathbf{r})) \qquad \psi_L(\mathbf{r}) = \sqrt{n_L(\mathbf{r})}\exp(i\theta_L(\mathbf{r})) \tag{2.1}$$

[1] The NIST (National Institute of Standards and Technology) standard for one volt is achieved by using an array of 32.768 Josephson junctions in series [33].

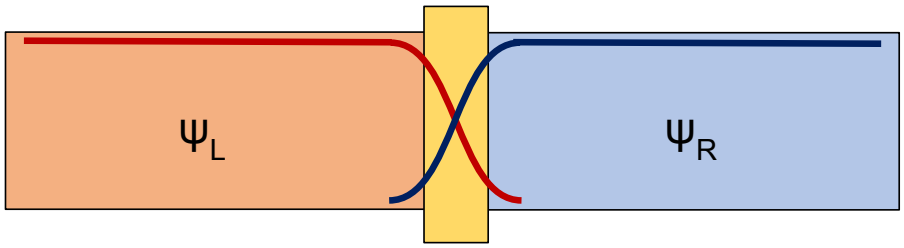

Figure 2.1: Schematic rapresentation of a JJ. Two superconductors described by two wavefunctions on the left (L) and right (R) of a weak link that suppresses their amplitudes, but leaving a small tail allowing tunnelling between them.

where we have used the subscripts L and R for the right and left side of the junction respectively (see Figure 2.1). The time evolution of an isolated superconductor is described by the Schrödinger equation

$$i\hbar\frac{\partial\psi(\mathbf{r},t)}{\partial t} = E\psi(\mathbf{r},t) \tag{2.2}$$

where E is the ground state energy and we have set the reduced Planck constant $\hbar = 1$. If the coupling between the two sides of the JJ is weak (weak link regime), the equations for the two wavefunctions remain almost unaltered with the addition of one coupling (or tunnelling) coefficient K [23, 101]

$$\begin{aligned} i\hbar\frac{\partial\psi_R(\mathbf{r},t)}{\partial t} &= E_R\psi_R(\mathbf{r},t) + K\psi_L(\mathbf{r},t) \\ i\hbar\frac{\partial\psi_L(\mathbf{r},t)}{\partial t} &= E_L\psi_L(\mathbf{r},t) + K\psi_R(\mathbf{r},t) \end{aligned} \tag{2.3}$$

where we put the subscripts R and L also to the energies E. Writing the wavefunction explicitly with amplitude and phase, we obtain two equations

$$\begin{aligned} i\hbar\left(\frac{\dot{n_R}}{2} + in_R\dot{\theta_R}\right) &= E_Rn_R + K\sqrt{n_Ln_R}e^{i(\Delta\theta)} \\ i\hbar\left(\frac{\dot{n_L}}{2} + in_L\dot{\theta_L}\right) &= E_Ln_L + K\sqrt{n_Ln_R}e^{-i(\Delta\theta)} \end{aligned} \tag{2.4}$$

where we have used the dot to indicate the derivative with respect to time and we have defined $\Delta\theta \equiv \theta_L - \theta_R$. Equating real and imaginary parts of the Eqs.Eq. (2.4),

we obtain four equations describing the time evolution of the two probability amplitudes n_L and n_R and the two phases of the two superconductors θ_L and θ_R:

$$\begin{aligned}
\hbar \dot{n_R} &= 2K\sqrt{n_L n_R}\sin(\Delta\theta) \\
\hbar \dot{n_L} &= -2K\sqrt{n_L n_R}\sin(\Delta\theta) \\
\hbar \dot{\theta_R} &= -E_R - K\sqrt{\frac{n_L}{n_R}}\cos(\Delta\theta) \\
\hbar \dot{\theta_L} &= -E_L - K\sqrt{\frac{n_R}{n_L}}\cos(\Delta\theta)
\end{aligned} \tag{2.5}$$

One of the initial observations that can be made is the equality between $\dot{n_R}$ and $-\dot{n_L}$. Let us consider two identical superconductors with equal densities $n_L = n_R \equiv n_0$, then we have $\dot{n_L} = \dot{n_R} = 0$, and it seems like there is no current flow in the JJ. However, this reasoning does not take into account the phase of the system and is based solely on a classical dynamics perspective. Following all four Eq. (2.5), we can observe the presence of a Josephson density current given by $\dot{n_R}$ (or -$\dot{n_L}$)

$$J = J_0 \ \sin(\Delta\theta) \tag{2.6}$$

where $J_0 \equiv 2Kn_0/\hbar$ is the maximum current achievable in the JJ. This current-phase relation is the typical mark of the Josephson effect. In the absence of a voltage across the JJ, the ground state energies are equal ($E_L = E_R$) and $\hbar\dot{\Delta\theta} = E_R - E_L = 0$. The mere presence of a constant phase difference between the two superconductors induces a sinusoidal Josephson current inside the junction. This is the *DC Josephosn effect*.

Let us now apply a constant voltage V across the junction. The energy difference that a Cooper pair feels is $E_R - E_L = qV$, where $q = -2e$ and e is the electric charge. In the hypothesis $n_L \cong n_R$, there is still a Josephson current of the form of Eq. (2.6), but with a phase difference varying in time

$$\dot{\Delta\theta} = \frac{2eV}{\hbar} \tag{2.7}$$

that is the second Josephson equation [20] where $\Delta\theta_0$ is the phase difference at time $t = 0$. Substituting this expression inside the current Eq. (2.6), we obtain

$$J = J_0 \sin\left(\Delta\theta_0 - \frac{2eV}{\hbar}t\right) = J_0 \sin(\Delta\theta_0 + \omega_J t) \tag{2.8}$$

The presence of the constant voltage V across the junction implies a Josephson current oscillating at the Josephson frequency $\omega_J = 2eV/\hbar$. This is the *AC Josephson*

effect.
The application of a voltage with a constant term plus a high frequency one

$$V = V_0 + v\cos(\omega t) \tag{2.9}$$

gives rise to a Josephson current of the form

$$J = J_0 \sin\left(\Delta\theta_0 - \frac{2e}{\hbar}V_0 t + \frac{2e}{\hbar}\frac{v}{\omega}\sin(\omega t)\right) \tag{2.10}$$

For small amplitudes of the oscillating term $v \ll V_0$, the current is

$$J = J_0\left[\sin\left(\Delta\theta_0 - \frac{2e}{\hbar}V_0 t\right) + \frac{2e}{\hbar}\frac{v}{\omega}\sin(\omega t)\cos\left(\Delta\theta_0 - \frac{2e}{\hbar}V_0 t\right)\right] \tag{2.11}$$

Averaging over times much larger than the inverse of the frequencies ω_J and ω, the first term vanishes, but the second term is nonzero for the frequencies

$$\omega = s\frac{2e}{\hbar}V_0 \tag{2.12}$$

where s is an integer number. This effect is a kind of "phase-locking" of the Josephson current to an external signal and gives rise to the so-called *Shapiro steps* [102], a characteristic structure in the current-voltage relation when

$$V_0 = \frac{\hbar\omega}{2ne} \tag{2.13}$$

Effect	Second Josephson equation $\dot{\Delta\theta}$	Josephson current J
DC Josephson effect	0	$J_0\sin(\Delta\theta_0)$
AC Josephson effect	$\frac{2eV}{\hbar}$	$J_0\sin(\Delta\theta_0 - \frac{2eV}{\hbar}t)$
SQUID	$\frac{2e}{\hbar}(V_0 + v\cos(\omega t))$	$J_0\sin\left(\Delta\theta_0 - \frac{2eV}{\hbar}t\right) + J_0\frac{2e}{\hbar}v\sin(\omega t)\cos\left(\Delta\theta_0 - \frac{2eV}{\hbar}t\right)$

2.2.2 Josephson applications: SQUIDs

Another interesting phenomena happens when two JJs are put in parallel along a superconducting ring and driven by an external common current J_{tot}. This is the scheme of a Superconducting QUantum Interference Device, the so-called SQUID,

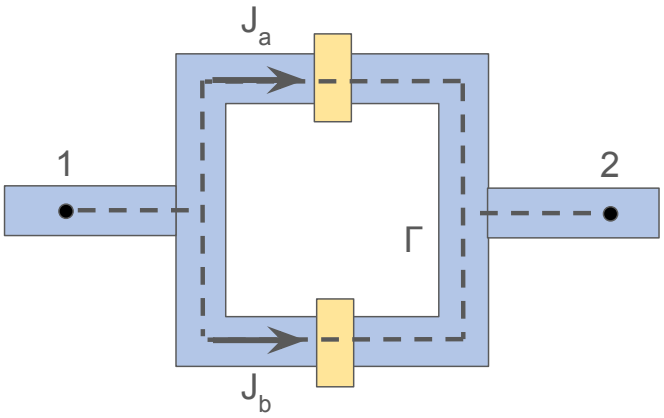

Figure 2.2: Representation of a Superconducting QUantum Interference Device (SQUID)

see Figure 2.2. Its mechanism is based both on Josephson effect and flux quantization. As we have seen for superfluid systems in section 1.4, also superconductors are described by a macroscopic single-valuedness wavefunction, which is at the basis of flux quantization. In this case, the supercurrent density is given by

$$\boldsymbol{J} = \frac{\hbar}{m}\left(\boldsymbol{\nabla}\theta - \frac{2e}{\hbar}\boldsymbol{A}\right)n \tag{2.14}$$

where $\mathbf{A}$ is the vector potential. Inside the ring, the supercurrent is zero and we have

$$\hbar\boldsymbol{\nabla}\theta = 2e\boldsymbol{A} \tag{2.15}$$

Integrating both sides of Eq. (2.15) along a closed path Γ around the ring, we have

$$\theta_f - \theta_i = \oint_\Gamma \boldsymbol{\nabla}\theta \cdot \boldsymbol{dl} = \frac{2e}{\hbar}\oint_\Gamma \boldsymbol{A}\cdot\boldsymbol{dl} = \frac{2e}{\hbar}\phi \tag{2.16}$$

where ϕ is the magnetic flux enclosed by the path Γ and $\phi_{i,f}$ are the initial and final phases. The single-valuedness of the wavefunction imposes that $\theta_f - \theta_i$ equals an integer number of 2π. As a consequence, the flux adjusts itself in order to be

$$\phi = \frac{\hbar}{2e}(\theta_f - \theta_i) = s\frac{\pi\hbar}{e} \quad s \in \mathbb{N} \tag{2.17}$$

that is the *flux quantization* of a superconductor.
Let us now consider two JJs in parallel in the ring. The phase difference $\theta_2 - \theta_1$ can be calculated along the upper part and the lower part of the ring

$$\begin{aligned}(\theta_2 - \theta_1)_a &= \Delta\theta_a + \frac{2e}{\hbar}\int_{upper}\boldsymbol{A}\cdot\boldsymbol{dl}\\ (\theta_2 - \theta_1)_b &= \Delta\theta_b + \frac{2e}{\hbar}\int_{lower}\boldsymbol{A}\cdot\boldsymbol{dl}\end{aligned} \tag{2.18}$$

where $\Delta\theta_{a,b}$ are the phase differences across the two JJs. The phase differences along the two paths must be equal, so that the phase differences across the JJs differs exactly by the phase given by the vector potential $\Delta\theta_a - \Delta\theta_b = \frac{2e}{\hbar}\int_\Gamma \boldsymbol{A}\cdot\boldsymbol{dl}$. We can write the single $\Delta\theta_{a,b}$ as

$$\Delta\theta_a = \Delta\theta_0 + \frac{e}{\hbar}\phi \qquad \Delta\theta_b = \Delta\theta_0 - \frac{e}{\hbar}\phi \tag{2.19}$$

These two phases give rise to two Josephson currents whose sum is the total current in the ring

$$\begin{aligned} J_{total} &= J_a + J_b = J_0\left[\sin\left(\Delta\theta_0 + \frac{e}{\hbar}\phi\right) + \sin\left(\Delta\theta_0 - \frac{e}{\hbar}\phi\right)\right] \\ &= 2J_0\sin\left(\Delta\theta_0\right)\cos\left(\frac{e}{\hbar}\phi\right) \end{aligned} \tag{2.20}$$

We can observe that, whatever the value of $\Delta\theta_0$, the maximum value of the current J_{max} is given by

$$J_{max} = 2J_0\left|\cos\frac{e\phi}{\hbar}\right| \tag{2.21}$$

at the points given by

$$\phi = s\frac{\pi\hbar}{e} \tag{2.22}$$

where s is an integer. These flux values are the same found in Eq. (2.17) for the flux quantization.

2.3 Josephson effect in Superfluid Helium

As discussed in Chapter 1, the helium, specifically ^{4}He, displays quantum mechanical behavior at low temperatures. In particular, it undergoes a phase transition with the superfluid state in which it displays peculiar characteristic such as flowing without friction and phase coherence. A superfluid system can be described at a quantum level by a single collective wavefunction, as for superconductors. Therefore, if we consider two reservoirs of superfluids divided by a weak link, they are again described by two wavefunctions as in Eq. (2.1) and the mathematical construction is the one derived in the previous section for superconductors, following the famous lectures of Feynman [23]. Specifically, we derive the same Josephson equations

$$\begin{aligned} \dot{n_R} &= -\dot{n_L} = 2K\sqrt{n_L n_R}\sin(\Delta\theta) \\ \dot{\theta_{R,L}} &= -E_{R,L} - K\sqrt{\frac{n_{L,R}}{n_{R,L}}}\cos(\Delta\theta) \end{aligned} \tag{2.23}$$

where we put $\hbar = 1$. The main difference consists in the source of energy difference that induces the dynamics of the phase difference. Considering as before $n_L \cong n_R$, we obtain $\dot{\Delta\theta} = E_L - E_R$ that is not given by the voltage across the JJ, but by the chemical potential difference $\Delta\mu$ between the two superfluid reservoirs. The Josephson current in a superflulid JJ is then

$$J = J_0 \sin(\Delta\theta) \tag{2.24}$$

$$\dot{\Delta\theta} = -\Delta\mu \tag{2.25}$$

The current-phase relation Eq. (2.24) displays the sinusoidal relation between the Josephson current and the phase difference. The phase evolution equation Eq. (2.25) has been demonstrated by Anderson to be a more general behavior of superfluids [24, 25] and explains the system behaviour with applying a chemical potential difference to it [26]. The absence of $\Delta\mu$ implies a constant Josephson current, like a DC Josephson effect, while its presence induces the sinusoidal Josephson current

$$J = J_0 \sin(\Delta\mu t) \tag{2.26}$$

A chemical potential difference could be produced by a pressure difference ΔP between the two reservoirs of the JJ

$$\Delta\mu = \frac{\Delta P m}{n} \tag{2.27}$$

This gives rise to the counterintuitive effect that, pushing the superfluid through the weak link by applying a pressure difference, this does not results in a linear current as one could imagine in a classical way, but results instead in a sinusoidal oscillation of the fluid at the Josephson frequency $\omega_J = \Delta\mu$. Typical values of this frequency are in the sound regime, opposite from the superconductors Josephson effect where the frequency is in the microwave regime.
First experiments on superfluid weak link phenomena were performed with ^{3}He because of nanofrabication issues [22]. The weak link, indeed, needs to be smaller than the healing length of the superfluid that is higher, for example, for ^{4}He.

2.4 Bosonic Josephson Junction

BECs are ultracold quantum gases of bosonic particles that display phase coherence and are described by a single wavefunction [6]. Thanks to this characteristic and

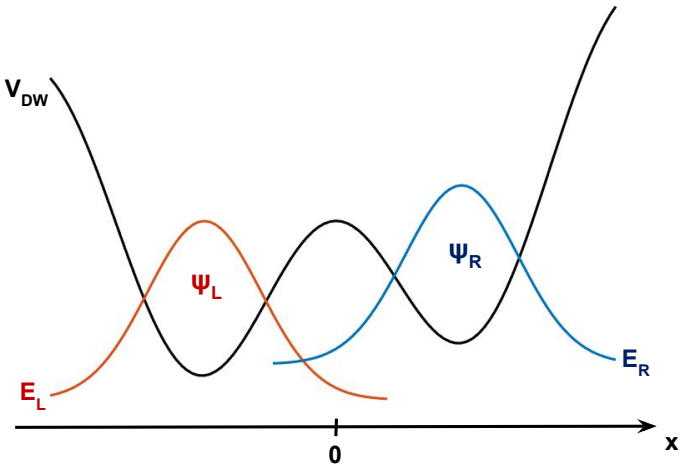

Figure 2.3: Schmatic representation of a BJJ. A BEC in a double well potential V_{DW} is divided in two spatially localized wavefunctions $\psi_{L,R}$ in the two wells. Here is represented the nonsymmetric case where there is an energy difference between the two wells given by the offset $E_{L,R}$.

to the high precision reachable with the confining potential [8], they became a new well controllable environment to study Josephson effect [22, 29].

A bosonic Josephson junction (BJJ) can be implemented using spatial or internal degrees of freedom of bosons [22]. In the first case, the weak link can be created by a doble well potential which spatially separates the single-component BEC into the two wells and allows tunnelling of bosons between them [29]. In the case of internal degrees of freedom, the BEC is spatially in the same position, but it is composed by two hyperfine states and the tunnelling is realized through a weak driving field [103]. We are going to focus on the external BJJ and derive Josephson equations in this system.

Following the derivation of Josephson equations for a superconducting JJ that we have done in subsection 2.2.1, we have to write the dynamical evolution of the wavefunctions $\psi_{L,R}$ describing the BECs localized in the right (R) and left (L) well of the double well potential (see Figure 2.3). This system can be described by a two-state model [27]

$$\begin{aligned} i\frac{\partial \psi_L}{\partial t} &= (E_L + N_L U_L)\psi_L - K\psi_R \\ i\frac{\partial \psi_R}{\partial t} &= (E_R + N_R U_R)\psi_R - K\psi_L \end{aligned} \tag{2.28}$$

where $U_{L,R}$ are the on-site interaction parameters, $N_{L,R} = |\psi_{L,R}|^2$ are the populations of the two BECs and K is the coupling matrix element[2] [23, 27]. These parameters can be expressed in terms of overlap of the local wavefunctions with a two-mode ansatz.

The system is described by the condensate wave function $\psi(\mathbf{r}, t)$ which is solution of the GPE (see Eq. (1.48))

$$i\frac{\partial\psi(\mathbf{r},t)}{\partial t} = \left(-\frac{\nabla^2}{2m} + V_{DW} + g|\psi(\mathbf{r},t)|^2\right)\psi(\mathbf{r},t) \tag{2.29}$$

where V_{DW} is the double-well potential and g is the contact interaction parameter. We write ψ as a linear combination of the wave functions localized in the two wells

$$\psi(\mathbf{r},t) = \psi_L(t)\phi_L(\mathbf{r}) + \psi_R(t)\phi_R(\mathbf{r}) \tag{2.30}$$

where we have separated the spatial and temporal evolution. This ansatz needs some hypothesis. The GPE has a nonlinear term, thus it is not obvious that the condensate wavefunction can be written as a linear superposition of the two states. The suppression of the wavefunction amplitude in the weak link needs to be high enough to almost cancel the interaction in the link and preserve this ansatz. Moreover, we neglect the dynamics of the spatial parts which are localized in the wells and the small change in density due to the Josephson current. This can be estimated to give a negligible correction to the chemical potential difference between the wells [104, 105].
The temporal parts of the wavefunctions can be written, as for superconductors, with phase and amplitude

$$\psi_{L,R}(t) = \sqrt{N_{L,R}(t)}\ \exp(i\theta_{L,R}(t)) \tag{2.31}$$

where $N_{L,R}$ are the populations in the two wells with the constriction that the total atom number $N = N_1 + N_2$ is conserved. The system Eq. (2.28) assumes the form

$$\begin{aligned} i\left(\frac{\dot{N}_L}{2} + iN_L\dot{\theta_L}\right) &= (E_L + N_L U_L)N_L - K\sqrt{N_L N_R}e^{i(\theta_R-\theta_L)} \\ i\left(\frac{\dot{N}_R}{2} + iN_R\dot{\theta_R}\right) &= (E_R + N_R U_R)N_R - K\sqrt{N_L N_R}e^{-i(\theta_R-\theta_L)} \end{aligned} \tag{2.32}$$

[2] We have used the sign minus in order to have a positive coupling K.

so that the imaginary parts give the populations evolution

$$\begin{aligned}
\dot{N_L} &= -K\sqrt{N_L N_R}\sin(\theta_R - \theta_L) \\
\dot{N_R} &= K\sqrt{N_L N_R}\sin(\theta_R - \theta_L) \\
\dot{\theta_L} &= E_L + N_L U_L - K\sqrt{\frac{N_R}{N_L}}\cos(\theta_R - \theta_L) \\
\dot{\theta_R} &= E_R + N_R U_R - K\sqrt{\frac{N_L}{N_R}}\cos(\theta_R - \theta_L)
\end{aligned} \tag{2.33}$$

Defining the population and phase imbalances

$$Z \equiv \frac{N_L - N_R}{N} \qquad \Delta\theta \equiv \theta_R - \theta_L \quad , \tag{2.34}$$

we obtain the standard Josephson equations for a BJJ [27]

$$\begin{aligned}
\dot{Z} &= -\sqrt{1 - Z^2}\sin\Delta\theta \\
\dot{\Delta\theta} &= \Delta E + \Lambda Z + \frac{Z}{\sqrt{1 - Z^2}}\cos\Delta\theta
\end{aligned} \tag{2.35}$$

where we have rescaled the time by $2K$ and we have defined the dimensionless parameters

$$\begin{aligned}
\Delta E &\equiv \frac{E_L - E_R}{2K} + \frac{N(U_L - U_R)}{4K} \\
\Lambda &\equiv \frac{N(U_L + U_R)}{4K}
\end{aligned} \tag{2.36}$$

The first one is the energy difference given both by the trap energies $E_{L,R}$ and the on-site interaction parameters $N_{L,R}U_{L,R}$, while the second one is the total interaction energy given by the sum of the contributions from the two wells.
We can distinguish many regimes resembling the ones found for the superconducting JJ. First of all, in the limit of vanishing interaction $\Lambda \to 0$ and symmetric trap $\Delta E = 0$, Eq. (2.35) becomes

$$\ddot{Z} = -Z \tag{2.37}$$

thus implying Rabi-like oscillations in the population of each trap with a frequency

$$\omega = 2K \tag{2.38}$$

This is the analogue of the DC Josephson effect where, in absence of an external applied voltage (here an energy difference between the wells) there is a current in the JJ (here a flow in the BJJ).

Keeping the interactions in the symmetric trap ($U_L = U_R \equiv U$) and linearizing Eq. (2.35) for small values of Z and $\Delta\theta$, we have

$$\begin{aligned} \dot{Z} &\cong -\Delta\theta \\ \dot{\Delta\theta} &\cong (1+\Lambda)\, Z \end{aligned} \tag{2.39}$$

where $\Lambda = NU/(2K)$. The result is a sinusoidal current $I \equiv \dot{Z}N/2$ with frequency

$$\omega_J = \sqrt{1+\Lambda} \tag{2.40}$$

whos dimensional expression is

$$\omega_J = \sqrt{4K^2 + 2NUK} \tag{2.41}$$

A different approximation can be done linearizing only in Z

$$\begin{aligned} \dot{Z} &= -\sin\Delta\theta \\ \dot{\Delta\theta} &= \Delta E + (\Lambda + \cos\Delta\theta) Z \end{aligned} \tag{2.42}$$

In the limit of a big energy difference $\Delta E \gg (\Lambda + \cos\Delta\theta)$, that is the opposite of what we have done so far, we obtain a linear increase in time of the phase difference and an oscillating Josephson current

$$\begin{aligned} \Delta\theta(t) &= \Delta\theta(0) + \Delta E\, t \\ \dot{Z} &= -\sin\left(\Delta\theta(0) + \Delta E\, t\right) \end{aligned} \tag{2.43}$$

This is the analogue of the AC Josephson effect.
A further observation can be made considering an oscillation in the laser that creates the barrier of the double well, thus

$$\Delta E(t) = \Delta E(1 + \delta \sin(\omega_0\, t)) \tag{2.44}$$

where δ and ω_0 are the amplitude and frequency of this oscillation. This results in a Josephson current

$$< I(t) >= \delta < \sin(\omega_0\, t) \sin(\Delta E\, t) > \tag{2.45}$$

where the mean is performed over time and gives non-zero values. This current has a resonance at $\omega_0 = \Delta E$, which is the analogue of the Shapiro steps for a superconducting JJ.

2.4.1 Macroscopic Quantum Self-Trapping

An intriguing phenomenon observed in BJJs is the so-called Macroscopic Quantum Self-Trapping (MQST), whose presence is solely due to the non-linear interaction. In an analogy with the classical pendulum [27], with Z as the angular momentum and $\Delta\theta$ as the angle of inclination, the oscillating regime we found in the previous section is the counterpart of small-amplitude oscillations. A high value of Z causes the pendulum not to oscillate around the equilibrium position, but to rotate completely. In a BJJ, this regime corresponds to a self-locking of the population in one well. Let us find the critical value Z_c of initial population imbalance that demarks the transition from the oscillating regime to the MQST.
Considering Z and $\Delta\theta$ as canonically conjugate variables, it applies

$$\dot{Z} = -\frac{\partial H}{\partial \Delta\theta} \qquad \dot{\Delta\theta} = \frac{\partial H}{\partial Z} \tag{2.46}$$

where the Hamiltonian H is

$$H = \Delta E\, Z + \frac{\Lambda}{2} Z^2 - \sqrt{1 - Z^2}\, \cos\Delta\theta \tag{2.47}$$

or, in the symmetric case

$$H = \frac{\Lambda}{2} Z^2 - \sqrt{1 - Z^2}\, \cos\Delta\theta \tag{2.48}$$

In Figure 2.4 is plotted the Hamiltonian Eq. (2.48) with $L = 10$ as an example. For small values of Z and $\Delta\theta$ the energy levels assume low values and follow paths closed symmetrically around zero. Increasing the energy (from blue to yellow area) leads to open trajectories periodic in the angle $\Delta\theta$. The separatrix line is given by

$$H_c \equiv \max_{\Delta\theta} H(Z = 0, \Delta\theta) = \max_{\Delta\theta}(-\cos\Delta\theta) = 1 \tag{2.49}$$

Considering an initial condition with a non-zero population imbalance but no phase difference, the critical value of Z can be found imposing an initial energy higher than H_c

$$H(Z, \Delta\theta = 0) = \frac{\Lambda}{2} Z^2 - \sqrt{1 - Z^2} > H_c = 1 \tag{2.50}$$

so that

$$Z > Z_c \equiv \frac{2}{\Lambda}\sqrt{\Lambda - 1} \tag{2.51}$$

The self-trapping of the population in one of the two wells occurs due to the nonlinear interatomic interaction and demonstrates the coherence of a macroscopic

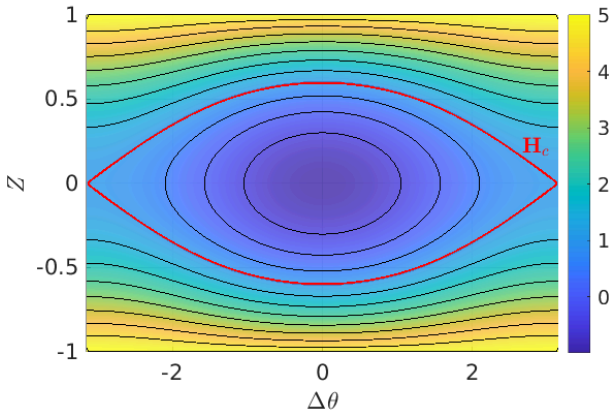

Figure 2.4: Phase space of the hamiltonian Eq. (2.48) with $\Lambda = 10$. For small values of Z and $\Delta\theta$ black countour lines of H are closed symmetrically around zero, while increasing the energy with different initial conditions, leads to open trajectories periodic in the angle $\Delta\theta$. Values of H increase from the blue area to the yellow one. The red line is the separatrix characterised by the value $H_c = 1$.

number of atoms. The MQST is impossible to observe in superconducting JJs, due to the external circuit which suppresses charge imbalances.

In the next chapter we are going to demonstrate that this effect can take place also in supersolid dipolar quantum gases, where the JJ is uniquely self-induced.

3

Josephson effect in a supersolid dipolar quantum gas

3.1 Self-Induced Josephson junction

In Chapter 1 we have learnt that the dipolar supersolid is a superfluid state of matter with an intrinsic density modulation, like the crystal structure of a solid, but with more than one atom per site [16–18, 106]. Each site, in fact, consists of hundreds of atoms that we are going to call clusters. Atoms can flow between clusters while keeping the periodic structure intact [19]. In Chapter 2 we have learnt that a Josephson junction (JJ) is made of two superconductors [20], superfluids [24, 25] or BECs connected through a weak link [27–29, 104]. The key ingredient for a JJ is the suppression of the order parameter, usually induced by the presence of an externally imposed barrier that creates a weak link allowing tunnelling between the two reservoirs.

The main idea of this chapter and the works on which it is based consists in considering the minima in the self-induced density modulation of the dipolar supersolid as the weak link of the JJ [19]. So far the Josephson effect in supersolids has not been studied beyond the phenomenological modelling of the relaxation towards the ground state in a cold-atom system [107]. There is no theoretical or experimental evidence for local Josephson oscillations. The problem is complicated by the fact

that, in supersolids, the weak links are self-induced by internal interactions rather than by an external potential, so they can change during the dynamics. Therefore it is not clear if phenomena such as Josephson oscillations can exist at all in a supersolid. The complete absence of an external potential in addition to the harmonic trap differs it from previous works [108] and makes it a completely self-induced Josephson junction (SIJJ).

We will begin by developing a theoretical model that will allow us to write the analogue of the Josephson equations for our dipolar supersolid. We will then be able to identify a sinusoidal Josephson current regime, which we will call small oscillations, and another self-trapping regime, identical to that observed in BJJs. We will also find the same results by directly integrating the eGPE on a numerical level and comparing the value of the parameters in a specific case. This model and the numerical simulations were also compared in another regime directly with the experimental data [19] of the group with which we (Luca Pezzè, Augusto Smerzi and Beatrice Donelli) have a direct collaboration with and from which this work originated (Giulio Biagioni, Nicolò Antolini, Marco Fattori, Andrea Fioretti, Carlo Gabbanini, Massimo Inguscio, Luca Tanzi and Giovanni Modugno). In particular, this collaboration generated the work of Chapter 4 [19] and whose discussions built the basis for the birth of this chapter.

3.2 Theoretical model

3.2.1 Introduction to the theoretical model

The theoretical model follows Feynman's derivation of the Josephson equations [23] and the standard derivation of the two-mode model for a bosonic JJ [27]. Feynman derived his model for two superconductors described by two isolated wavefunctions $\psi_{1,2}$ with ground state energies $E_{1,2}$ and a coupling K between them. When the coupling is zero, their dynamics are described by the two Schrödinger equations $i\partial\psi_1/\partial t = E_1\psi_1$ and $i\partial\psi_2/\partial t = E_2\psi_2$. Adding the coupling between them, would lead to the two coupled equations [23]

$$\begin{aligned} i\frac{\partial\psi_1}{\partial t} &= E_1\psi_1 + K\psi_2 \\ i\frac{\partial\psi_2}{\partial t} &= E_2\psi_2 + K\psi_1 \end{aligned} \tag{3.1}$$

where we put the reduced Planck constant $\hbar = 1$. From these equations it is possible to derive the Josephson equations for the population and phase imbalance between the two superconductors (see subsection 2.2.1).

Considering a BJJ with two wavefunctions $\psi_{1,2}$ describing the two BECs, we need to include also the nonlinear contact interaction. The system, indeed, is no more described by a Schrödinger equation, but by a GPE. The nonlinear term gives a contribution to the energy of the system which is quadratic in the populations ($\propto N_{1,2}^2 \equiv |\psi_{1,2}|^4$) [27]

$$\begin{aligned} i\frac{\partial\psi_1}{\partial t} &= (E_1 + N_1U_1)\psi_1 + K\psi_2 \\ i\frac{\partial\psi_2}{\partial t} &= (E_2 + N_2U_2)\psi_2 + K\psi_1 \end{aligned} \tag{3.2}$$

where $U_{1,2}$ are the on-site interaction parameters and $N_{1,2}$ are the populations of the two BECs. From Eq. (3.2) we can derive Josephson equations for fractional population imbalance z and phase imbalance $\Delta\theta$, as we have seen in Chapter 2.

As we have seen in Chapter 1, the dipolar supersolid is decribed by a eGPE with the dipolar interaction, which is still a mean-field contribution and the first order quantum fluctuation correction, the LHY. Doing a two-mode ansatz, as for the BJJ, in this system is not trivial that is going to lead to two coupled equations of the form of Eq. (3.2). For example, the dipolar interaction is likely going to be included in the U parameter because it depends on the same power of the wavefunction square modulus, while the LHY depends of an higher power. We are going to demonstrate that also in the dipolar supersolid we can apply a two-mode model and derive the Josephson equations, as in the BJJ.

3.2.2 Two-mode model for a dipolar supersolid Josephson junction

The supersolid system is described by the extended Gros-Pitaevskii equation (eGPE)

$$\begin{aligned} i\frac{\partial\psi(\mathbf{r},t)}{\partial t} = \Bigg[&-\frac{\nabla^2}{2m} + V_t(\mathbf{r}) + g|\psi(\mathbf{r},t)|^2 \\ &+ \int d\mathbf{r}' V_{dd}(\mathbf{r}-\mathbf{r}')|\psi(\mathbf{r}',t)|^2 + \gamma(\epsilon_{dd})|\psi(\mathbf{r},t)|^3 \Bigg] \psi(\mathbf{r},t). \end{aligned} \tag{3.3}$$

This equation has been extensively used in theoretical studies of a dipolar-gas supersolid [70, 71, 106, 109**?** , 110], finding excellent agreement with experimental results [16–19, 95, 111]. In Eq. (3.3), $V_t(\mathbf{r}) = \frac{1}{2}m(\omega_x^2x^2 + \omega_y^2y^2 + \omega_z^2z^2)$ is

an harmonic trapping potential, $g = \frac{4\pi\hbar^2 a_s}{m}$ is the contact interaction parameter and $V_{dd}(\mathbf{r}) = \frac{C_{dd}}{4\pi}\frac{1-3\cos^2\theta}{r^3}$ is the dipolar interaction. In addition to the standard Gross-Pitaevskii equation, Eq. (3.3) includes the LHY term calculated within the local density approximation for a dipolar system [70, 71] and has the form $\gamma(\epsilon_{dd}) = \frac{32}{3\sqrt{\pi}} g a_s^{3/2} F(\epsilon_{dd})$ where $F(\epsilon_{dd}) = \frac{1}{2}\int_0^\pi d\theta \sin\theta[1 + \epsilon_{dd}(3\cos^2\theta - 1)^{5/2}]$ and $\epsilon_{dd} = a_{dd}/a_s$.

Consider a small supersolid of only two clusters of atoms, thus we can make the two-mode ansatz for the total wavefunction, decoupling the spatial and temporal dependance

$$\psi(\mathbf{r}, t) = \psi_1(t)\phi_1(\mathbf{r}) + \psi_2(t)\phi_2(\mathbf{r}) \tag{3.4}$$

where the subscripts 1,2 are referred to the two clusters. This ansatz consider localized spatial wavefunction $\phi_{1,2}(\mathbf{r})$ and the absence of the external barrier creating the weak link makes it not obvious that this ansatz is going to recreate accurate results. In the limit of weak link, the two spatial wavefunctions have almost zero overlap, thus we impose the condition

$$\langle\phi_i|\phi_j\rangle = \delta_{ij} \quad \forall i = 1, 2 \qquad \phi_{1,2} \in \mathbb{R} \tag{3.5}$$

For the temporal parts, we are going to write them in the form

$$\psi_{1,2}(t) = \sqrt{N_{1,2}} e^{i\theta_{1,2}} \tag{3.6}$$

where $N_{1,2}$ are the populations in the two wells, while $\theta_{1,2}$ are the relative phases. This also assures that the total wavefunction is normalized to the total atom number N

$$\int d\mathbf{r}\ |\psi(\mathbf{r}, t)|^2 = |\psi_1|^2 + |\psi_2|^2 = N_1 + N_2 = N \quad , \tag{3.7}$$

which is a constant of the dynamics. We then replace the ansatz Eq. (3.4) in Eq. (3.3) and we project on ϕ_1 and on ϕ_2 in order to obtain two equations for the evolution of ψ_1 and ψ_2 (see Appendix B).

We shall now define the variables whose temporal evolution we want to investigate, namely the population and phase imbalance between the two clusters of atoms

$$Z \equiv \frac{N_1 - N_2}{N} \quad , \quad \Delta\theta \equiv \theta_2 - \theta_1 \quad . \tag{3.8}$$

such that

$$\begin{aligned} |\psi_1|^2 = N_1 &= \frac{N}{2}(1 + z) \\ |\psi_2|^2 = N_2 &= \frac{N}{2}(1 - z) \\ (\psi_1^*\psi_2 + \psi_1\psi_2^*) &= 2\sqrt{N_1 N_2}\cos\phi = N\sqrt{1 - z^2}\cos\phi \end{aligned} \tag{3.9}$$

It is now possible to write the system describing their evolution (see Appendix B)

$$\begin{cases} \dot{Z} = -\sqrt{1-Z^2}\sin\phi \\ \dot{\phi} = A + BZ + \frac{Z}{\sqrt{1-Z^2}}\cos\phi + C(1+Z)^{3/2} + D(1-Z)^{3/2} \end{cases} \tag{3.10}$$

where we have rescaled the time as $t \to 2K_{12}t$ and we have defined the adimensional coefficients

$$\begin{aligned} A &= \frac{K_{22}-K_{11}}{2K_{12}} + \frac{N\Big(U_1 - U_2 + D_1 - D_2\Big)}{4K_{12}} \\ B &= \frac{N\Big(U_1 + U_2 + D_1 + D_2\Big)}{4K_{12}} \\ C &= \frac{N^{3/2}L_1}{2^{5/2}K_{12}} \\ D &= -\frac{N^{3/2}L_2}{2^{5/2}K_{12}} \end{aligned} \tag{3.11}$$

as a function of the parameters

$$\begin{aligned} K_{ij} &\equiv -\int d\mathbf{r}\ \phi_i(\mathbf{r})\left(-\frac{\nabla^2}{2m} + V_t(\mathbf{r})\right)\phi_j(\mathbf{r}) \\ U_i &\equiv g\int d\mathbf{r}\ |\phi_\alpha(\mathbf{r})|^4 \\ D_i &\equiv \int d\mathbf{r}\ |\phi_\alpha(\mathbf{r})|^2 \int d\mathbf{r}'\ V_{dd}(|\mathbf{r}-\mathbf{r}'|)|\phi_\gamma(\mathbf{r}')|^2 \\ L_i &\equiv \gamma\int d\mathbf{r}\phi_i(\mathbf{r})^5 \quad . \end{aligned} \tag{3.12}$$

The variables z and $\Delta\theta$ are canonically conjugate with $\dot{z} = -\frac{\partial H}{\partial \Delta\theta}$ and $\dot{\Delta\theta} = \frac{\partial H}{\partial z}$, where the Hamiltonian is (see Appendix B)

$$H = AZ + B\frac{Z^2}{2} - \sqrt{1-Z^2}\cos\phi + \frac{2}{5}C(1+Z)^{5/2} + \frac{2}{5}D(1-Z)^{5/2} \tag{3.13}$$

3.2.3 Symmetric Josephson junction

A common case useful to simplify the coefficients Eq. (3.11) is the symmetric BJJ. This means that the spatial wavefunctions in the two wells are identical, even if centered in different positions. We can define

$$\begin{aligned} U_1 &= U_2 \equiv U \\ D_1 &= D_2 \equiv D \\ L_1 &= L_2 \equiv L \end{aligned} \tag{3.14}$$

so that

$$A = 0 \quad B = \frac{N\big(U+D\big)}{2K_{12}} \quad C = \frac{N^{3/2}L}{2^{5/2}K_{12}} \quad D = -C \quad . \tag{3.15}$$

The dynamical system Eq. (3.10) now depends only on the two parameters B and C and we can calculate the limit of small z, obtaining

$$\begin{cases} \dot{Z} = -\sqrt{1-Z^2}\sin\phi \\ \dot{\phi} = \Lambda' Z + \frac{Z}{\sqrt{1-Z^2}}\cos\phi \end{cases} \tag{3.16}$$

where $\Lambda = B+3C$. This is exactly the same system derived with a two-mode model in a BJJ [27, 104]. Also the Hamiltonian assumes the same form

$$H = \Lambda\frac{Z^2}{2} - \sqrt{1-Z^2}\cos\phi \tag{3.17}$$

In conclusion, the system Eq. (3.16) and its associated Hamiltonian are identical to the ones of a BJJ. The LHY adds its contribution to the mean-field one without changing the form of the system. As a consequence, the LHY does not induces any different phenomena from the BJJ at a Josephson dynamics level. Let us generalize the two-mode model to a $2M$-mode model in the next section.

3.2.4 2M-mode model

As already seen, the supersolid is characterized by a density modulation and we are taking the minima as weak links of JJs. It thus appears as a linear array of many weakly connected clusters. We can generalize the two-mode model associating to each cluster of atoms a localized wavefunction $\psi_j = \sqrt{N_j}\exp(i\theta_j)$ with population N_j and phase θ_j. The population-phase dynamics following a quench of these variables is described by a 2M-mode model

$$\begin{aligned} i\frac{\partial\psi_1}{\partial t} &= (E_1 + U_1N_1)\psi_1 - K_{12}\psi_2 \\ &\vdots \\ i\frac{\partial\psi_j}{\partial t} &= (E_j + U_jN_j)\psi_j - K_{j,j-1}\psi_{j-1} - K_{j,j+1}\psi_{j+1} \\ &\vdots \\ i\frac{\partial\psi_{2M}}{\partial t} &= (E_{2M} + U_{2M}N_{2M})\psi_{2M} - K_{2M,2M-1}\psi_{2M-1} \end{aligned} \tag{3.18}$$

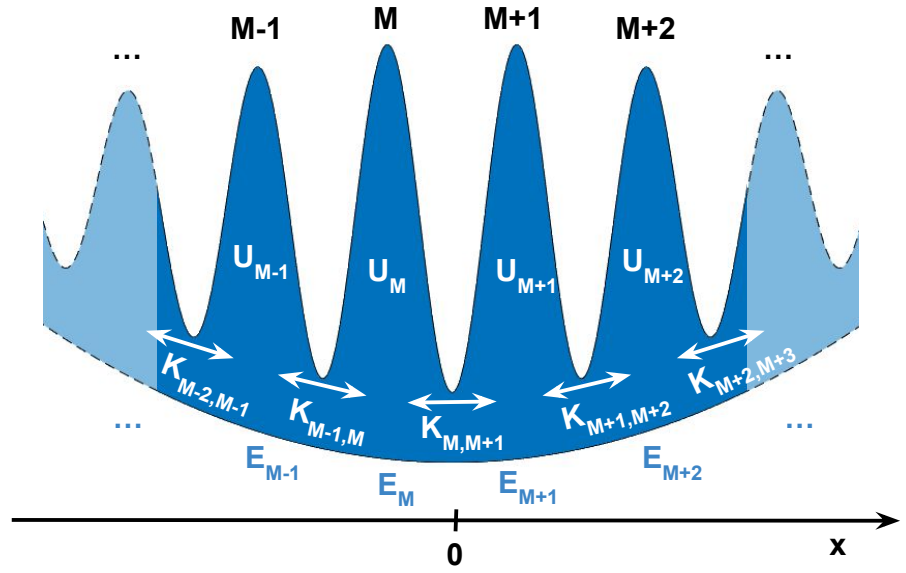

Figure 3.1: Sketch of a supersolid as a linear array of $2M$ clusters. For a pictorial representation, the density is vertically displaced to follow the harmonic trap along the x direction. The jth cluster has its on-site interaction parameter U_j and the couplings with adjacent clusters $K_{j-1,j}$ and $K_{j,j+1}$ and an energy offset E_j.

where U_j is the on-site interaction of the jth cluster and $K_{j,j-1}$ is the coupling coefficient between clusters j and $j-1$ [23, 27]. The terms E_j account for the energy offset of the jth cluster due to the external trapping [27], see Figure 3.1. Due to the strong interactions characterizing the gas and the lack of external energy potentials confining the clusters, it is not a priori obvious that it is possible to identify regimes of parameters where the model Eq. (3.18) leads to accurate results. In the following, we identify analytically interesting dynamical regimes predicted by Eq. (3.18) and compare them directly with numerical integration of the complete eGPE. As it will be discussed below, the set of Eq. (3.18) shows different dynamical regimes among which we identify both josephson-like oscillations and MQST. These are analogous to those predicted [27] and experimentally observed in bosonic Josephson junctions [28, 29, 112]. We emphasise that in the present study, no external barrier was imposed.

We consider a symmetric clusters array with $E_{j>M} = E_{2M-(j-1)}$ and $U_{j>M} = U_{2M-(j-1)}$. We study the dynamics of the population imbalance

$$Z \equiv \frac{N_{M+1} - N_M}{N_{M+1} + N_M} \tag{3.19}$$

and phase difference

$$\Delta\theta \equiv \theta_{M+1} - \theta_M \tag{3.20}$$

between the central clusters, labelled as M and $M+1$. Under the condition

$$\dot{N}_{M+1} - \dot{N}_M = \alpha\left(\sum_{j=1}^{M-1} \dot{N}_j - \sum_{k=M+2}^{2M} \dot{N}_k\right), \tag{3.21}$$

where α is a constant, Eq. (3.18) reduce to (see Appendix C)

$$\begin{aligned} \dot{Z} &= 2K\frac{\alpha}{\alpha-1}\sqrt{1-z^2}\sin(\Delta\theta) \\ \dot{\Delta\theta} &= -U(N_{M+1}+N_M)z \end{aligned}, \tag{3.22}$$

where $K \equiv K_{M,M+1}$ and $U \equiv U_M$. These equations have the form of the standard bosonic Josephson equations [27] with two important differences. (i) The lateral clusters (1 to $M-1$ and $M+2$ to $2M$) enter the dynamics renormalizing the coupling coefficient K. (ii) Differently from previous studies [27–29], there is no externally-imposed weak link: the JJ is here self-induced thanks to the supersolid intrinsic density modulation.

In order to study Josephson dynamics, we need to start the system in an out-of-equilibrium condition, specifically an antisymmetric initial quench of populations and phases. This can be achieved by adding an external sinusoidal potential with half-period equal to the distance between clusters, thereby creating population imbalances with opposite signs in subsequent clusters. Using this kind of quench and in the regime of small oscillations, we can write the ansatzs for populations and phases

$$\begin{aligned} N_j(t) &= N_j^0 + (-1)^{j+1}\Delta_j \sin(\omega_J t) \\ \Delta\theta_{j+1,j}(t) &= (-1)^j \delta\theta \cos(\omega_J t) \end{aligned} \tag{3.23}$$

where N_j^0 represents the equilibrium population, ω_J the Josephson frequency and $\Delta\theta_{j+1,j} \equiv \theta_{j+1} - \theta_j$. The parameters Δ_j and $\delta\theta$ are the amplitudes of the oscillations. We have supposed a Josephson-like dynamics where both N_j and $\Delta\theta$ oscillates with the same frequency ω_J and a relative temporal shift of $\pi/2$. The signs come from the antisymmetric quench we have chosen. Subsituting the ansatzs Eq. (3.23) in the model Eq. (3.18), we obtain some conditions on the interacting and tunnelling parameters involved in the system, in particular on the ratio between interacting

parameters of neighbour clusters (see Appendix D)

$$\begin{aligned} \frac{U_1}{U_2} &= 1 + \frac{K_{23}}{K_{12}}\sqrt{\frac{N_3^0}{N_1^0}} \\ \frac{U_j}{U_{j+1}} &= \frac{1 + \frac{K_{j+1,j+2}}{K_{j,j-1}}\sqrt{\frac{N_{j+2}^0}{N_j^0}}}{1 + \frac{K_{j,j-1}}{K_{j,j+1}}\sqrt{\frac{N_{j-1}^0}{N_{j+1}^0}}}, \quad \forall j. \end{aligned} \tag{3.24}$$

This conditions provide an explicit expression for α to be found (see Appendix D)

$$\alpha = \left(\sum_{j=1}^{M-1}(-1)^{j-M+1}\frac{U_M}{U_j}\right)^{-1}. \tag{3.25}$$

Upon the validity of Eq. (3.24), we can characterize the small oscillations regime, finding the Josephson frequency (see Appendix D)

$$\omega_J = \sqrt{2K\frac{\alpha}{\alpha-1}U(N_{M+1}+N_M)}. \tag{3.26}$$

This expression is analogue to the standard BJJ, but with the presence of the α coefficient which renormalizes the tunnelling coefficient K. It is interesting to notice that Eq. (3.22) predicts also the MQST regime, exclusive to BJJ (see subsection 2.4.1). This regime is characterized by the oscillation of Z around a non-zero value and a running phase over the interval [0,2π]. The transition from the small oscillations regime to the MQST one is marked by a critical value Z_c of the initial population imabalance, i.e. the value of Z at $t = 0$. The system enter the MQST regime when $Z(t = 0)$ exceeds the value (see Appendix C)

$$Z_c = \sqrt{\frac{8K\frac{\alpha}{\alpha-1}}{U(N_M+N_{M+1})}}. \tag{3.27}$$

To be noticed that once again the expression is analogue to the one for the BJJ, but with α coefficient renormalizing the coupling K in the same way as for the Josephson frequency Eq. (3.26).

3.3 Numerical methods

We have numerically integrated the eGPE Eq. (3.3) with a 4th order Runge-Kutta method (see Appendix E). Ground states are evaluated using an imaginary time propagation implemented by a dynamical time step adjustment technique, that we are going to discuss in the next subsections. On the other side, dynamics are numerically integrated by evolving the eGPE in real time, thus without the adjustable time step. The application of these numerical methods requires the discretization of the eGPE that is quite standard (see Appendix E), but the dipolar term needs a small trick that we are going to see below.

3.3.1 Imaginary time propagation

Imaginary time propagation (ITP) is a widely used numerical method [113–116] to find the ground state of a quantum system described by a Schrödinger-like time-dependent equation such as:

$$i\hbar\frac{\partial\psi(x,t)}{\partial t} = H\psi(x,t) \tag{3.28}$$

The hamiltonian is an hermitian operator, so that its eigenvalues $E_0 \leq E_1 \leq E_2 \ldots$ are real and non negative, and the corresponding eigenfunctions $\phi_i(x)$ can be chosen to form a real orthonormal basis on its domain. ITP is based on the Wick rotation [117], a mathematical method that consists in substituting a real variable with an imaginary one, i.e. in a rotation of $\pi/2$ in the complex plane. In our case, it consists in the substitution $t \to i\tau$, transforming the Schrödinger equation Eq. (3.28) into a diffusion type one:

$$-\hbar\frac{\partial\psi(x,\tau)}{\partial\tau} = H\psi(x,\tau) \tag{3.29}$$

whose formal solution is:

$$\psi(x,\tau) = e^{-\frac{H}{\hbar}\tau}\psi(x,0) \tag{3.30}$$

Expanding the initial wavefunction $\psi(x,0) \equiv \psi_0(x)$ in the complete basis of eigenfunctions:

$$\psi_0(x) = \sum_i c_i\phi_i(x) \tag{3.31}$$

the imaginary time evolution Eq. (3.30) becomes:

$$\psi(x,\tau) = e^{-\frac{H}{\hbar}\tau}\sum_i c_i\phi_i(x) = \sum_i c_i e^{-\frac{E_i}{\hbar}\tau}\phi_i(x) \tag{3.32}$$

Evidently, when propagated forward in imaginary time, each eigenfunction decays exponentially, with the rate of decay proportional to its energy. Indeed, all the states other than the ground state will die off exponentially quickly even compared to how quickly the ground state is vanishing:

$$\frac{\psi(x,\tau)}{\psi(x,0)} \propto e^{-\tau(E_i - E_0)} \tag{3.33}$$

Therefore, for a sufficiently long time integration, the only asintotically appreciable contribution to $\psi(x,\tau)$ is given by the lowest eigenvalue, namely the ground state E_0:

$$\psi(x,\tau) \to c_0 e^{-\frac{E_0}{\hbar}\tau}\phi_0(x) \qquad \tau \to +\infty \tag{3.34}$$

Ultimately, selecting a random initial wave function at $\tau = 0$ and allowing it to evolve in imaginary time will lead to convergence with the true ground state wave function. The greater the similarity between the initial function and the ground state, the more rapidly convergence will be achieved.

3.3.2 Dynamic time step adjustment method

We have integrated the Eq. (3.3) with a standard 4th order Runge Kutta method (see Appendix E), but implemented by an adaptive stepsize algorithm. We have used the technique proposed by Lehtovaara *et al.* [114]. It basically consists in using two different time steps for the integration. At first glance, it could seem like a waste of time to double the calculation, but we will see that it is not. In fact, the algorithm makes the code choosing the best time step and adjusts it dynamically.

Considering the integration of the Schrödinger equation in imaginary time, every iteration we take a longer time step $dt_L = \Delta\tau$ and a shorter one $dt_S = \chi\Delta\tau$, where the factor χ is changing every step. Starting from the first iteration, we have:

$$\begin{cases} dt_L = \Delta\tau \\ dt_S = \frac{1}{2}\Delta\tau \end{cases} \tag{3.35}$$

giving two different solutions ψ_L and ψ_S with which we calculate the two energies:

$$\begin{cases} E_L = \langle\psi_L|\,\hat{H}\,|\psi_L\rangle \\ E_S = \langle\psi_S|\,\hat{H}\,|\psi_S\rangle \end{cases} \tag{3.36}$$

where we have assumed that the wave functions are normalized to 1. Since we are searching for the ground state with the ITP method, the energy must decrease

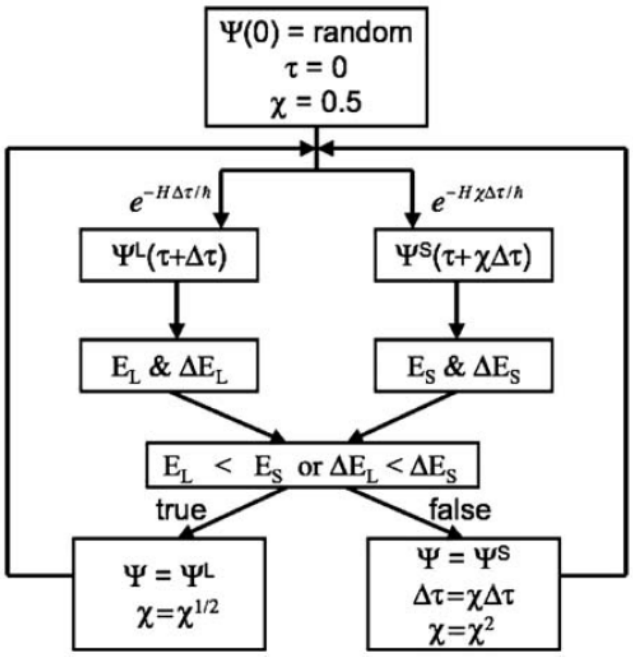

Figure 3.2: Dynamic time step adjustment algorithm: every iteration the code integrates using a longer time step $\Delta\tau_L$ and a shorter one $\Delta\tau_S$. The chosen time step is the one that gives the smaller energy. Figure adapted from Lehtovaara *et al.*[114]

exponentially to the right value. Therefore, we choose the time step size that gives the smaller energy as the new dt_L. This is the transcription in the code written using Matlab:

```
1     if En_totL(ip) < En_totS(ip)
2         En_tot(ip) = En_totL(ip);
3         chi = sqrt(chi);
4         dtS = chi*dtL;
5         Phi0 = PhiL;
6     else
7         En_tot(ip) = En_totS(ip);
8         dtL = dtS;
9         chi = chi^2;
10        dtS = chi*dtL;
11        Phi0 = PhiS;
12    end
```

If dt_L gives the smaller energy, the next step dt_L remains the same, but $\chi = \sqrt{\chi}$, so that the dt_S is kept smaller than dt_L but bigger than before: $dt_S = \frac{dt_L}{\sqrt{2}} > \frac{dt_L}{2}$. This because the trend is to prefer having a longer dt. On the other side, if dt_S gives the smaller energy, dt_S becomes the new dt_L and $\chi = \chi^2$, so that the new dt_S is $\frac{dt_L}{4}$. This time, instead, is because the trend is to prefer a smaller dt. The code makes this choice every iteration, but in general this allowed it only to keep the same dt or decreasing it, never increasing it. So, the initial time step need to be chosen as large as possible, so as not to make it unstable. In particular, we can use the condition stability for a 3D diffusion-type equation:

$$dt \leq \frac{dx^2 + dy^2 + dz^2}{2D} \tag{3.37}$$

where D is the diffusion coefficient that in our case is $D = \frac{\hbar^2}{2m}$, so that we have:

$$dt \leq (dx^2 + dy^2 + dz^2)\frac{m}{\hbar} \sim 6.54 \cdot 10^{-4} \tag{3.38}$$

where we have used values coming from our grid (see Appendix E). Since this, we have used an initial time step:

$$dt = 10^{-3}\ \frac{2\pi}{\omega_x} s \sim 5.41 \cdot 10^{-5} s \tag{3.39}$$

defined with respect to the trap period $T_x = \frac{2\pi}{\omega_x}$ in the direction where the supersolid modulation is detected.

Where is the gain? To achieve the same accuracy of this method using only one fixed time step, we should use the last time step used in the adaptive method, that is the smallest one. This would cause the use of a large number of iterations. On the other side, the adaptive method usese a bigger initial time step, going decreasing it when the algorithm has roughly found the desired minimum. Only at that point, it decreases the size of the time step until the desired precision.

3.3.3 Dipolar term

The dipolar interaction is long-range and contains an integral

$$\Phi_{dd}(\mathbf{r}, t) = \int d\mathbf{r}' V_{dd}(|\mathbf{r} - \mathbf{r}'|)|\phi(\mathbf{r}', t)|^2 \tag{3.40}$$

so it is computationally expensive to evaluate it over the full space grid. A smart way to compute it consists in noticing that it is a convolution and evaluate it in the

Fourier space. In fact, the convolution theorem states that the Fourier transform of a convolution of two functions is the product of the Fourier transforms of the two functions [118]

$$\mathcal{F}[f * g] = \mathcal{F}[f] \cdot \mathcal{F}[g] \tag{3.41}$$

where the convolution is defined as

$$f * g = \int d\mathbf{r} f(\mathbf{r}) g(\mathbf{r} - \mathbf{r}') \tag{3.42}$$

The Eq. (3.40) can therefore be rewritten as:

$$\Phi_{dd}(\mathbf{r}, t) = \mathcal{F}^{-1}\Big[\mathcal{F}[V_{dd}](\mathbf{k}) \cdot \mathcal{F}[n](\mathbf{k})\Big] \tag{3.43}$$

where $\mathcal{F}^{-1}$ is the inverse Fourier transform and we have called n the density $|\phi(\mathbf{r}, t)|^2$. The Fourier transform of the dipolar interaction can be derived analitically (see Appendix F), thus in the code we need to Fourier transform the density n. After this, we multiply the two terms and calculate the inverse Fourier transform of this product.

3.3.4 Convergence criterion

We have all the necessary ingredients to evolve iteratively the 4th order Runge-Kutta method with the dynamic time step adjustment technique. However, these iterations necessitate a convergence criterion that indicates when the code should stop. To establish this criterion, we use the total energy. We have already included the energy calculation in the dynamic time step adjustment technique as

$$E^n_{tot} = E^n_{kin} + E^n_{h.o.} + E^n_{contact} + E^n_{dd} + E^n_{LHY} \tag{3.44}$$

where

$$\begin{aligned}
E^n_{kin} &= \langle\phi_n| \hat{K} |\phi_n\rangle = \int d\mathbf{r} \frac{\hbar^2}{2m} |\nabla n(\mathbf{r})|^2 \\
E^n_{h.o.} &= \langle\phi_n| \hat{V}_{h.o.} |\phi_n\rangle = \int d\mathbf{r}\ \frac{1}{2} m(\omega_x^2 x^2 + \omega_y^2 y^2 + \omega_z^2 z^2) n(\mathbf{r}) \\
E^n_{contact} &= \langle\phi_n| \hat{V}_{contact} |\phi_n\rangle = \frac{1}{2} g \int d\mathbf{r} n(\mathbf{r}) \\
E^n_{dd} &= \langle\phi_n| \hat{V}_{dd} |\phi_n\rangle = \frac{1}{2} \int d\mathbf{r} \int d\mathbf{r}' V_{dd}(|\mathbf{r} - \mathbf{r}'|) n(\mathbf{r}') n(\mathbf{r}) \\
E^n_{LHY} &= \langle\phi_n| \hat{V}_{LHY} |\phi_n\rangle = \frac{2}{5} \gamma(\epsilon_{dd}) \int d\mathbf{r} n(\mathbf{r})^{5/2}
\end{aligned} \tag{3.45}$$

and $n(\mathbf{r}) = |\phi(\mathbf{r})|^2$ is the density calculated at the nth step. Every iteration, this energy is compared to the one calculated at the step before

$$check \equiv \frac{|E^n_{tot} - E^{n-1}_{tot}|}{E^{n-1}_{tot}} \quad . \tag{3.46}$$

Iterations keep going until this *check* variable reaches a satisfactory level of accuracy without requiring an excessive amount of computational time.

3.4 Numerical results

We compare the predictions of Eq. (3.18) and Eq. (3.22) with the numerical integration of the eGPE Eq. (3.3) describing our dipolar supersolid.

The choice of system parameters was dictated by our desire to study a single JJ, so a two-mode system. We actually found an experimentally relevant regime with a ground state with two clusters. This can be realized with an harmonic trap with frequencies $\omega_{x,y,z} = (20,50,50)$Hz and $N = 2 * 10^4$ atoms, but in this case the Josephson dynamics is unstable. The initial population imbalance that we impose in order to starts the dynamics, couples many modes of many different kind and with a lot of frequencies in the dynamics. The next reasonable choice was therefore to look for a four-clusters system and it is the one we are going to analyze below. We can conclude that it seems like the presence of the lateral clusters is needed because it stabilizes the Josephson dynamics, which in this case clearly emerges as a single frequency mode in the system. This observation is in line with the hypothesis Eq. (3.21) we had to assume in order to be able to write the Josephson equations 3.22 from the general 2M-mode model Eq. (3.18). Indeed, the hypothesis is a kind of balance (even if there is the prefactor α) between the Josephson current of central clusters and the one of all the other lateral clusters.

3.4.1 System description

We integrate Eq. (3.3) considering $N = 35000$ atoms of ^{162}Dy in an harmonic trap with frequencies $\omega_{x,y,z} = 2\pi\ (18.5, 53, 81)$ Hz [16]. The polarization direction is $\hat{z}$, which is the direction of stronger confinement, in order to induce the roton instability [79] described in subsection 1.7.2, while the density modulation is formed along $\hat{x}$, the direction with weakest confinement.

The supersolid density modulation is one-dimensional, but the trap tends to be

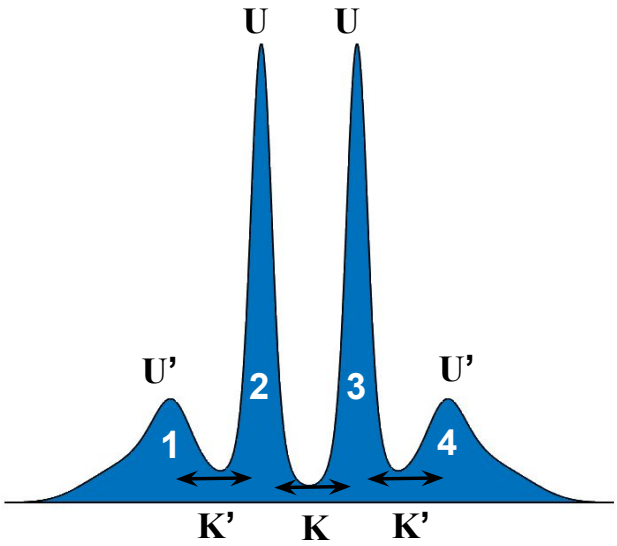

Figure 3.3: Density integrated profile $n(x)$ of supersolid at $\epsilon_{dd} = 1.4$ from eGPE. The indices of the four clusters goes from left to right. Clusters $2-3$ have an interacting parameter U and clusters $1-4$ have U'. The coupling coefficients are K for the central one between 2 and 3 and the others between 1 and 2 and between 3 and 4 are K'. Lateral clusters are smaller due to the energy offset E^0 given by the harmonic trapping.

bi-dimensional, causing a discontinuous phase transition from the superfluid BEC regime to the indipendent droplets (or droplets crystal) [111, 119].

Density modulation are found for $\epsilon_{dd} \gtrsim 1.4$ and the specific combination of number of atoms and trap frequencies gives rise to a 4-clusters supersolid. In Figure 3.3 is plotted the one dimensional integrated density $n(x) \equiv \iint dy\, dz\, n(x, yz)$, that is the three-dimensional density $n(x, y, z)$ integrated along the directions transverse to the one where the density modulation develops (x). We can notice the smaller size of the lateral clusters due to the presence of an energy offset E^0 given by the harmonic trapping potential.

3.4.2 Four mode model

This system requires a theoretical 4-mode model ($M = 2$) to compare the dynamics predicted by the eGPE Eq. (3.3) and the theoretical model Eq. (3.18). Let us start

writing the evolution of populations and phase differences in the case $M = 2$

$$\begin{aligned}
\dot{N}_1 &= -2K'\sqrt{N_1 N_2}\sin\Delta\theta_{21} \\
\dot{N}_2 &= 2K'\sqrt{N_1 N_2}\sin\Delta\theta_{21} - 2K\sqrt{N_2 N_3}\sin\Delta\theta_{32} \\
\dot{N}_3 &= 2K\sqrt{N_2 N_3}\sin\Delta\theta_{32} - 2K'\sqrt{N_3 N_4}\sin\Delta\theta_{43} \\
\dot{N}_4 &= 2K'\sqrt{N_3 N_4}\sin\Delta\theta_{43} \\
\Delta\dot{\theta}_{21} &= E^0 + U'N_1 - UN_2 \\
\Delta\dot{\theta}_{32} &= U(N_2 - N_3) \\
\Delta\dot{\theta}_{43} &= -E^0 - U'N_4 + UN_3
\end{aligned} \tag{3.47}$$

where we have defined the parameters as in Figure 3.3, so that the prime symbol refers to the lateral clusters. The parameter E^0 refers to the energy offset of the lateral clusters with respect to the central ones. Phase differences are defined as $\Delta\theta_{ij} \equiv \theta_j - \theta_i$ where $i, j = 1,2,3,4$ are the indices of the clusters, as in Figure 3.3. The condition Eq. (3.21) is

$$\dot{N}_3 - \dot{N}_2 = \alpha\left(\dot{N}_1 - \dot{N}_4\right) \tag{3.48}$$

so that we can derive the Josephson equations for the central clusters $(2-3)$. Writing down the evolution of the population imbalance

$$\begin{aligned}
\dot{N}_3 - \dot{N}_2 &= 4K\sqrt{N_2 N_3}\sin\Delta\theta_{32} - 2K'\sqrt{N_3 N_4}\sin\Delta\theta_{43} - 2K'\sqrt{N_1 N_2}\sin\Delta\theta_{21} \\
&= 4K\sqrt{N_2 N_3}\sin\Delta\theta_{32} - \dot{N}_4 + \dot{N}_1 \\
&= 4K\sqrt{N_2 N_3}\sin\Delta\theta_{32} + \frac{\dot{N}_3 - \dot{N}_2}{\alpha}
\end{aligned} \tag{3.49}$$

so that

$$\begin{aligned}
\dot{N}_3 - \dot{N}_2 &= 4K\frac{\alpha}{\alpha - 1}\sqrt{N_2 N_3}\sin\Delta\theta_{32} \\
\Delta\dot{\theta}_{32} &= -U(N_3 - N_2)
\end{aligned} \tag{3.50}$$

where the second equation is exactly from Eq. (3.47). The fractional population imbalance and phase difference are defined as

$$Z \equiv \frac{N_3 - N_2}{N_{23}} \quad \Delta\theta \equiv \theta_2 - \theta_3 \tag{3.51}$$

where the denominator is the sum of the central equilibrium populations $N_{23} \equiv N_2(0) + N_3(0)$. The system of equations for Z and $\Delta\theta$ is

$$\begin{aligned} \dot{Z} &= 2K\frac{\alpha}{\alpha-1}\sqrt{1-Z^2}\sin\Delta\theta \\ \dot{\Delta\theta} &= -UN_{23}Z \end{aligned} \tag{3.52}$$

that is the system Eq. (3.22) with $M = 2$.

3.4.3 Josephson dynamics and MQST

In order to excite Josephson dynamics, we start the system in a non-symmetric equilibrium condition achieved by finding the ground states with the addiction of an external sinusoidal potential with half-period equal to the distance between clusters, thereby creating population imbalances with opposite signs in subsequent clusters (see Figure 3.6). This potential can be provided experimentally by an optical lattice. We then numerically evolve the system in real time, examining the populations and phases of each cluster, defined as

$$N_j(t) = \int_{cluster j} dx\ n(x,t) \quad \theta_j = \int_{cluster j} dx\ \theta(x,t) \tag{3.53}$$

where the integrated 1d densities and phases are $n(x,t) = \int dy\ dz\ |\psi(\mathbf{r},t)|^2$ and $\theta(x,t) = \frac{\int dy\ dz\ \phi(\mathbf{r},t)\ |\psi(\mathbf{r},t)|^2}{\int dy\ dz\ |\psi(\mathbf{r},t)|^2}$. The integrals on the transverse directions $y-z$ are performed over the whole box, while on the x-direction is performed over the cluster jth, specifically on the interval between the two minima in the density modulation outlining the limits of the cluster. We have weighted the 1d phase profile with the density to suppress noise at the boundaries, where the density goes to zero.

In Figure 3.4 and Figure 3.5 we plot the dynamics of the Josephson variables, Z (blue lines) and $\Delta\theta$ (red lines) for $\epsilon_{dd} = 1.43$ in the supersolid regime but with different values of the initial population imbalance $Z_0 \equiv Z(t=0)$. In Figure 3.4 we plot an example of the small oscillations regime, with $Z_0 = -0.02$. Density and phase oscillate harmonically in time around the equilibrium position $Z = 0$ and $\Delta\theta = 0$ with the same frequency, but a relative shift of $\pi/2$, as in the standard Josephson dynamics. The insets show three density profiles at three different instants of time showing the symmetric exchange of population between the two central clusters. These oscillations are well reproduced by the theoretical model, plotted here as dashed lines. In Figure 3.5 is plotted the dynamics for $Z_0 = -0.18$ and Z oscillates around a nonzero value, while $\Delta\theta$ runs over the interval $[0,2\pi]$.

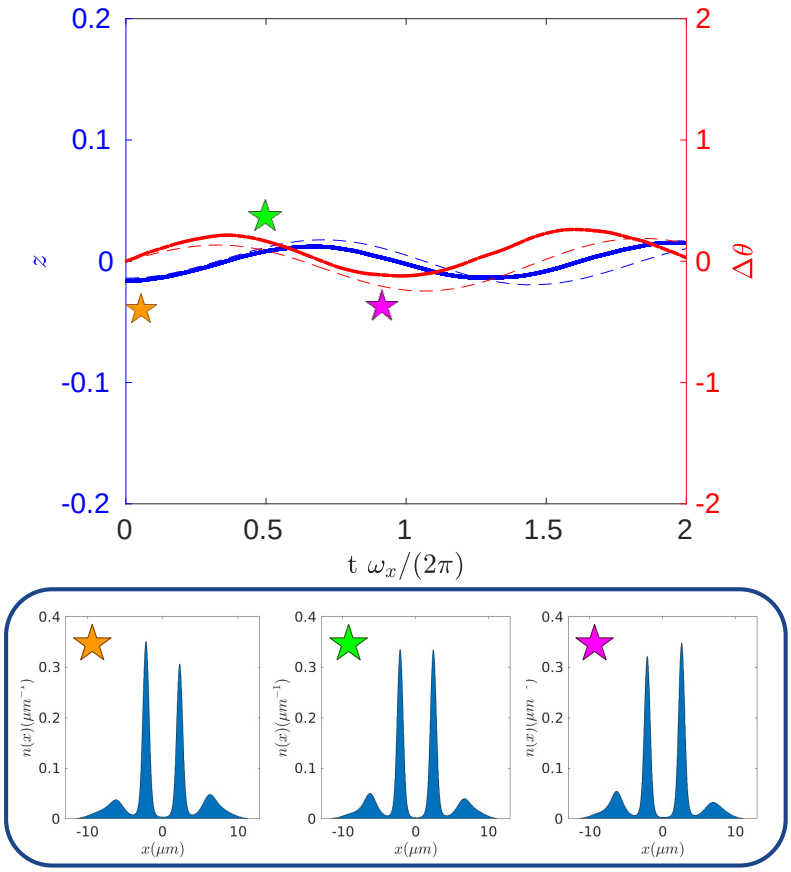

Figure 3.4: Evolution in time of the population imbalance Z (blue lines and left axis) and phase difference $\Delta\theta$ (red lines and right axis) in the small oscillations regime. Solid lines are the numerical integration of the eGPE, while dashed lines are the integration of the model Eq. (3.52). Both variables oscillate around zero with the same frequency and a relative shift of $\pi/2$. On the bottom, there are three density profiles at three different times $t = (5,22,38)$ms corresponding to the limiting behaviour of the oscillation, showing the symmetric exchange of population between the two central clusters. The coloured stars indicate the instant of time where the snapshots were taken.

This effect, called MQST, is inherited from the bosonic JJs and is a self locking of the population on one side due to the nonlinear interaction. The three density profiles in the insets show the nonsymmetric exchange of population between clusters. The population of the bigger cluster starts to move among the smaller one, but the phase difference stops this balancing, sending them back. In a classical pendulum analogy [27], with Z as the angular momentum and $\Delta\theta$ as the tilt angle, an high

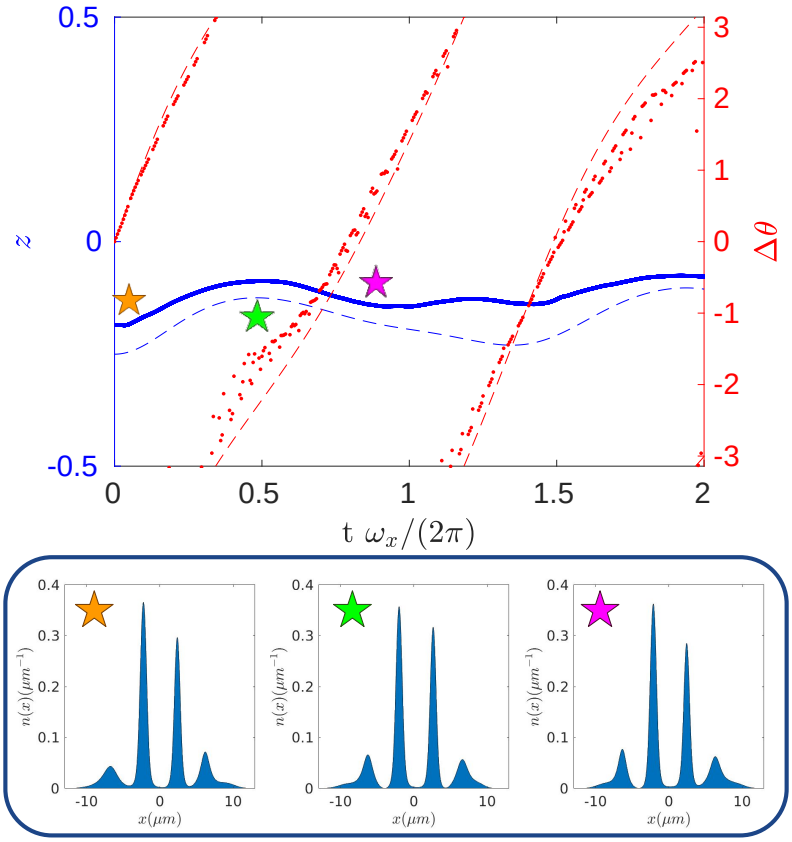

Figure 3.5: Evolution in time of the population imbalance Z (blue lines and left axis) and phase difference $\Delta\theta$ (red lines and right axis) in the MQST regime. Solid blue line and dotted red line are the numerical integration of the eGPE, while dashed lines are the integration of the model Eq. (3.52). Z oscillates around a nonzero value, while $\Delta\theta$ runs over the whole interval $[0,2\pi]$. On the bottom, there are three density profiles at three different times $t = (8,27,49)$ms corresponding to the limiting behaviour of the oscillation, showing the non-symmetric exchange of population between the two central clusters. The coloured stars indicate the instant of time where the snapshots were taken.

Z causes the pendulum to not oscillate around the equilibrium position, like the small oscillation regime, but to fully rotate.

Dashed lines in Figure 3.4 and Figure 3.5 are the direct integration of Eq. (3.18) with the interaction and coupling parameters values extracted using the data from the eGPE and by fitting the model to the data with a procedure that we are going to explain.

First of all, we derive the value of α from the equality between currents Eq. (3.48).

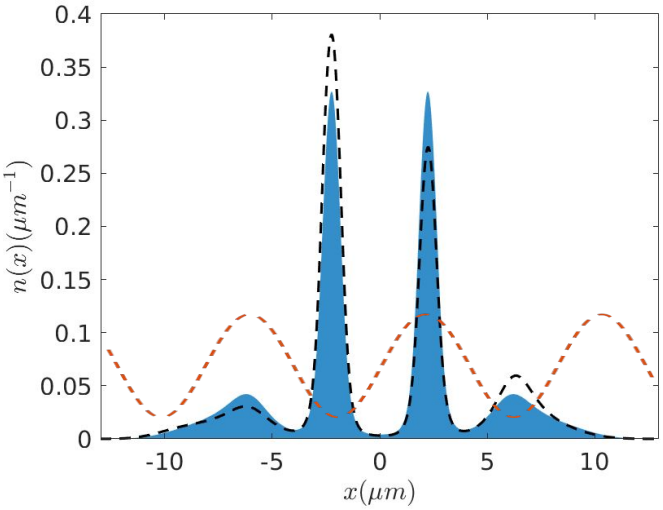

Figure 3.6: Excitation of a Josephson dynamics. Blue area is the equilibrium density profile of the supersolid, while the black dashed line is the density profile with a population imbalance. This is created by imposing a sinusoidal potential, here represented with a red dashed line. Amplitude of the potential is in arbitrary units.

In Figure 3.7 are plotted the left (orange dots) and right (green dots) hand sides of Eq. (3.48) with $\alpha = 2$. We find that this value of α gives a good agreement between left and right hand side of the hypothesis both in the regime of small oscillations (top panel) and MQST (bottom panel).
At this point, we derive the central coupling K and interacting U coefficients, through the fitting of the linearized Eq. (3.52), using $\alpha = 2$

$$\begin{aligned} \dot{Z} &= 4K\Delta\theta \\ \dot{\Delta\theta} &= -UN_{23}Z \end{aligned} \tag{3.54}$$

These equations are valid for $Z \ll 1$ and $\Delta\theta \ll 1$. In Figure 3.8, an example of the current-phase relation at the interaction $\epsilon_{dd} = 1.41$ for different Z_0 is shown. On the left, a small Z_0 results in a linear relation as in Eq. (3.54) and on the right, for higher Z_0, is the characteristic Josephson sinusoidal current-phase relation Eq. (3.52). Green dots are numerical results from the eGPE, while orange line is the fitting curve.

The parameters K' and U' are derived from fitting the equations for $\dot{N}_1$ and $\dot{\theta}_4 - \dot{\theta}_1$ (see Eq. (3.47))

$$\begin{aligned} \dot{N}_4 &\cong 2K'\sqrt{N_3N_4}\Delta\theta_{43} \\ \dot{\theta}_4 - \dot{\theta}_1 &= \Delta\theta_{21} + \Delta\theta_{32} + \Delta\theta_{43} = U'(N_1 - N_4) \end{aligned} \tag{3.55}$$

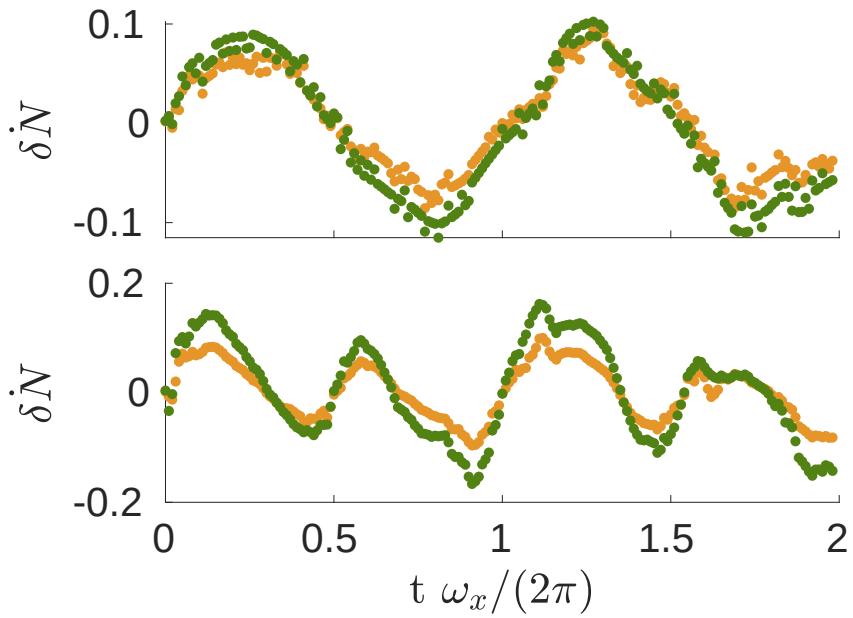

Figure 3.7: Verification of Eq. (3.48) in the regime of small oscillations (top panel) at $\epsilon_{dd} = 1.41$ and MQST (bottom panel) at $\epsilon_{dd} = 1.46$. Green and orange dots are respectively the right and left hand side of Eq. (3.48) with $\alpha = 2$, thus $\dot{N}_3 - \dot{N}_2$ and $2(\dot{N}_1 - \dot{N}_4)$.

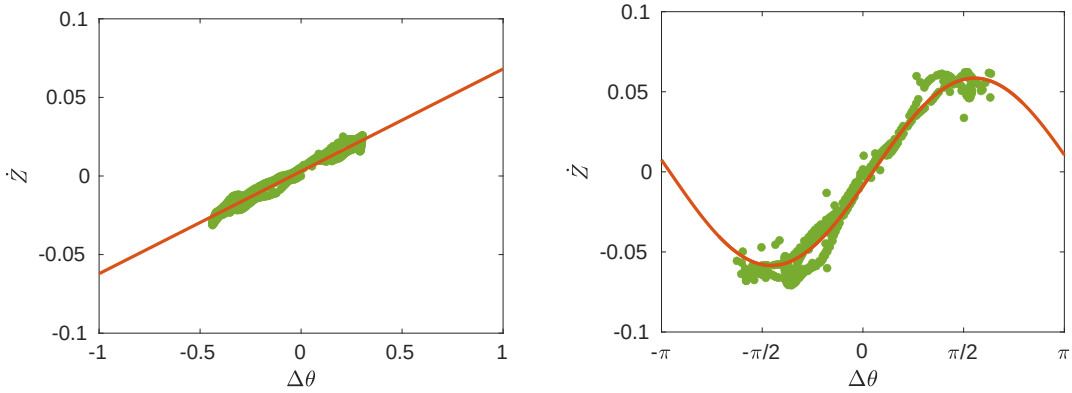

Figure 3.8: Current-phase relation $\dot{Z} - \Delta\theta$ at fixed interaction $\epsilon_{dd} = 1.41$ and different initial population imbalance Z_0. Left panel has a smaller Z_0 and a linear fitting, thus for higher Z_0 the curve becomes sinusoidal. Green dots are numerical integration of the eGPE and orange line is the fitting curve.

We found $K \cong 0.015$ $(0.007 \div 0.03)$, $UN_{23} \cong 10$ $(7 \div 13)$, where $N_{tot} = N_1 + N_2 + N_3 + N_4$, all in units of $\hbar\omega_x$. Lateral parameters with respect to the central ones

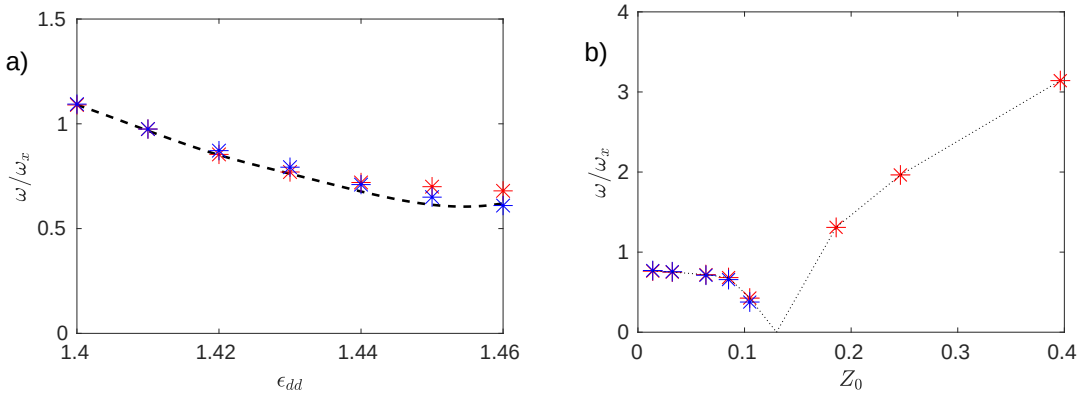

Figure 3.9: Josephson frequencies. Numerical results from eGPE for the evolution of Z (blue asterisks) and $\Delta\theta$ (red asterisks). The black dashed line is the theoretical frequency given by Eq. (3.26). a) Frequencies at fixed $Z_0 \cong 0.01$ as a function of the interaction. b) Frequencies for $\epsilon_{dd} = 1.43$ as a function of the initial population imbalance Z_0. Dotted line is a guide to the eye. The increase of the frequency happens entering the MQST regime, as in a BJJ.

assume the values $U'/U \cong 2.2$ $(1.7 \div 2.7)$ and $K'/K \cong 1.1$ $(0.6 \div 1.6)$.
These values allow us to check if the value of α found with the Eq. (3.48) (see Figure 3.7) agrees with Eq. (3.25) in our four-mode model

$$\alpha = \frac{U'}{U} \quad . \tag{3.56}$$

The agreement is good and thus the hypothesis Eq. (3.48) is verified.

We further extend the comparison of numerical results with the model through the analysis of the frequencies. In Figure 3.9a are shown the Josephson frequencies in the small oscillations regime $Z_0 \cong 0.01$ as a function of the interaction ϵ_{dd}. They are obtained from the fit of the Josephson oscillations in the eGPE Eq. (3.3) (blue and red asterisks for Z and $\Delta\theta$) and agree well with the theoretical expression in Eq. (3.26) (black dashed line). The decrease of this frequency distinguishes it from a different mode, for example a dipole mode along x that would have remained at $\omega/\omega_x = 1$. In Figure 3.9b is shown the trend of the frequencies for $\epsilon_{dd} = 1.43$ as a function of the initial population imbalance Z_0. Blue and red asterisks correspond to numerical frequencies from eGPE of Z and $\Delta\theta$ respectively, while the black dotted line is a guide to the eye. Numerical frequencies initially stay constant, but than decrease and re-increase rapidly as we enter the MQST regime, similar to a standard BJJ [27, 28].

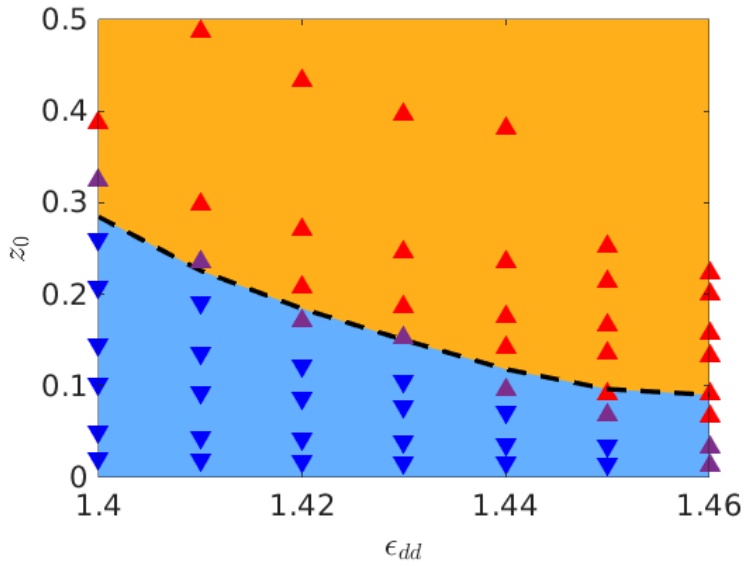

Figure 3.10: Phase diagram showing the transition from the small oscillations regime $z < z_c$ (blue region) to MQST $z > z_c$ (orange region) as a function of the interaction strength ϵ_{dd} and z_0. Each triangle corresponds to the numerical result of the eGPE: blue downward triangles correspond to balanced population-phase oscillations analogue to those of Figure 3.4, red upward triangles correspond to self-trapped oscillations with running phase analogue to those of Figure 3.5 and correspnding to the MQST regime. Violet triangles correspond to an intermediate regime with mixed oscillations and self-trapping or unclassifiable dynamics. The black dashed line indicates the theoretical critical value of Z_c, demarcating the boundary between these two distinct regimes.

In Figure 3.10 we summarise our findings regarding the analysis of the small oscillations to MQST transitions. We compare the eGPE dynamics results with the theoretical model for different values of the interaction ϵ_{dd} and initial quench of the population imbalance Z_0. Every triangle corresponds to a eGPE dynamics, downward-pointing blue for small oscillations regime and upward-pointing red for the MQST. Purple triangles correspond to a transient regime where, for example, the clusters start in the MQST regime but after a finite amount of time both Z and $\Delta\theta$ start oscillating, as in the small oscillations regime. The precise classification of these intermediate dynamics were not the purpose of this work. For values of the interaction $\epsilon_{dd} > 1.46$, the dynamics stops to show the single Josephson mode due to the loss of coherence between the clusters, thus marking the transition from supersolid regime to indipendent droplets crystal. The black dashed line corresponds

to the theoretical critical value

$$Z_c = \sqrt{\frac{16K}{UN_{23}}} \tag{3.57}$$

as a function of ϵ_{dd}. This line splits the phase diagram in two areas: light blue for the small oscillations regime, while orange for the MQST. Overall, eGPE shows a dynamics in the MQST regime for values of ϵ_{dd} and Z_0 according to the theoretical predictions (red triangles are in the orange area).

3.5 Discussion

The parameters of the system, such as the number of atoms N and the frequencies of the harmonic trapping potential, play a crucial role in determining the behaviour and properties of the system. To observe the phenomenon of supersolidity, it is necessary to induce rotonic instability through confinement along the direction of dipole polarisation $\hat{z}$, as well as weaker confinement along the direction $\hat{x}$ in which density modulation will develop. Therefore, it is possible to use different harmonic frequencies ω_x, leading to the formation of supersolid with a different number of clusters, which implies a different value of M in the theoretical model. The simpler case of $M = 1$, or a 2-mode model, could not be reproduced even though a ground state with tighter confinement was observed, resulting in only two clusters. However, when dynamics is introduced, these two clusters tend to shift and decrease, resulting in the formation of smaller clusters at the boundaries of the trap that oscillate, appear and disappear. Many modes are thus excited, making it impossible to isolate the single Josephson dynamics. We switched to the scenario of $M = 2$, which corresponds to a 4-mode model, and this stable configuration was successfully reproduced through our numerical simulations. The presence of the lateral clusters seems essential to excite the single Josephson mode in the system. Moreover, exciting the 4 clusters system with a single gaussian potential under one of the two central clusters instead of the sinusoidal potential under all clusters, starts a dynamics with many modes coupled. The dynamics of the central clusters seems to be stabilized through the dynamics of the lateral clusters, that is the essence of the hypothesis Eq. (3.21) at the basis of our theoretical model. With the decrease of ω_x, thus the increase of the number of clusters, the system is still stable and is possible to observe Josephson dynamics ([19]).

This chapter demonstrates that the dynamics of the system, initially prepared with a small population imbalance between supersolid clusters, exhibits a sinusoidal oscillation of the population imbalance across the density dip. This oscillation frequency decreases as the system crosses the supersolid phase towards the indipendent droplets regime. Furthermore, by increasing the initial population imbalance between clusters, the system enters the non-linear regime of MQST, characterized by non-symmetric population oscillations and running phase difference, analogue to standard BJJs.

It is noteworthy that these characteristic features of the Josephson effect are observed in the absence of an external weak link, as the weak links in supersolids are self-induced by internal interactions. The Josephson frequencies obtained from the numerical data were compared with the theoretical predictions, yielding good agreement. Overall, we provided evidence for the existence of both Josephson oscillations and MQST in supersolid dipolar quantum gases, contributing to our understanding of the phase rigidity of these systems. This novel kind of JJ, which is self-induced, can open the path toward the exploration of fundamental physics of this new state of matter.

4

Sub-unity superfluid fraction of a supersolid from self-induced Josephson effect

The following chapter stems from a fruitful collaboration between the experimental group led by G. Modugno at CNR in Pisa and the theoretical group QSTAR (Quantum Science and Technology in ARcetri) in which I spent my PhD. This resulted in an article of a great impact sent for publication and now under review in the journal Nature [19] and from which this chapter is inspired. The authors of this article which I had the pleasure to work with are Giulio Biagioni, Nicolò Antolini, Luca Pezzè, Augusto Smerzi, Marco Fattori, Andrea Fioretti, Carlo Gabbanini, Massimo Inguscio, Luca Tanzi and Giovanni Modugno.

This chapter starts with a broader perspective on supersolidity, looking for a universal measure capable of detecting and quantifying the supersolid state of a system. This measure is known as the superfluid fraction, which has been extensively investigated by Leggett [15, 120]. In this chapter, we will propose an alternative expression related to the coupling energy of a JJ. Experimental observation of the Josephson effect not only confirms its presence in a novel, self-induced JJ (see Chapter 3), but also measures the superfluid fraction and demonstrates its sub-unity value, thereby revealing the supersolid nature of the system.

4.1 Quantifying supersolidity

Supersolids are a fundamental phase of matter originated by the spontaneous breaking of the gauge symmetry as in superfluids and superconductors, and of the translational symmetry as in crystals [14, 15, 121, 122]. This gives rise to a macroscopic wavefunction with spatially-periodic modulation, and to mixed superfluid and crystalline properties. Supersolids were originally predicted in the context of solid helium [14, 15, 121, 122]. Today, quantum phases with spontaneous modulation of the wavefunction are under study in a variety of bosonic and fermionic systems such as: the second layer of 4He on graphite [123, 124]; ultracold quantum gases in optical cavities [125], with spin-orbit coupling [126], or with strong dipolar interactions [16–18, 127]; the pair density wave phase of 3He under confinement [128, 129]; pair density wave phases in various types of superconductors [130–132]. Related phases have been proposed to exist in the crust of neutron stars [133] and for excitons in semiconductor heterostructures [134]. All these systems might be connected to supersolidity, which however so far has emerged clearly only in some cold-atom systems with the evidence of the double spontaneous breaking and of the mixed superfluid-crystalline character [93, 94, 125]. The experiments carried out so far on the other types of systems have proved the coexistence of superfluidity/superconductivity and crystal-like structure [123, 124, 128–132], but no quantitative connection of the observations to the concept of supersolidity has been made. One of the difficulties in comparing different types of systems with spatial modulation of the wavefunction is the seeming lack of a universal property quantifying the deviations from the dynamical behavior of ordinary superfluids or superconductors.

Here we note that a property with such characteristics already exists, the so-called superfluid fraction of supersolids, well known in the field of superfluids but not in the one of superconductors. The superfluid fraction, introduced by A. J. Leggett in 1970 [15], quantifies the effect of the spatial modulation on the superfluid stiffness, which is in itself a defining property of superfluids and superconductors. The superfluid stiffness indeed measures the finite energy cost of twisting the phase of the macroscopic wavefunction and accounts for all fundamental phenomena of superfluidity, such as phase coherence, quantized vortices and supercurrents [13]. As shown in Figure 4.1, while in a homogeneous superfluid/superconductor the phase varies linearly in space, in a modulated system most of the phase variation can be accommodated in the minima of the density, reducing the energy cost. Since the

superfluid velocity is the gradient of the phase, this implies that peaks and valleys should move differently, giving rise to complex dynamics with mixed classical (crystalline) and quantum (superfluid) character. For example, fundamental superfluid phenomena like vortices and supercurrents are predicted to be profoundly affected by the presence of the spatial modulation, losing the canonical quantization of their angular momentum [15, 135–137]. The superfluid fraction, which ranges from unity for standard superfluids to zero for standard crystals, enters directly in all these phenomena and is therefore the proper quantity to assess the deviations from standard superfluids and superconductors. Note that the superfluid fraction of supersolids is not related to thermal effects, in contrast to the superfluid fraction due to the thermal depletion of superfluids and superconductors [138].

The standard methods to measure the superfluid stiffness are based on the measurement of global properties such as the moment of inertia for rotating superfluids [123, 124], or the penetration depth of the magnetic field for superconductors [139]. In dipolar supersolids, previous attempts using rotational techniques revealed a large superfluid fraction [95], but were not precise enough to assess its sub-unity value [96, 97]. In the other systems there is evidence that the superfluid stiffness is low [123, 124, 139], but no quantitative measurement of a sub-unity superfluid fraction is available.

In this work we make a paradigm shift, demonstrating that it is possible to measure ,the superfluid fraction not only from global dynamics but also from a fundamental phenomenon taking place in individual cells of a supersolid: the Josephson effect [20]. Here we demonstrate that a supersolid can in fact sustain coherent phase-density oscillations, behaving as an array of Josephson junctions. We also show that the Josephson coupling energy that one can deduce from the Josephson oscillations provides a direct measurement of the local superfluid fraction. We use this novel approach to measure with high precision the superfluid fraction of the dipolar supersolid appearing in a quantum gas of magnetic atoms. We find a whole range of sub-unity values of the superfluid fraction, depending on the depth of the density modulation in accordance with Leggett's predictions.

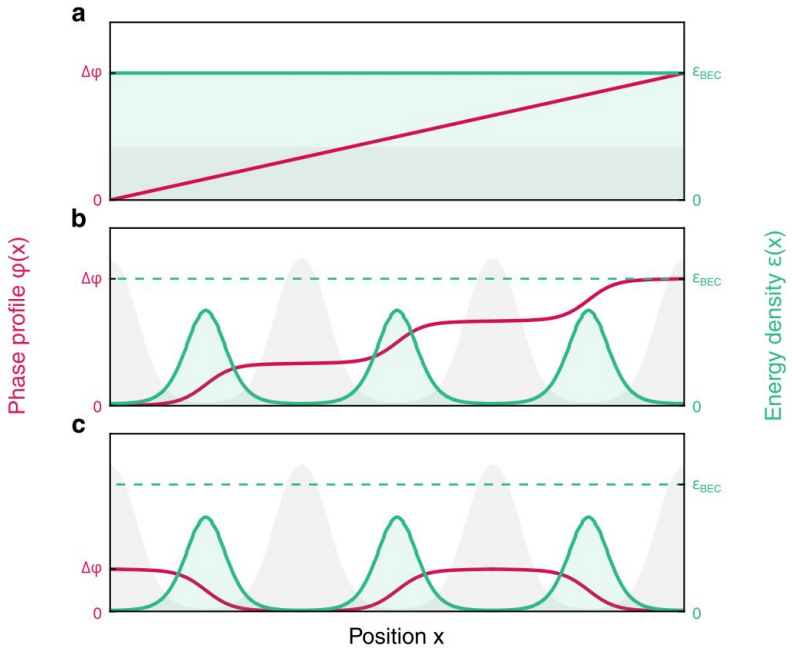

Figure 4.1: Sketch of the superfluid fraction from the application of a phase twist in a bosonic system at zero temperature. a) In a homogeneous superfluid a phase twist with amplitude $\Delta\phi$ results in a constant gradient of the phase, i.e. a constant velocity, while in a supersolid (b,c) the kinetic energy can be minimised by accumulating most of the phase variation in the low-density regions. The grey and green areas represent the number density and the kinetic energy density respectively, while the phase profile is plotted in red. The superfluid fraction is the ratio of the area under the green curve to that of the homogeneous case. (b) Leggett's approach, which for an annular system would correspond to a stationary rotation, leads to a monotonous increase of the phase. (c) Our method, based on an alternating oscillation of the phase, leads to Josephson oscillations. Both kinetic energy and superfluid fraction are the same for b) and c).

4.2 Superfluid fraction

Leggett's approach to the superfluid fraction considers an annular supersolid in the rotating frame and maps it to a linear system with an overall phase twist, as sketched in Figure 4.1b. The superfluid fraction is defined on a unit cell as [15, 140]

$$f_s = \frac{E_{kin}}{E_{kin}^{hom}} \ . \tag{4.1}$$

The numerator is the kinetic energy acquired by the supersolid with number density $n(x)$ when applying a phase twist over a lattice cell of length d

$$E_{kin} = \frac{\hbar^2}{2m} \int_{cell} dx n(x) |\nabla \phi(x)|^2 \tag{4.2}$$

and thus accounts for density and phase modulations. The denominator

$$E_{kin}^{hom} = \frac{1}{2} N m v_s^2 \tag{4.3}$$

is the kinetic energy of a homogeneous superfluid of N atoms and velocity $v_s = \hbar \Delta\phi/(md)$ associated with a constant phase gradient across the cell. Using a variational approach [15, 120], Leggett found an upper (f_s^u) and a lower (f_s^l) bound for the superfluid fraction Eq. (4.1) [120]

$$f_s^u \equiv \iint \frac{dz\, dy}{\frac{1}{d^2}\int_{\text{cell}} \frac{dx}{n(x,y,z)}} \leq f_s \leq \left(\frac{1}{d^2} \int_{\text{cell}} \frac{dx}{\iint dy\, dz\, n(x,y,z)} \right)^{-1} \equiv f_s^l \tag{4.4}$$

where x is the direction where the supersolid modulation extends and the 1D density $\bar{n}(x) \equiv \iint dy\, dz\, n(x,y,z) / \iint dy\, dz \int_{cell} dx\, n(x,y,z)$ is normalized over the cell. This normalization in the upper bound restricts f_s to be lower than unity if the density is spatially modulated.

We propose an alternative expression for the superfluid fraction, considering Josephson phase twists with alternating sign between neighbouring lattice sites of a supersolid, as sketched in Figure 4.1. This corresponds to a different type of motion of the supersolid, with no global flow but with alternate Josephson phase-density oscillations between sites. Also in this case we can consider a single cell, since the kinetic energy is proportional to $|\nabla\phi|^2$, so it does not depend on the sign of the phase twist. In the limit of small excitations ($\Delta\phi \to 0$), the kinetic energy of a Josephson junction is given by $E_{kin} = NK\Delta\phi^2$, where K is the coupling energy across the barrier [27]. From Eq. (4.1) we thus find

$$f_s = \frac{K}{\hbar^2/(2md^2)} \tag{4.5}$$

showing a direct relation between the superfluid fraction and the coupling energy of the junction. We note that an expression similar to the upper bound in Eq. (4.4) was derived by Leggett for the coupling energy of a single Josephson junction [105], however without discussing the connection to the superfluid fraction.

4.3 Observation and modelling of josephson oscillations in a dipolar supersolid

We now demonstrate the existence of coherent Josephson-like oscillations in a dipolar supersolid [16]. This system is particularly appealing to study fundamental aspects of supersolidity: the supersolid lattice is macroscopic, with many atoms per site and large superfluid effects; the available control of the quantum phase transition allows to directly compare supersolids and superfluids; interactions are weak, allowing accurate theoretical modelling. The experimental system that we have numerically simulated is composed of $N = 3 * 10^4$ bosonic dysprosium atoms, held in an harmonic trap elongated along the x direction, with trap frequencies $\omega_{x,y,z} = 2\pi(18{,}97{,}102)$Hz. By tuning the relative strength ϵ_{dd} of dipolar and contact interactions, we can cross the quantum phase transition from a standard BEC to the supersolid regime. This can be performed experimentally by tuning the contact scattering length a_s by means of a magnetic Feshbach resonance (see Chapter 3). The supersolid density modulation is one dimensional, leading to a continuous phase transition [111]. Differently from Chapter 3, our supersolid is made of two main central clusters and four smaller lateral ones, thus six clusters ($M = 3$) with a lattice period $d \cong 4\mu m$, as shown in Figure 4.2a. We can vary the density modulation depth by varying the interaction strength in the range $\epsilon_{dd} = 1.38 - 1.45$. The further increase of ϵ_{dd} leads to the formation of an incoherent crystal of separate clusters, the so-called droplet crystal, a regime that can only be observed numerically, but cannot be studied experimentally due to its short lifetime [16].

We experimentally and numerically observe that the application for a short time of an optical lattice with twice the spacing of the supersolid (sketched in Figure 4.2a) imprints the proper alternating phase difference between adjacent clusters to excite Josephson oscillations between them. After a variable evolution time without the lattice, we measure both the evolving phase difference $\Delta\theta$ between neighbouring clusters and the population imbalance Z between the left and right halves of the supersolid. $\Delta\theta$ is measured experimentally from the interference fringes developing after a free expansion (snapshots in Figure 4.2b, top row), while Z is measured by in-situ phase-contrast imaging (Figure 4.2b, bottom row). As shown in Figure 4.2, there is a single-frequency oscillations of Z and $\Delta\theta$, with the characteristic $\pi/2$ phase shift of the standard Josephson dynamics [20, 27, 29, 141–143]. The observation time is limited to about 100ms by the finite lifetime of the supersolid,

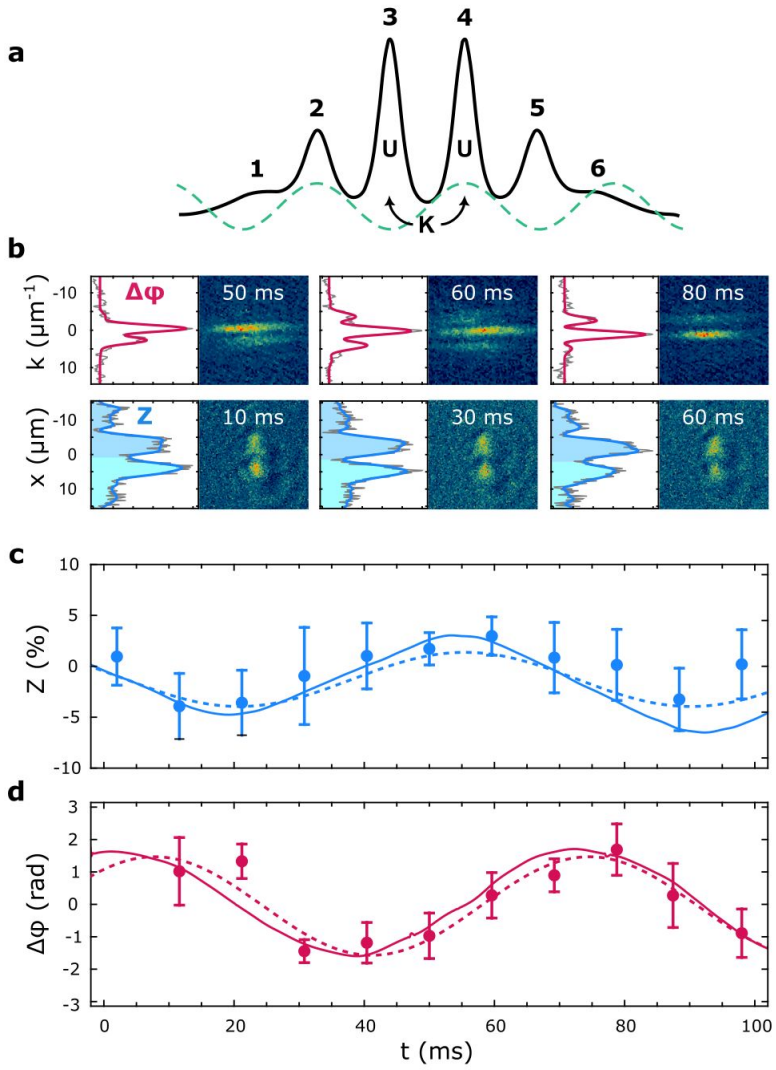

Figure 4.2: Josephson oscillations in a supersolid. (a) Sketch of the experimental system. The black line is the supersolid density profile at equilibrium. The green dashed line is the optical lattice potential used for the phase imprinting. (b) Examples of experimental single shots and corresponding integrated 1D profiles. Top row: interference fringes after a free expansion. Red curves are fit functions used to extract the phase difference $\Delta\theta$. Bottom row: in-situ images. Shaded areas indicate the populations of the left and right halves of the supersolid used to extract the population imbalance Z. (c) Oscillations of Z as a function of time at $\epsilon_{dd} = 1.428$. Dots are experimental points. The solid line is the numerical simulation for the same parameters. The dotted line is a sinusoidal fit to the experimental data. (d) Same for $\Delta\theta$.

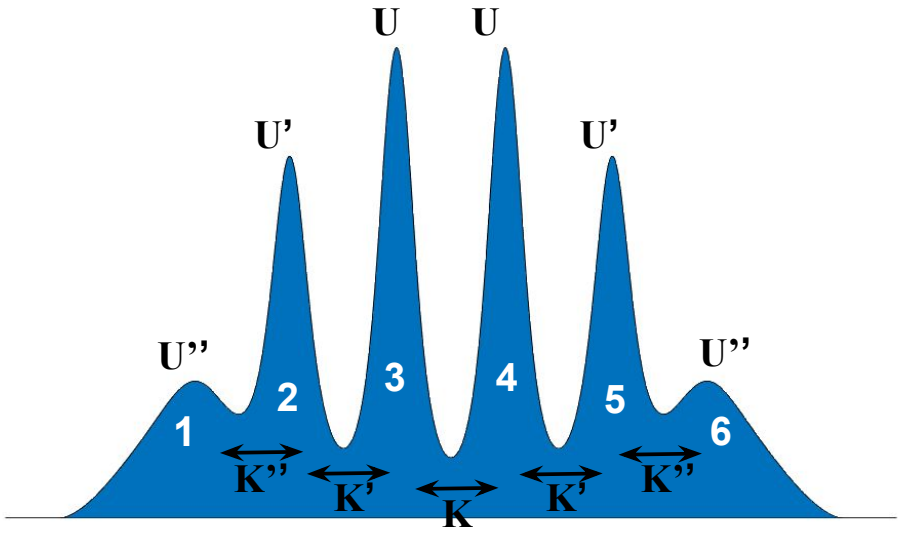

Figure 4.3: Integrated profile of supersolid at $\epsilon_{dd} = 1.43$ from eGPE. The indices of the six clusters goes from left to right. Clusters $3-4$ have an interacting parameter U, clusters $2-5$ have U' and clusters $1-6$ have U''. The coupling coefficients are K for the central one between 2 and 3, K' for the ones between $2-3$ and $4-5$ and K'' for the ones between $1-2$ and $5-6$. Lateral clusters are smaller and smaller due to the energy offsets given by the harmonic trapping.

due to unavoidable particle losses [16]. The experimental observations agree very well with numerical simulations based on the time-dependent eGPE, also shown in Figure 4.2c-d (see section 3.3).

The observation of a single frequency in both experiment and numerical simulations indicates not only that it is possible to excite Josephson-like oscillations in a supersolid, but also that they are a normal mode of the system (see Chapter 3). To model our observations, we develop a six-mode model, thus $M = 3$ in the theoretical model of subsection 3.2.4.

In Figure 4.3 is shown an integrated density profile of the six-clusters supersolid with the relative interaction parameters U_j, with $j = 1, ...,6$ labelling the clusters, five coupling parameters between adjacent clusters $K_{j,j+1}$, and energy offsets E_0 and E_1, for the opposite side clusters 1 and 6, and 2 and 5, due to the harmonic trap. We indicate as $K = K_{34}$ and $U = U_3 = U_4$ the coupling and interaction energy, respectively, in two central clusters. The symmetry of the system further allows us to equalise the two side coupling $K' = K_{23} = K_{45}$ and $K'' = K_{12} = K_{56}$, the two side interactions $U' = U_2 = U_5$ and $U'' = U_1 = U_6$ (see Figure 4.3). We thus have a system of six equations for the time evolution of the populations N_j

and five phase differences $\Delta\theta_{ij} = \theta_i - \theta_j$

$$\begin{aligned}
\dot{N}_1 &= -2K'2\sqrt{N_1N_2}\sin\Delta\theta_{21} \\
\dot{N}_2 &= 2K''\sqrt{N_1N_2}\sin\Delta\theta_{21} - 2K'\sqrt{N_2N_3}\sin\Delta\theta_{32} \\
\dot{N}_3 &= 2K'\sqrt{N_2N_3}\sin\Delta\theta_{32} - 2K\sqrt{N_3N_4}\sin\Delta\theta_{43} \\
\dot{N}_4 &= 2K\sqrt{N_3N_4}\sin\Delta\theta_{43} - 2K'\sqrt{N_4N_5}\sin\Delta\theta_{54} \\
\dot{N}_5 &= 2K'\sqrt{N_4N_5}\sin\Delta\theta_{54} - 2K''\sqrt{N_5N_6}\sin\Delta\theta_{65} \\
\dot{N}_6 &= 2K''\sqrt{N_5N_6}\sin\Delta\theta_{65} \\
\Delta\dot{\theta}_{21} &= E^1 + U''N_1 - U'N_2 \\
\Delta\dot{\theta}_{32} &= E^0 + U'N_2 - UN_3 \\
\Delta\dot{\theta}_{43} &= U(N_3 - N_4) \\
\Delta\dot{\theta}_{54} &= -E^0 + UN_4 - U'N_5 \\
\Delta\dot{\theta}_{65} &= -E^1 + U'N_5 - U''N_6
\end{aligned} \tag{4.6}$$

where we considered the case $(N_4 + N_3)U/(2K) >> 1$ so that we can neglect the coupling terms in the evolution of the phases. Following the procedure of Chapter 3, we find a Josephson dynamics between central clusters under the hypothesis Eq. (3.21) with $M = 3$

$$\dot{N}_4 - \dot{N}_4 = \alpha(\dot{N}_1 + \dot{N}_2 - \dot{N}_5 - \dot{N}_6) \tag{4.7}$$

so that Eq. (4.6) becomes

$$\begin{aligned}
\dot{N}_4 - \dot{N}_3 &= 4K\frac{\alpha}{\alpha - 1}\sqrt{N_3N_4}\sin(\Delta\theta_{43}) \\
\Delta\dot{\theta}_{43} &= -U(N_4 - N_3)
\end{aligned} \tag{4.8}$$

These equations hold in the parameter regime given by

$$\begin{aligned}
\frac{U''}{U'} &= 1 + \frac{K'}{K''}\sqrt{\frac{N_3^0}{N_1^0}} \\
\frac{U'}{U} &= \frac{1 + \frac{K}{K'}\sqrt{\frac{N_3^0}{N_2^0}}}{1 + \frac{K''}{K'}\sqrt{\frac{N_1^0}{N_3^0}}}
\end{aligned} \tag{4.9}$$

where α assumes the form

$$\alpha = \left(\frac{U}{U'} - \frac{U}{U''}\right)^{-1} \tag{4.10}$$

The parameters U and K of the central clusters are extracted from Eq. (4.8). The other parameters U', U'', K' and K'' are extracted from fits using Eq. (4.6). Overall, we obtain that the interactions parameters are $U/U' \sim 1$, $U/U'' \sim 1/2$ within fluctuations of about 10% for different values of ϵ_{dd}. On the other hand, the coupling ratio $K/K' \sim 0.6$ is constant, while $K/K'' \sim 0.7$ on the BEC side and decreases with ϵ_{dd}, as do the initial external populations $N1(0) = N6(0)$. We thus find that Eq. (4.10) is fulfilled and $\alpha = 2$.

Defining $\Delta N \equiv N_2 - N_3$ and using $\alpha = 2$, the system Eq. (4.8) becomes

$$\begin{aligned} \dot{\Delta N} &= 4KN_{34}\sin(\Delta\theta) \\ \dot{\Delta\theta} &= -U\Delta N \end{aligned} \tag{4.11}$$

where $N_{34} \equiv N_3 + N_4$ and $\Delta\theta \equiv \Delta\theta_{43}$.

Eq. (4.11) are equivalent to those of a simple pendulum with angle $\Delta\theta$ and angular momentum ΔN, and in the small-angle limit feature sinusoidal oscillations with a single frequency

$$\omega_J = \sqrt{4KUN_{34}} \tag{4.12}$$

We emphasise that the current-phase relation Eq. (4.11) as well as ω_J^2 differ by a factor 2 with respect to the Josephson equations of two weakly coupled BECs, due to the contribution of the lateral clusters. Notice also that Eq. (4.11) depend only on the coupling energy K and the interaction energy U of the two central clusters, in contrast to the expectation that the inhomogeneity of the trapped system may introduce other energies in the equations of motion. We checked by Gross-Pitaevskii simulations that the experimental configuration satisfies the conditions Eq. (4.9) to have a Josephson-like normal mode.

In the experiment it was not possible to resolve the populations of the individual clusters, but we studyied the population difference between the left and right halves of the system, $Z = (N_1 + N_2 + N_3 - N_4 - N_5 - N_6)/N$. There is a proportionality relation between the two observables, $\Delta N = 2NZ$, which allows us to rewrite Eq. (4.11) in terms of the experimental observables.

An important difference between a cell of the supersolid and a standard Josephson junction is the fact that in the supersolid the position of the weak link is not fixed by an external barrier but it is self-induced, so it can move. This leads to the appearance of a low-energy Goldstone mode associated with the spontaneous translational symmetry breaking. In a harmonic potential, it consists of a slow oscillation of the position of the weak link, together with the density maxima, and

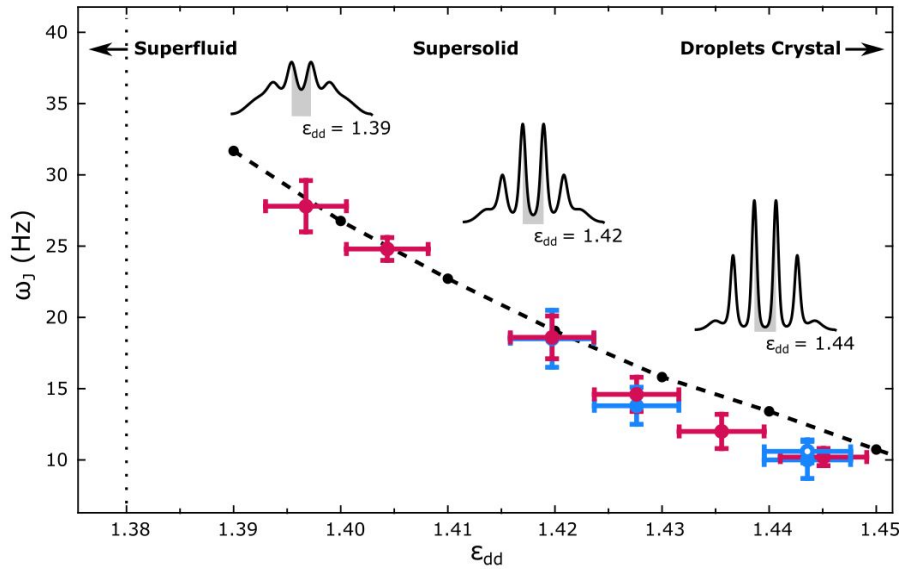

Figure 4.4: Josephson oscillation frequencies as a function of the interaction parameter ϵ_{dd}. Red dots are the experimental frequencies for $\Delta\theta$. Filled and open blue dots are the frequencies for Z measured by in situ imaging with and without optical separation, respectively [19]. The red point at $\epsilon_{dd} = 1.444$ is slightly shifted horizontally for clarity. Black points are the results of numerical simulations and dashed line is a guide for the eye. The insets show the modulated ground state density profiles obtained from numerical simulations for different values of ϵ_{dd}. The vertical dotted line marks the critical point of the superfluid-supersolid quantum phase transition.

an associated oscillation of both Z and $\Delta\theta$ [27]. Due to its low frequency (few Hz), the Goldstone mode is spontaneously excited by thermal fluctuations, resulting in shot-to-shot fluctuations of the experimental observables. The same low frequency, however, allows to separate Josephson and Goldstone dynamics in both experiment and theory. We measure the Josephson frequency ω_J from a sinusoidal fit of the phase and population dynamics in Figure 4.2c-d. We repeat the measurement by varying the interaction parameter ϵ_{dd}, corresponding to different depths of the supersolid density modulation. Figure 4.4 shows the fitted frequencies as a function of ϵ_{dd} comparing experimental data with numerical simulations. We observe a decrease of the frequency for increasing ϵ_{dd}. This is justified by the fact that the superfluid current across the junction decreases because a larger and larger portion of the wavefunction remains localised inside the clusters, see insets in Figure 4.4. This reduces the coupling energy K while only weakly affecting the interaction energy.

From the Josephson frequency Eq. (4.12) we can derive the coupling energy

$$K = \frac{\omega_J^2}{4UN_{34}} \tag{4.13}$$

using the experimental measured frequency and the numerical value of denominator. We verified that this relation holds not only in the small-amplitude regime of the simulations, but also for the larger amplitudes of the experiment.

From the measured K, we derive in turn the superfluid fraction using Eq. (4.5). The results are shown in Figure 4.5 and feature a progressive reduction of the superfluid fraction below unity for increasing depths of the supersolid modulation. The experimental data are in good agreement with the numerical simulations (green dots). According to Eq. (4.11), the coupling energy is obtained from the linear dependence of dZ/dt on $\sin(\Delta\theta)$ (current-phase relation) both with numerical and experimental data, see Figure 4.5b-c.

What we measure here is the superfluid fraction of the central cell of our inhomogeneous supersolid, for a one-dimensional phase twist. Such a local quantity would coincide with the global superfluid fraction of a hypothetical homogeneous supersolid, composed of cells identical to our central one. This includes the annular geometry originally studied by Leggett, where however our supersolid with macroscopic clusters would also show transverse effects, not included in Leggett's theory for the moment of inertia [15]. Studying the Josephson effect allows us to avoid such transverse effects.

In Figure 4.5a we also compare our results with Leggett's prediction of Eq. (4.4), relating the superfluid fraction to the density modulation of the supersolid. From the numerical density profiles, we calculate both the upper bound f_s^u and the corresponding lower bound [120] f_s^l, which delimit the grey area in Figure 4.5a. The two bounds would coincide if the density distribution were separable in the transverse coordinates y and z. Since our supersolid lattice is one dimensional, the two bounds are close to each other. The superfluid fraction calculated from the simulated dynamics lies between the two bounds in the whole supersolid region we investigated, demonstrating the applicability of Leggett's result to our system.

In conclusion, the overall agreement between experiment, simulations and theory on our dipolar supersolid proves the long-sought sub-unity superfluid fraction of supersolids and its relation to the spatial modulation of the superfluid density. The demonstration of self-sustained Josephson oscillations in a supersolid not only establishes an analogy between supersolids and Josephson junction arrays, but also

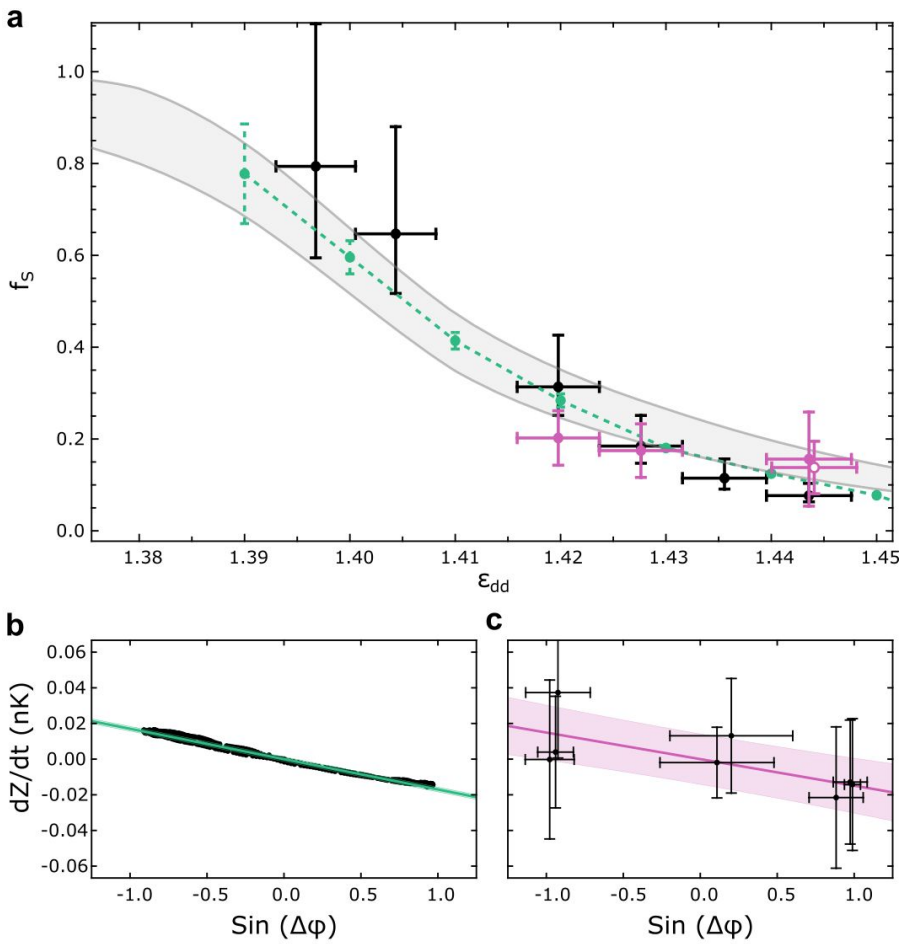

Figure 4.5: Superfluid fraction of the supersolid from Josephson oscillations. (a) Superfluid fraction as a function of ϵ_{dd}. Black dots are experimental results derived from the Josephson frequencies. Green dots are results from numerical simulations. Pink points are derived from the experimental phase-current relation, as in (c). The open pink point at $\epsilon_{dd} = 1.444$ is the dataset without the optical separation technique (Methods). The grey band spans from the upper to the lower bound of Eq. (4.4). (b-c) Current-phase relation at $\epsilon_{dd} = 1.444$. The points show the results of numerical simulations (b) and experimental measurements (c), respectively. From the linear regressions (green and pink lines) we extract the coupling energy K according to Eq. (4.13). The shaded regions are the confidence bands for one standard deviation.

provides a novel proof of the extraordinary nature of supersolids compared to ordinary superfluids and crystals. These oscillations indeed cannot exist neither in crystals, where particles are bound to lattice sites, nor in ordinary superfluids, which do not have a lattice structure.

4.4 Discussion

Our findings open new research directions. The observed reduction of the superfluid fraction with increasing modulation depths may explain the low superfluid stiffness measured in other systems, such as ^{4}He on graphite [123, 124] or superconductors hosting pair-density-wave phases [130–132]. An important question related to the pair density waves in fermionic systems is how Leggett's bounds on the superfluid fraction may be extended to systems where the superfluid density and particle density do not coincide. Note that Eq. (4.4) is also applicable to standard superfluids with an externally-imposed spatial modulation, as demonstrated for BECs in optical lattices via measurements of the effective mass [141] or of the sound velocity [144, 145]. In the supersolid, however, the dynamics linked to the reduced superfluid fraction is not constrained by an external potential, and so totally new phenomena might be observed. The large value of f_s we measured for the dipolar supersolid, which remains larger than 10% also for deep density modulations, indicates that partially quantized supercurrents [15, 136] and vortices [135] should appear at a macroscopic level.

Due to the generality of the Josephson effect, our Josephson-oscillation technique might be applied to characterise the local superfluid dynamics of the other supersolid-like phases under study in superfluid and superconducting systems. The Eq. (4.5) is applicable in general, considering that the detection of Josephson oscillations implies measurement of both the coupling energy and the spatial period of the superfluid density modulation. For example, a promising type of system may be the pair-density wave phase in superconductors, where the modulation has already been resolved.

Additionally, the self-induced Josephson junctions we have identified in supersolids might have extraordinary properties due to the mobility of the weak links. Indeed, although the Goldstone mode of the weak links is not relevant for the Josephson dynamics due to its very low energy, for the same reason it may affect the fluctuation properties of the junction [146], potentially leading to new thermometry methods [147], and especially to novel entanglement properties [148].

5

Stabilizing persistent currents in an atomtronic Josephson junction necklace

This chapter stems from a different fruitful collaboration with the experimental group of G. Roati at LENS (European Laboratory for Non-Linear Spectroscopy) in Florence. This resulted in an article sent for publication in the journal Nature Communication [34] and now under review and from which this chapter is freely inspired. The authors of this article with which I had the pleasure to work are Luca Pezzè, Klejdja Xhani and the experimental group composed by Cyprien Daix, Nicola Grani, Francesco Scazza, Diego Hernandez-Rajkov, Woo Jin Kwon, Giulia Del Pace and Giacomo Roati.

In this chapter we want to study arrays of Josephson junctions, that are at the forefront of research on quantum circuitry for quantum computing, simulation and metrology. They provide a testing bed for exploring a variety of fundamental physical effects where macroscopic phase coherence, nonlinearities and dissipative mechanisms compete. Here we realize finite-circulation states in an atomtronic Josephson junction necklace, consisting of a tunable array of tunneling links in a ring-shaped superfluid. We study the stability diagram of the atomic flow by tuning both the circulation and the number of junctions. We predict theoretically and demonstrate

experimentally that the atomic circuit withstands higher circulations (corresponding to higher critical currents) by increasing the number of Josephson links. The increased stability contrasts with the trend of the superfluid fraction – quantified by Leggett's criterion – which instead decreases with the number of junctions and the corresponding density depletion. Our results demonstrate atomic superfluids in mesoscopic structured ring potentials as excellent candidates for atomtronics applications, with prospects towards the observation of non-trivial macroscopic superpositions of current states.

5.1 Josephson junction necklace

Josephson junction arrays are pivotal and versatile elements that hold promise to turn quantum mechanics into emerging computing, sensing and simulation technologies [149–153]. By harnessing the dissipationless non-linearity of single Josephson junctions, combined with strong collective effects, they show intriguing synchronization [154–157] and interference [141, 158, 159] phenomena. Furthermore, they serve as experimental tools to investigate the phase coherence and order parameters in high-T_c superconductors [160, 161].

An array of junctions in a multiply-connected geometry forms a Josephson junction necklace (JJN). In this configuration, the Josephson effect is used to control the current of persistent states, implementing robust dynamical regimes characterized by the competition between tunneling and interaction energies [21]. JJNs with one or two junctions realize common quantum interference devices (SQUIDs) [162, 163], which find applications in rotation sensing with superfluid gyroscopes [164, 165] and magnetic field sensing with superconducting rings [162, 166]. Furthermore, JJNs are key elements of atomtronic circuits [167–170]. Ultracold atoms in toroidal traps with a single junction or a weak link have been explored for the experimental realization of ultra-stable circulation states [171–174], including the study of various superfluid decay phenomena [175–177], current-phase relations [178] and hysteresis [179]. These experiments have stimulated several theoretical studies that have mainly focused on the analysis of different instability phenomena in ring superfluids with various types of defects and potentials [180–187]. In addition, double-junction atomtronic SQUIDs have enabled the observation of different regimes of Josephson dynamics [188], resistive flow [189] and quantum interference of currents [190].

Interestingly, as conjectured by Feynman [191], further intriguing quantum coherence effects can arise – due to the stiffness of the superfluid phase – in ring systems hosting arrays of multiple junctions. However, despite advancements both in manufacturing mesoscopic nanostructured multi-linkcircuits [192–196] and in engineering atomic trapping potentials [169, 197–199], the realization of tunable JJNs with arbitrary number of junctions remains technologically and experimentally challenging, and so far elusive in both superconducting and superfluid platforms.

In this work, we investigate supercurrent states in an atomtronic JJN. We analytically predict the stabilization of persistent currents against decay by increasing the number of junctions, n. We support this surprising prediction by numerical simulations and we demonstrate it experimentally in a bosonic superfluid ring with n up to 16. Such an effect is a direct consequence of the single-valuedness of the order parameter, reflecting the macroscopic phase coherence of the superfluid state. Increasing the number of Josephson links leads to a decrease of the superfluid speed across each junction and to the corresponding increase of the global maximum (critical) current in the ring. Furthermore, the density depletion associated to an increasing n determines a decrease of the superfluid fraction according to Leggett's formulation [15, 120] that, however, does not result in a decrease of the critical current. The full control of our atomtronic circuit opens exciting prospects toward the realization of non-trivial quantum superpositions of persistent currents [200–204].

5.2 Critical current in a multi-junction Josephson necklace

A steady superfluid state can be described by a collective wavefunction $\psi(\boldsymbol{r}) = \sqrt{\rho(\boldsymbol{r})}e^{i\phi(\boldsymbol{r})}$, with $\rho(\boldsymbol{r})$ and $\phi(\boldsymbol{r})$ being the density and the phase of the superfluid, respectively [13]. The latter is related to the superfluid speed by $\boldsymbol{v}(\boldsymbol{r}) = \frac{\hbar}{m}\nabla\phi(\boldsymbol{r})$, where m is the atomic mass and $\hbar$ the reduced Planck constant. To ensure a single-valued wavefunction, the integral of $\nabla\phi(\boldsymbol{r})$ calculated around any arbitrary closed path Γ must be a multiple of 2π,

$$\frac{m}{\hbar}\oint_{\Gamma} d\boldsymbol{r}\cdot\boldsymbol{v}(\boldsymbol{r}) = 2\pi w, \tag{5.1}$$

where the integer (winding) number w is a topological invariant. In a multiply-connected geometry (e.g. in a toroidal superfluid), Eq. (5.1) defines a series of quantized persistent-current states labeled by w [205, 206]. Although the ground

state is $w = 0$, metastable finite-circulation states ($w \neq 0$) can be generated, as first demonstrated with liquid helium [207, 208] and more recently with ultracold atomic gases [171, 172, 174, 209–211].

Let us consider, for the sake of illustration, a one-dimensional (1D) JJN of radius R with n equivalent junctions modelled as narrow Gaussian potential barriers, rotating with angular velocity Ω (see Appendix G). In the rotating frame, the current of stationary states is given by

$$J = \rho(\theta)(v(\theta)/R - \Omega), \tag{5.2}$$

where θ is the azimuthal angle along the ring. Each junction induces a dip in the particle density $\rho(\theta)$, shown as the blue line in Figure 5.1(a) and (b) as calculated from the stationary state of the one-dimensional Gross-Pitaevskii equation (Appendix G). We emphasize that the barrier height is larger than the chemical potential and the barriers width is of the order of the superfluid healing length (seeAppendix G), with the density not vanishing inside the barrier. Due to

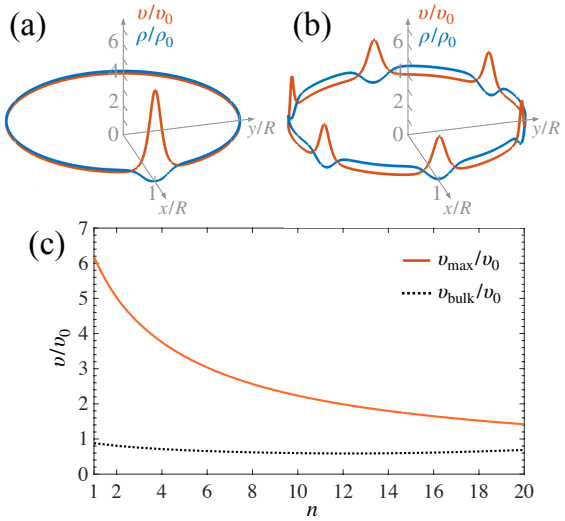

Figure 5.1: Superfluid speed in a JJN. Panels (a) and (b) show the particle density ρ (blue line) and the superfluid speed v (orange line) in a 1D ring, divided by the density (ρ_0) and speed (v_0) in the homogeneous ring, respectively. The two panels correspond to a one-dimensional JJN with $n = 1$ (a) and $n = 6$ (b) junctions, respectively. (c) Maximum, v_{max} (solid orange line), and bulk, v_{bulk} (dotted black line), superfluid speed as a function of the number of junctions. Results in all panels are obtained from the stationary state of the one-dimensional GPE with $w = 1$ and $\Omega = 0$.

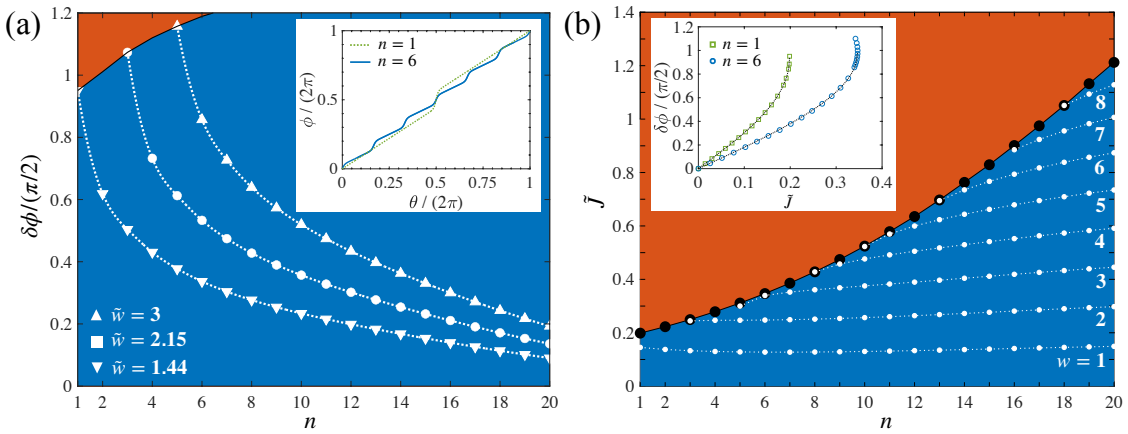

Figure 5.2: Superfluid phase and critical current in a JJN. (a) Phase gain across each junction as a function of n, Eq. (5.6), where $f(\tilde{w}, n)$ and ρ_{bulk} are obtained with GPE calculations. Symbols are obtained for $\tilde{w} = 1.44$ (downward triangles), $\tilde{w} = 2.15$ (squares) and $\tilde{w} = 3$ (upward triangles), which correspond to the maximum value of $\tilde{w}$ for $n = 1, 3$ and 5, respectively, for which a stable solution can be found. For larger values of $\tilde{w}$, for the given n, the system is unstable due to the nucleation of solitons. Lines are guides to the eye. In particular, the solid black line connects maxima of $\delta\phi$ obtained for different w, separating the stable (blue) from the unstable (orange) region. The inset shows the superfluid phase ϕ as a function of the angle θ along the ring, for $n = 1$ (dotted green line) and $n = 6$ (solid blue line). (b) Critical current as a function of the number n of junctions. The analytic formula Eq. (5.7) (large black dots) superpose to the numerical calculation of the maximum current. Small white dots show the current $\tilde{J}$ calculated for $\Omega = 0$ and different values of w, ranging from $w = 1$ (lower) to $w = 8$ (upper). Solid and dotted lines are guides to the eye. The orange region corresponds to values of the current above $\tilde{J}_c$ and are thus inaccessible in the system. Inset: phase across each junction as a function of the current (symbols) for $n = 1$ (green squares) and $n = 6$ (blue circles). The solid lines are the current-phase relations $\delta\phi = \arcsin(\tilde{J}/\tilde{J}_c) - 2\pi\ell\tilde{J}$, with $\tilde{J}_c$ and ℓ extracted from fitting.

the conservation of mass-flow (see Eq. (5.2)) a density dip implies a local increase of the superfluid speed $v(\theta)$ (orange lines in Figure 5.1(a) and (b)). Comparing the panels (a) and (b) of Figure 5.1, obtained for the same value of the circulation w and for different number of junctions, $n = 1$ and $n = 6$, respectively, we observe that the maximum superfluid speed, v_{max}, drops by increasing n. This is a consequence of the topological invariance expressed by Eq. (5.1). This is seen by writing $v(\theta) = v_{\text{bulk}} + v_{n-\text{peaks}}(\theta)$, where v_{bulk} is the bulk speed, given by the minimum velocity along the ring, and $v_{n-\text{peaks}}(\theta)$ describes the n peaks of the superfluid speed.

Replacing this expression for $v(\theta)$ into Eq. (5.1), we find

$$v_{\text{bulk}} + \frac{1}{2\pi}\int_0^{2\pi} d\theta\; v_{n-\text{peaks}}(\theta) = \frac{\hbar w}{mR}. \tag{5.3}$$

The bulk contribution in Eq. (5.3) is expected to change only slightly when adding sufficiently-narrow junctions to the JJN (see the dotted black line in Figure 5.1(c)). On the contrary, the second term in Eq. (5.3) is proportional to $nv_{\max}$. Therefore, for a given w, $v_{\max}$ must decrease roughly as $1/n$ in order to keep the integral in Eq. (5.3) constant. The decrease of $v_{\max}$ is confirmed by the results of GPE simulations reported in Figure 5.1(c) (solid orange line). The reduction of the superfluid velocity at each barrier implies a decrease of the phase gain $\delta\phi$ across each junction, upon increasing n. For a more quantitative study, we use Eq. (5.3) and notice that $v_{\text{bulk}} = JR/\rho_{\text{bulk}} + \Omega R$, where ρ_{bulk} is the bulk density, given by the maximum density along the ring, and $n\delta\phi = (mR/\hbar)\int d\theta\, v_{n-\text{peaks}}(\theta)$. We find the relation

$$\frac{2\pi\tilde{J}}{\rho_{\text{bulk}}} + n\delta\phi = 2\pi\tilde{w}, \tag{5.4}$$

where $\tilde{J} = J/J_R$, $J_R = \hbar/(mR^2)$ is the current quantum in the homogeneous (no junctions) case and $\tilde{w} = w - \Omega/J_R$ is an effective circulation in the rotating frame. Varying Ω allows to address non-integer $\tilde{w}$ and thus continuous values of the current. Furthermore, by inserting Eq. (5.2) into Eq. (5.1), we obtain

$$\tilde{J} = \frac{\tilde{w} f(\tilde{w}, n)}{2\pi}, \tag{5.5}$$

where $f(\tilde{w}, n) = (2\pi)^2\Big[\int d\theta/\rho(\theta)\Big]^{-1}$. We note that $f(\tilde{w}, n) \leq f_s$, where $f_s \in [0, 1]$ is Leggett's superfluid fraction [15, 19, 105, 120, 212, 213]. The latter expresses the phase rigidity of the system, quantified by the kinetic-energy response to a phase twist of the superfluid order parameter. Since $f(\tilde{w}, n) = f_s$ for $w = 0$ and in the limit $\Omega \to 0$ [34], Eq. (5.5) connects the superfluid fraction to the current in the ring. It is possible to see that f_s decreases with n as far as the junctions do not overlap substantially [34], therefore, according to Eq. (5.5) the current decreases as well.

On the other hand, by combining Eqs. (5.4) and (5.5), the phase across each junction reads

$$\delta\phi = \frac{2\pi\tilde{w}}{n}\left(1 - \frac{f(\tilde{w}, n)}{\rho_{\text{bulk}}}\right). \tag{5.6}$$

In Figure 5.2(a), we plot $\delta\phi$ as a function of n, Eq. (5.6), where the quantities $f(\tilde{w}, n)$ and ρ_{bulk} are obtained from the stationary states of the 1D GPE. Symbols refer to different values of $\tilde{w}$. We clearly see that $\delta\phi$ decreases with n. This implies that the condition $\delta\phi \approx \pi/2$ [11, 21] – that determines the maximum (or critical) current $\tilde{J}_c$ in the JJN – for increasing n is met for higher values of $\tilde{w}$. We find an explicit expression for $\tilde{J}_c$, by considering the usual current-phase relation $\delta\phi = \sin^{-1}(\tilde{J}/\tilde{J}_c) - 2\pi\ell\tilde{J}$ [21, 175], with ℓ an adimensional kinetic inductance. The condition $\tilde{J} = \tilde{J}_c$ provides a critical phase $\delta\phi_c = \pi/2 - 2\pi\ell\tilde{J}_c$. Replacing this value into Eq. (5.6) and using Eq. (5.5), we find

$$\tilde{J}_c = \frac{nf_c/4}{2\pi(1 - f_c/\rho_c) + nf_c\ell}, \tag{5.7}$$

where f_c and ρ_c are the values of $f(\tilde{w}, n)$ and ρ_{bulk} obtained when $\tilde{J} = \tilde{J}_c$. Neglecting the small inductance ($n\ell \ll 2\pi$), we find that the critical current is mainly determined by the competition between n and $f_c(n)$. In Figure 5.2(b) we plot the critical current obtained from the GPE solution as a function of n. Numerical values agree with Eq. (5.7) (black dots, with the solid line being a guide to the eye), where ℓ is extracted from a fit of the numerical current-phase relation, e.g. shown in the inset for $n = 1$ (green squares) and $n = 6$ (blue circles). Furthermore, small white dots in Figure 5.2(b) show the current of metastable states in the case $\Omega = 0$, where $\tilde{J}$ assumes only quantized values, see Eq. (5.5) with $\tilde{w} = w$. Figure. 5.2(b) clearly shows that $\tilde{J}_c$ increases with the number of junctions. When $\tilde{J} > \tilde{J}_c$, the current enters the unstable regime (red regions in Figure 5.2(a)-(b)), characterized by the simultaneous emission of n solitons from the barriers (see Refs. [185, 186] for a study of the case $n = 1$).

Although the above discussion is restricted to a 1D geometry, the predicted effects are expected to hold also in higher dimensions, due to the general validity of Eq. (5.1). To confirm this expectation, we have performed 3D time-dependent Gross-Pitaevskii simulations Appendix G. We prepare the ground state in an annular trap, impose a circulation w_0, and observe the dynamics of the system in the presence of n junctions. Consistently with the results of Figure 5.2, we observe a decrease with n of both the superfluid speed and the time-averaged phase gain across each junction. The results of numerical simulations are schematically summarized as in Figure 5.3(a). If the number of junctions is below a critical value n_c that depends on w_0, then vortices are emitted symmetrically from each barrier, causing phase slippage and a decay of both the current and the winding number in time.

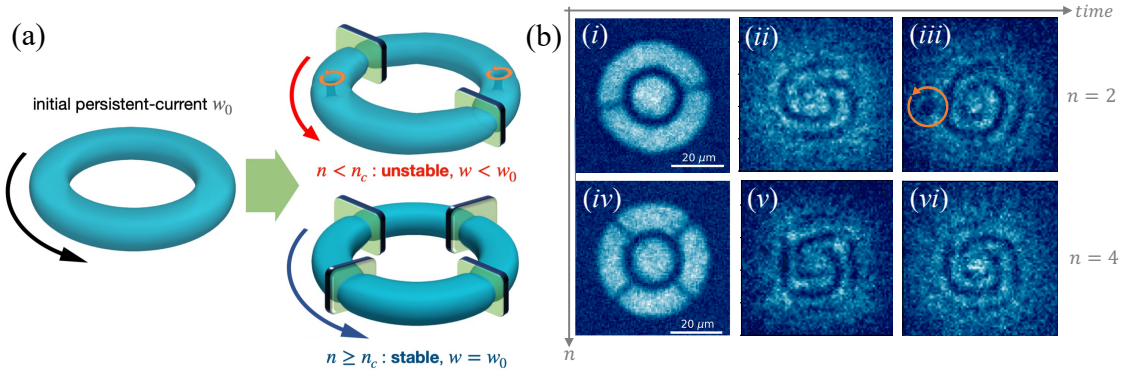

Figure 5.3: Sketch of the experiment and observables. (a) After preparing an initial persistent current state with circulation w_0, the n junctions are ramped up (see text). The 3D density plots are isosurfaces obtained from 3D GPE numerical simulations of the experimental set-up. If n is below a critical value n_c depending on w_0, the initial current is dissipated via the nucleation of vortices (here $n = 2$ and vortices are highlighted by orange cycling arrows in the upper right plot). Conversely, if $n \geq n_c$ (here $n = 4$), the system remains stable with $w = w_0$ (lower right plot). (b) Examples of single-shot experimental in-situ images and interferograms obtained for $w_0 = 2$ and for the same number of junctions n as in (a): $n = 2$ (unstable configuration), at $t = 0$ (*i*), $t = 1$ ms (*ii*) and $t = 7$ ms (*iii*); and $n = 4$ (stable configuration) for $t = 0$ ms (*iv*), $t = 1$ ms (*v*) and $t = 20$ ms (*vi*). In the case (*iii*), the circulation has decayed ($w(t) < w_0$) and the vortex emission is identified by the single spiral arm and the presence of a localized region of low density, i.e. a vortex.

This vortex emission is the 3D analogue of the observed simultaneous nucleation of n solitons in 1D simulations in the unstable regime. If n is increased above n_c, then the emission of vortices is suppressed and the circulation remains constant in time. A higher stable circulation corresponds to a larger critical current.

5.3 Experimental system and persistent current states

We investigate experimentally the predicted increase of current stability in JJNs by realizing a Bose-Einstein condensate (BEC) of ^{6}Li molecules in an annular trap equipped with a variable number ($n \leq 16$) of static planar junctions. Both the ring-shaped trap and the array of junctions are produced by the same digital micromirror device (DMD) illuminated with blue-detuned light to provide a repulsive optical

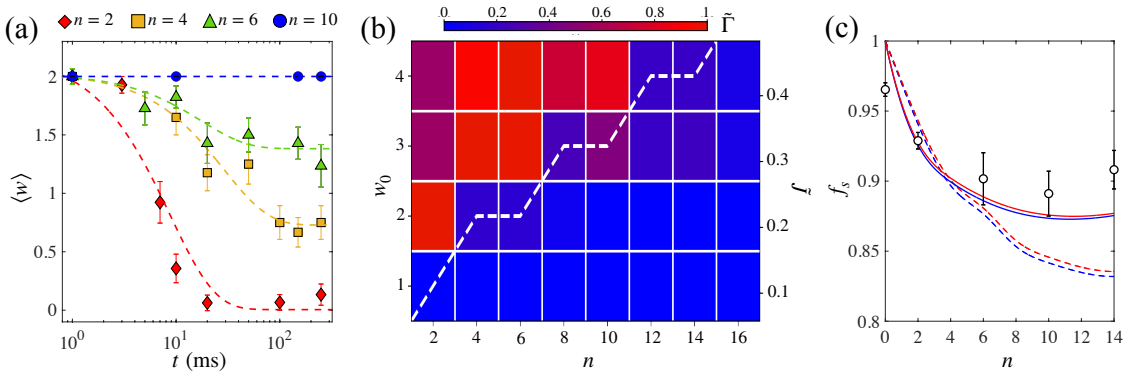

Figure 5.4: Stability phase diagram of an atomtronic JJN. (a) Mean circulation as a function of time, for $w_0 = 2$ and different number of barriers, n (symbols), with averages and error bars obtained from ~ 15 repeated measurements for each point. The dashed lines are exponential fits, $\langle w(t) \rangle = w_f + \Delta w \exp(-\Gamma t)$. (b) Effective decay rate $\tilde{\Gamma} \propto \Delta w \, \Gamma$ (colormap), extracted from the exponential fits as in panel (a) as a function of w_0 and n. $\tilde{\Gamma}$ quantifies the stability of an initial finite-circulation state w_0. The dashed white line is the critical circulation $w_c(n)$ and the corresponding current (right axis) as a function of n, obtained from 3D GPE simulations. (c) Upper (dashed red line) and lower (dashed blue line) bounds to the superfluid fraction f_s, Eq. (5.8), as a function of the number of junctions. Bounds are obtained from the ground state density of the numerical GPE. The solid lines are the bounds evaluated by including the finite resolution of the experimental imaging system. Circles are the upper bound evaluated using experimental in-situ images and averaged over 10 realizations.

potential. Using the high resolution of the DMD projection setup, we create a dark ring-shaped region in the x-y plane delimited by hard walls whose height is much larger than the chemical potential of the superfluid (given by $\mu/h \simeq 850$ Hz in the clean ring), with $R_{\rm in} \simeq 11.7 \pm 0.2$ μm and $R_{\rm rout} \simeq 20.6 \pm 0.2$ μm being the inner and outer radius of the annulus. The potential is completed by a tight harmonic confinement along the vertical z direction, of trapping frequency $\omega_z = 2\pi \times (383 \pm 2)$ Hz. The junctions can be modelled as Gaussian peaks of initial height $V_0 \simeq (1.3 \pm 0.2)\,\mu$ and $1/e^2$-width $\sigma = (1.2 \pm 0.2)\,\xi$, with $\xi \approx 0.68$ μm being the healing length. We initially trap $\simeq 6.8 \times 10^3$ condensed atom pairs inside the ring with a shot-to-shot stability around 5%. Due to the finite lifetime of our molecular BEC, the pair number decreases over the course of the current decay by at most 20%, causing a decrease of the chemical potential of the superfluid. Consequently the value of V_0/μ increases by up to $\sim 15\%$ depending on the holding time.

We initialize the superfluid ring in a quantized circulation state with winding number $w_0 \in \{1,2,3,4\}$. Following the procedure described in Ref. [174], different values of w_0 are obtained on-demand by shining a DMD-made azimuthal light intensity gradient onto the ring over a duration $t_I \ll \hbar/\mu$, i.e. shorter than the characteristic density response time, $\hbar/\mu$. In this way, we imprint a phase $\Phi(\theta) = U_0(\theta) \times t_I/\hbar$ to the condensate wavefunction without modifying the atomic density [211], where $U_0(\theta)$ is the spin-independent potential exerted by the light field on the atomic states that varies linearly with θ [174]. After the imprinting, we wait 300 ms to let the cloud reach equilibrium, allowing the possible density excitations following the imprinting procedure to damp out [187]. We then progressively ramp up the n Gaussian junctions over approximately 1 ms (corresponding to $\approx 6\,\hbar/\mu$).

5.4 Stability phase diagram

To measure the winding w in the ring, we exploit an interferometric probe [174, 178, 214]: we equip the atomic superfluid with a central disk acting as a phase reference (see panels (*i*) and (*iv*) in Figure 5.3(b)) and measure the relative phase between the disk and the ring from the interference pattern arising after a short time-of-flight. The number of spiral arms in the interferogram provides access to the value of the circulation (winding number) at time t, $w(t)$. The different panels of Figure 5.3(b) display typical examples of experimental images. In panels (*i*) and (*iv*) we show the in-situ atomic density profile at $t = 0$. The atomic density (averaged over 10 experimental images) is characterized by a homogeneous bulk both in the azimuthal and radial directions. The $n = 2$ (*i*) and $n = 4$ (*iv*) junctions are clearly visible and are associated to local dips in the density, similarly as in Figure 5.1 and Figure 5.3(a). In panels (*ii*) and (*iii*) we show examples of spiral interference patterns emerging for an unstable dynamics, namely $w(t)$ decreasing in time below w_0 (here, $w_0 = 2$ and $n = 2$): in (*ii*) $t = 1$ ms and $w(t) = 2$, while in (*iii*) $t = 7$ ms and $w(t) = 1$. In particular, panel (*iii*) shows the presence of a vortex identified as a localized low-density defect and marked by the orange arrow. The vortex emission signals the decrease of w by one quantum. In panels (*v*) and (*vi*) we show instead the interferograms for stable dynamics, namely $w(t) = w_0$ (here, $w_0 = 2$ and $n = 4$). A non-circular, polygonal interference pattern is visible both at short ((*v*), $t = 1$ ms) and at long ((*vi*), $t = 20$ ms) times due to the sharp phase gain at the junctions.

By averaging the winding number over $\sim$ 15 experimental realizations under

the same conditions, we extract the evolution of the mean circulation $\langle w(t) \rangle$ for various n. We study the dynamics up to 250 ms, which is sufficient to observe steady current states at long-times while still limiting particle losses. The measured $\langle w(t) \rangle$ is shown in Figure 5.4(a) for $w_0 = 2$. We fit each curve with an exponential decay given by $\langle w(t) \rangle = w_f + \Delta w \exp(-\Gamma t)$. The fitting parameters w_f, Δw and Γ allow us to characterize the mean supercurrent. As $\langle w(t) \rangle$ is obtained from statistical averaging, the figure shows that the number of realizations $w(t)$ that remain stable in time increases with the number of junctions. In particular, the number of stable realizations increases substantially when changing the number of junctions from $n = 2$ (red diamonds) to $n = 4$ (yellow squares). For $n = 10$ (blue circles), all realizations are stable: this demonstrates the experimental capability to create stable finite-circulation states in a JJN.

Figure 5.4(b) summarizes the results obtained for different w_0 and n, in the form of a stability phase diagram. In particular, we plot the quantity $\tilde{\Gamma} = \Delta w\, \Gamma / \max_n(\Delta w\, \Gamma)$, where each horizontal line of the phase diagram is normalized to its maximum value for fixed w_0. This quantity combines information on the difference between the initial and the final winding numbers, Δw, namely how much the currents decay, and on the timescale over which this decay takes place, Γ. Values of $\tilde{\Gamma} \approx 1$ (red regions) are obtained when most of the realizations $w(t)$ rapidly decay towards values of the circulation lower than the initial w_0. On the contrary, small values of $\tilde{\Gamma} \approx 0$ (blue regions) are obtained when most of the realizations are stable over time, namely $w(t) = w_0$. The phase diagram clearly shows that, on average, the system supports a higher number of stable realizations when increasing the number of junctions. By the choice of normalization, $\tilde{\Gamma}$ shows a sharp transition from $\tilde{\Gamma} \approx 1$ to $\tilde{\Gamma} \approx 0$ when increasing n. The dashed white line in Figure 5.3(b) denotes the critical winding number $w_c(n)$ and the corresponding current (right axes) as a function of n, as computed numerically from 3D GPE simulations. The numerical critical curve $w_c(n)$ is obtained for $V_0/\mu = 1.8$ and match the experimental phase diagram well. The need for a larger V_0/μ in numerical simulations with respect to the one estimated in the experiment, is consistent with the finite lifetime of the sample (which implies that V_0/μ increases during the dynamics) and the finite resolution of the DMD potential, which makes the barriers not perfectly identical. Anyway, we note that the only effect of a change of V_0/μ on the critical line $w_c(n)$ is to provide a linear shift, meaning that the particular choice of V_0/μ does not affect its trend, which well reproduce the experimental findings.

Given that $\tilde{J}_c(n) \sim n\, f_c(n)$ from Eq. (5.7), a significant decrease of the superfluid fraction $f_s \geq f_c$ would overshadow the stabilization mechanism arising from increasing n. For this reason, in Figure 5.4(c), we study the dependence of f_s on n and indeed find a mildly decreasing trend, which is insufficient to disrupt the enhanced stability of currents for large n. According to a variational calculation by Leggett [15, 120], the superfluid fraction f_s can be bounded experimentally from the in-situ density profile [19, 212, 213]:

$$\iint \frac{dz\, dr\; r}{\frac{1}{d^2}\int_{\text{cell}} \frac{d\theta}{\rho(r,\theta,z)}} \leq f_s \leq \left(\frac{1}{d^2}\int_{\text{cell}} \frac{d\theta}{\iint dz\, dr\; r\rho(r,\theta,z)}\right)^{-1}, \tag{5.8}$$

where the density $\rho(r,\theta,z)$ is calculated from the ground state of the 3D GPE. The bounds in Eq. (5.8) are computed by restricting the azimuthal angle θ over a unit cell of size $d = 2\pi/n$ and using the normalization $\iint dz\, dr\; r \int_{\text{cell}} d\theta\, \rho(r,\theta,z) = 1$ [15, 105, 120]. In Figure 5.4 we plot the upper (dashed red line) and lower (dashed blue line) bounds in Eq. (5.8). They are very close to each other as our system is approximately separable in the transverse spatial directions [212] and coincide in 1D, where $f_s = \lim_{w=0,\ \Omega\to 0} f(\tilde{w}, n)$ [34]. Increasing n enhances the size of the density dip relative to the unit cell length and thus decreases both the lower and upper limits in Eq. (5.8), see Figure 5.4(c). Experimentally, for each value of n, we compute Leggett's upper bound on 10 different images of the experimental density. We compute the integral on the right-hand side of Eq. (5.8) by summing over all pixels inside an annular region with inner and outer radii $r_{cut1} > R_{in}$ and $r_{cut2} < R_{out}$ respectively. We have numerically verified that the values of the bounds do not depend on the exact size of this region. The corresponding mean values and standard deviations are shown as circles in Figure 5.4(a). The deviations from $f_s = 1$ in the clean torus ($n = 0$) are mainly due to noise in the experimental images, as well as the finite pixel size of our imaging sensor. Experimental results are well reproduced when taking into account the finite resolution of the imaging system (solid blue and red lines) and clearly show a decrease of f_s with n.

5.5 Superfluid fraction and the $f(\tilde{w}, n)$ function

The superfluid fraction for neutral atoms in a ring trap rotating at an angular velocity Ω can be defined as [15, 120]

$$f_s = 1 - \lim_{\Omega\to 0} \frac{L}{I_{\text{cl}}\Omega} \tag{5.9}$$

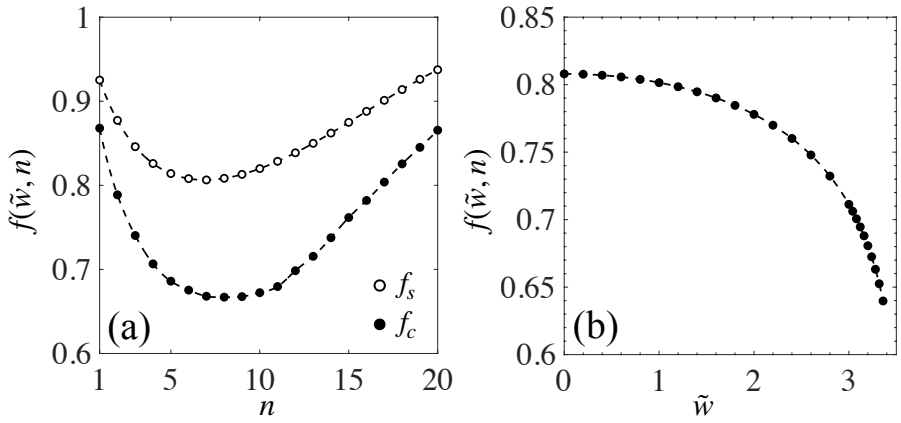

Figure 5.5: Function $f(\tilde{w}, n)$ calculated for stationary states of the 1D GPE. Panel (a) plots $f(\tilde{w}, n)$ as a function of n for two interesting cases: $f_c(n) = f(\tilde{w} = \tilde{w}_c, n)$ (dots dots) and $\lim_{w=0,\Omega\to 0} f(\tilde{w}, n) = f_s$ (circles), corresponding to Leggett's superfluid fraction, Eq. (5.10). Panel (b) shows $f(\tilde{w}, n)$ as a function of $\tilde{w}$ and for $n = 6$ (dots). In both panels, lines are guides to the eye.

where L is the expectation value of the angular momentum and $I_{\rm cl}$ is the classical moment of inertia. In 1D, we have

$$f_s = \frac{1}{\frac{1}{d^2}\int_{\rm cell} \frac{d\theta}{\rho(\theta)}}, \tag{5.10}$$

where $\rho(\theta)$ is normalized to one over the unit cell of azimuthal size d. Equation (5.10) is derived by noticing that the two bounds in Eq. (5.8) coincide in 1D. In our case, restricting to the unit cell as in Ref. [15, 120] is not necessary and Eq. (5.10) is unchanged if we write $f_s = \frac{1}{(2\pi)^2}(\int \frac{d\theta}{\rho(\theta)})^{-1}$ with $\rho(\theta)$ normalized to one over the full circle, even in the presence of n junctions. In particular, we have $f_s = \lim_{w=0,\ \Omega\to 0} f(\tilde{w}, n)$, where $f(\tilde{w}, n)$ is related to the current according to Eq. (5.5). In Figure 5.5(a) we plot f_s (circles) and f_c (corresponding to $f(\tilde{w} = \tilde{w}_c, n)$, dots) as a function of n. Both functions decrease with n until the barriers start to overlap. In Figure 5.5(b) we plot $f(\tilde{w}, n)$ as a function of $\tilde{w}$ for $n = 6$.

To compare numerical and experimental data in Figure 5.4(c), we have taken into account the finite spatial resolution of the imaging system, characterized by a Point Spread Function (PSF) of full-witdh-half-maximum FWHM $= 0.83\,\mu$m [215]. To estimate the theoretical curves of Figure 5.4(c), we first integrate the 3D numerical densities along the z direction, Then, we account for the finite experimental resolution by convolving the integrated numerical densities with a two-dimensional Gaussian with a FWHM matching the experimental PSF. This procedure leads

to a decrease in the resolution of the density modulation, which causes the estimated superfluid fraction to increase and yields results in good agreement with experimentally extracted values (see Figure 5.4(c)).

5.6 Discussion

Our work showcases the first experimental observation of ring supercurrents in periodic arrays of Josephson junctions. Such stable currents can be experimentally observed only for a sufficiently large number of links, as predicted by our theory modeling. In particular, our work shows that the maximum current flowing across the atomtronic circuit is due to a cooperative mechanism involving all the junctions rather than only to the properties of the single Josephson link. We expect the mechanism demonstrated in this manuscript to apply to any superfluids and superconductors as it soleley depends on the single valuedness of the wavefunction in a multiply-connected topology.

Therefore, a natural extension of our work will be to investigate whether the same effect stabilizes supercurrents in other annular systems, such as atomic Fermi superfluids [173, 174] and supersolids [216]. In the former case, the condensate fraction differs from unity even at $T = 0$ [215] and additional dissipative effects, such as Cooper pair-breaking [217, 218] may compete with the stabilization mechanism. In the latter, intrinsic density modulations realize an array of self-induced Josephson junctions – as recently demonstrated in Ref. [19] for an elongated atomic system – which can be controlled by tuning the confinement parameters.

Finally, the exquisite controllability offered by our platform opens the way toward realizing exotic quantum superposition of superflow states [200–204] with possible implications in both atomtronic and quantum technologies.

Conclusions

Starting with the beginnings of quantum mechanics in the first chapter, we finally arrived at the present day. We have studied Josephson currents in superfluid and supersolid systems, providing insight into the existence of new phenomena and proposing platforms for new types of quantum technologies.

The description of a supersolid as a self-induced Josephson junction has been theoretically modelled by a generalization of the standard two-mode model of the bosonic Josephson junctions. Despite the absence of an external weak link, which makes the possibility of sustaining josephson oscillations non-trivial, we were able to find a specific regime where we theoretically predict and numerically observe the presence of a single sinusoidal mode, decoupling it from the others. Moreover, we numerically observed the transition to the so-called macroscopic quantum self-trapping regime, characteristic of bosonic Josephson junctions, comparing it with theoretical model, yelding a good agreement. Numerical results and theoretical prediction are compared with exprimental data of the group whos collaboration led to the born of [19]. In this work, the demonstration of Josephson oscillations in a supersolid dipolar quantum gas is performed experimentally, numerically and theoretically. Moreover, we provide a relation between the coupling energy measured by the Josephson effect and the superfluid fraction of the system, as originally defined by Leggett. This relation has allowed us to measure without any doubts the sub-unity value of the superfluid fraction of this supersolid system, through the measure of the Josephson effect. It also provides a novel procedure applicable in other superfluid and superconducting systems showing supersolid-like properties that are now under study. However, the self-induced nature of the supersolid dipolar Josephson junction makes it a promising and rich platfrom to characterize this novel state of matter and provide novel quantum technologies.

The atomtronic Josephson junctions necklace studied in [34] consists instead of a ring-shaped superfluid with a periodic array of Josephson weak links. Ultracold

atoms in toroidal traps with a single or two Josephson junctions have been extensively studied, but the realization of tunable Josephson junctions necklaces with arbitrary number of junctions remains technologically and experimentally challenging, and so far elusive in both superconducting and superfluid platforms. We demonstrate that the critical current supported by a single Josephson junction, before dissipation via vortex nucleation occurs, is enhanced by increasing the number of Josephson junctions along the ring superfluid. Increasing the number of Josephson junctions leads also to a decrease of the supefluid fraction, contrasting with the observed stabilization of the persistent currents. We theoretically predict this stabilization using the single-valuedness of the superfluid wave function, explaining it as a cooperative mechanism involving all the Josephson junctions and not only a single one. We compare numerical simulations with experimental data of the group whos collaboration contributed to the born of this work.

The natural continuation of these works is the study of the supersolid in a ring geometry. This resembles the original definition of the superfluid fraction by Leggett, but even more it allows to study the presence of partially quantized supercurrents and vortices, thanks to the significant value of the superfluid fraction measured. The atomtronic Josephson junctions necklace study would suggests the idea of a better stabilization of supercurrents in a supersolid. The array of Josephson junctions, indeed, creates a periodic modulation in the density resembling the one of the supersolid, which, in contrast, is self-induced. Our theoretical 2M-mode model Eq. (3.18) is easily customisable on a ring geometry, simply by removing the energy offsets due to the harmonic trap and imposing a coupling between the first and last cluster. From a numerical point of view, it is needed to impose the periodic boundary conditions along the direction where the density modulation develops. These works unlock a promising research path full of possibility.

The potential applications of Josephson junctions in quantum computing, precision metrology, and the development of future quantum devices are extensive and exciting. The intersection of Josephson physics and supersolidity presents an exciting frontier that promises rich scientific discoveries and technological innovations. Atomic superfluids in mesoscopic structured ring potentials are excellent candidates for atomtronics applications, with prospects towards the observation of non-trivial macroscopic superpositions of current states.

This thesis has been an account of my personal journey during my PhD, detailing the various interactions I had with researchers both in my group and in

other groups. Just as we study the dynamics and interactions of atoms, which are essential to the phenomena and effects we observe, humans also rely on social interactions and relationships to navigate the world. No individual exists in isolation; we are all interconnected and interdependent. It is the complex and dynamic flow of interacting atoms that leads to extraordinary phenomena, as this thesis has had the audacity to illustrate.

A

Quantum depletion of a BEC

We stated in the main text that, using the Bogoliubov prescription Eq. (1.54)-Eq. (1.55), the quantum depletion of a BEC, that is the number of particles in the ground state with $\mathbf{k} \neq 0$, can be calculated as:

$$N' = \sum_{k \neq 0} \langle n_k \rangle \tag{A.1}$$

The sum can be substituted with an integral:

$$\begin{aligned} N' = \int d\mathbf{n} \langle n_k \rangle = \frac{V}{(2\pi)^3} \int d\mathbf{k} \langle n_k \rangle = \\ = \frac{V}{(2\pi)^3} \int d\mathbf{k} v_k^2 = \frac{V}{(2\pi)^3} \int d\mathbf{k} \frac{1}{2} \left(\frac{E_k^0 + ng}{E_k} - 1 \right) \end{aligned} \tag{A.2}$$

Now, we can write explicitly the energies E_k^0 and E_k and define $ng \equiv \frac{\hbar^2 k_0^2}{2m}$:

$$\begin{aligned} N' = \frac{V}{(2\pi)^3} \int d\mathbf{k} \frac{1}{2} \left(\frac{\frac{\hbar^2 k^2}{2m} + \frac{\hbar^2 k_0^2}{2m}}{\sqrt{\left(\frac{\hbar^2 k^2}{2m}\right)^2 + 2ng \frac{\hbar^2 k^2}{2m}}} - 1 \right) = \\ = \frac{V}{2(2\pi)^3} \int 4\pi k^2 dk \left(\frac{k^2 + k_0^2}{\sqrt{k^4 + 2k^2 k_0^2}} - 1 \right) \end{aligned} \tag{A.3}$$

where we have integrated over the angles in spherical coordinates because the integrand depends only on the modululs of $\mathbf{k}$. With the substitution $x = k/k_0$, so

$dx = dk/k_0$, we have:

$$N' = \frac{Vk_0^3}{4\pi^2}\int_0^{+\infty} dx x\left(\frac{x^2+1}{\sqrt{x^2+2}} - 1\right) \tag{A.4}$$

The next substitution is $x^2 + 2 = 2\cosh^2\alpha$, so that $xdx = 2\cosh\alpha\sinh\alpha d\alpha$ and then:

$$\begin{aligned} N' &= \frac{Vk_0^3}{4\pi^2}\int_0^{+\infty} d\alpha 2\cosh\alpha\sinh\alpha\left(\frac{2\cosh^2\alpha - 1}{\sqrt{2}\cosh\alpha} - \sqrt{2\cosh^2\alpha - 2}\right) = \\ &= \frac{Vk_0^3}{4\pi^2}\int_0^{+\infty} d\alpha\left[\sqrt{2}\sinh\alpha(2\cosh^2\alpha - 1) - 2\sqrt{2}\cosh\alpha\sinh^2\alpha\right) = \\ &= \frac{Vk_0^3}{2\sqrt{2}\pi^2}\left[\int d(\cosh\alpha)(2\cosh^2\alpha - 1) - 2\int d(\sinh\alpha)\sinh^2\alpha\right] = \\ &= \frac{Vk_0^3}{2\sqrt{2}\pi^2}\left[\frac{2}{3}\cosh^3\alpha - \cosh\alpha - \frac{2}{3}\sinh^3\alpha\right]\Big|_{\alpha=0}^{+\infty} \end{aligned} \tag{A.5}$$

At this point we need the expression of the hyperbolic functions in term of exponentials:

$$\begin{aligned} \cosh y &= \frac{e^y + e^{-y}}{2} \\ \cosh^3 y &= \frac{1}{8}(e^{3y} + 3e^y + 4 + 3e^{-y} + e^{-3y}) \\ \sinh^3 y &= \frac{1}{8}(e^{3y} - 3e^y + 4 + 3e^{-y} - e^{-3y}) \end{aligned} \tag{A.6}$$

Therefore:

$$\begin{aligned} N' &= \frac{Vk_0^3}{2\sqrt{2}\pi^2}\left[\frac{1}{6}(3e^y + e^{-3y}) - \frac{e^y + e^{-y}}{2}\right]\Big|_{\alpha=0}^{+\infty} = \\ &= \frac{Vk_0^3}{4\sqrt{2}\pi^2}\left[\frac{e^{-3y}}{3} - e^{-y}\right]\Big|_{\alpha=0}^{+\infty} = \\ &= \frac{Vk_0^3}{4\sqrt{2}\pi^2}\left(1 - \frac{1}{3}\right) \\ &= \frac{Vk_0^3}{4\pi^2}\frac{\sqrt{2}}{3} \end{aligned} \tag{A.7}$$

Putting together the definitions of g:

$$\begin{aligned} \frac{\hbar^2 k_0^2}{2m} &= ng = n\frac{4\pi\hbar^2 a}{m} \\ k_0^2 &= 8\pi a n \end{aligned} \tag{A.8}$$

we finally obtain the density of the quantum depletion:

$$n' \equiv \frac{N'}{V} = \frac{1}{4\pi^2}\frac{\sqrt{2}}{3}(8\pi a n)^{3/2} = \frac{8}{3\sqrt{\pi}}(na)^{3/2} \tag{A.9}$$

If we divide it by the total atom number density, we have:

$$\frac{n'}{n} = \frac{8}{3\sqrt{\pi}}(na^3)^{1/2} \tag{A.10}$$

that is exactly the equation Eq. (1.69).

B

Derivation of the two mode model for a dSJJ and beyond

In this appendix we are going to derive the two-mode model for the dSJJ retaining also higher order terms in the approximation of zero overlap between spatial wavefunctions. We will derive the results presented in subsection 3.2.2 and than the procedure used by Ananikian *et al.*[219].
The procedure that we are going to employ consists in substituting the two-mode ansatz

$$\psi(\mathbf{r},t) = \psi_1(t)\phi_1(\mathbf{r}) + \psi_2(t)\phi_2(\mathbf{r}) \tag{B.1}$$

inside the eGPE Eq. (3.3) describing the dipolar supersolid

$$\begin{aligned} i\frac{\partial\psi(\mathbf{r},t)}{\partial t} = \Bigg[&-\frac{\nabla^2}{2m} + V_t(\mathbf{r}) + g|\psi(\mathbf{r},t)|^2 + \int d\mathbf{r}' V_{dd}(\mathbf{r}-\mathbf{r}')|\psi(\mathbf{r}',t)|^2 \\ &+ \gamma(\epsilon_{dd})|\psi(\mathbf{r},t)|^3\Bigg]\psi(\mathbf{r},t) \end{aligned} \tag{B.2}$$

This substitution and than its projection onto ϕ_1 gives

$$\begin{aligned} i\frac{\partial\psi_1}{\partial t} &= \int d\mathbf{r}\ \phi_1\Big(-\frac{\nabla^2}{2m}+V_t(\mathbf{r})\Big)(\psi_1\phi_1+\psi_2\phi_2)+ \\ &+g\int d\mathbf{r}\ \phi_1\Big(|\psi_1|^2\phi_1^2+|\psi_2|^2\phi_2^2+(\psi_1^*\psi_2+\psi_1\psi_2^*)\phi_1\phi_2\Big)(\psi_1\phi_1+\psi_2\phi_2)+ \\ &+\int d\mathbf{r}\phi_1(\psi_1\phi_1+\psi_2\phi_2)\ \int d\mathbf{r}'\ V_{dd}(|\mathbf{r}-\mathbf{r}'|)\Big(|\psi_1|^2\phi_1'^2+|\psi_2|^2\phi_2'^2+(\psi_1^*\psi_2+\psi_1\psi_2^*)\phi_1'\phi_2'\Big)+ \\ &+\gamma(\epsilon_{dd})\ \int d\mathbf{r}\ \phi_1\Big(|\psi_1|^2\phi_1^2+|\psi_2|^2\phi_2^2+(\psi_1^*\psi_2+\psi_1\psi_2^*)\phi_1\phi_2\Big)^{3/2}(\psi_1\phi_1+\psi_2\phi_2) \end{aligned} \tag{B.3}$$

Isolating the temporal terms, we have

$$\begin{aligned} i\frac{\partial\psi_1}{\partial t} &= -\psi_1K_{11}-\psi_2K_{12}+|\psi_1|^2\psi_1U_{1111}+|\psi_1|^2\psi_2U_{1112}+|\psi_2|^2\psi_1U_{1221}+|\psi_2|^2\psi_2U_{1222}+ \\ &+(\psi_1^*\psi_2+\psi_1\psi_2^*)\psi_1U_{1121}+(\psi_1^*\psi_2+\psi_1\psi_2^*)\psi_2U_{1122}+|\psi_1|^2\psi_1D_{1111}+|\psi_1|^2\psi_2D_{1211}+ \\ &+|\psi_2|^2\psi_1D_{1122}+|\psi_2|^2\psi_2D_{1222}+(\psi_1^*\psi_2+\psi_1\psi_2^*)\psi_1D_{1112}+(\psi_1^*\psi_2+\psi_1\psi_2^*)\psi_2D_{1212}+\text{LHY} \end{aligned} \tag{B.4}$$

where we didn't write the LHY term and we have defined

$$\begin{aligned} K_{ij} &\equiv -\int d\mathbf{r}\ \phi_i(\mathbf{r})\Big(-\frac{\nabla^2}{2m}+V_t(\mathbf{r})\Big)\phi_j(\mathbf{r}) \\ U_{\alpha\beta\gamma\delta} &\equiv g\int d\mathbf{r}\ \phi_\alpha(\mathbf{r})\phi_\beta(\mathbf{r})\phi_\gamma(\mathbf{r})\phi_\delta(\mathbf{r}) \\ D_{\alpha\beta\gamma\delta} &\equiv \int d\mathbf{r}\ \phi_\alpha(\mathbf{r})\phi_\beta(\mathbf{r})\int d\mathbf{r}'\ V_{dd}(|\mathbf{r}-\mathbf{r}'|)\phi_\gamma'(\mathbf{r})\phi_\delta'(\mathbf{r}) \quad . \end{aligned} \tag{B.5}$$

Note some properties of these coefficients. The tunnelling K_{ij} is symmetric under exchange of indices

$$\begin{aligned} K_{ij} &\equiv -\int d\mathbf{r}\ \phi_i(\mathbf{r})\Big(-\frac{\nabla^2}{2m}+V_t(\mathbf{r})\Big)\phi_j(\mathbf{r}) = \\ &= \frac{1}{2m}\int d\mathbf{r}\ \phi_i(\mathbf{r})\Big(\nabla^2\phi_j(\mathbf{r})\Big)-\int d\mathbf{r}\ V_t(\mathbf{r})\phi_i(\mathbf{r})\phi_j(\mathbf{r}) = \\ &= -\frac{1}{2m}\int d\mathbf{r}\ \Big(\nabla\phi_i(\mathbf{r})\Big)\cdot\Big(\nabla\phi_j(\mathbf{r})\Big)-\int d\mathbf{r}\ V_t(\mathbf{r})\phi_j(\mathbf{r})\phi_i(\mathbf{r}) = \\ &= \frac{1}{2m}\int d\mathbf{r}\ \phi_j(\mathbf{r})\Big(\nabla^2\phi_i(\mathbf{r})\Big)-\int d\mathbf{r}\ V_t(\mathbf{r})\phi_j(\mathbf{r})\phi_i(\mathbf{r}) \equiv K_{ji} \end{aligned} \tag{B.6}$$

where we have utilized the integration by parts technique to shift the nabla operator within the first integral, discarding the boundary term where the spatial wavefunctions vanish. The contact interaction coefficient U is symmetrical with respect to any rearrangement of its indices, as it is the integral of a product of wavefunctions.

Conversely, the dipolar interaction coefficient $D_{\alpha\beta\gamma\delta}$ retains its form when swapping the first two indices with each other or the third and fourth with each other, as it involves two distinct integrals.

To deal with the LHY term, we recall that we are in the limit of zero overlap approximation, thus

$$\begin{aligned}
&\gamma \int d\mathbf{r}\ \phi_1\Big(|\psi_1|^2\phi_1^2 + |\psi_2|^2\phi_2^2 + (\psi_1^*\psi_2 + \psi_1\psi_2^*)\phi_1\phi_2\Big)^{3/2}(\psi_1\phi_1 + \psi_2\phi_2) \cong \\
&\cong \gamma(\epsilon_{dd}) \int d\mathbf{r}\ \phi_1\Big(|\psi_1|^2\phi_1^2 + |\psi_2|^2\phi_2^2\Big)^{3/2}(\psi_1\phi_1 + \psi_2\phi_2) = \\
&= \gamma\psi_1 \int d\mathbf{r}\ \phi_1\Big(|\psi_1|^2\phi_1^2\phi_1^{2/3} + \cancel{|\psi_2|^2\phi_2^2\phi_1^{2/3}}\Big)^{3/2} + \gamma\psi_2 \int d\mathbf{r}\ \phi_1\Big(\cancel{|\psi_1|^2\phi_1^2\phi_2^{2/3}} + |\psi_2|^2\phi_2^2\phi_2^{2/3}\Big)^{3/2} \cong \\
&\cong \gamma|\psi_1|^3\psi_1 \int d\mathbf{r}\ \phi_1^5 + \gamma|\psi_2|^3\psi_2 \cancel{\int d\mathbf{r}\ \phi_1\phi_2^4} \cong \gamma|\psi_1|^3\psi_1 \int d\mathbf{r}\ \phi_1^5
\end{aligned} \tag{B.7}$$

Defining

$$L_i \equiv \gamma \int d\mathbf{r}\ \phi_i^5(\mathbf{r}) \quad , \tag{B.8}$$

the LHY term assumes the simple form[1]

$$|\psi_1|^3\psi_1 L_1 \quad . \tag{B.9}$$

By analogy with Eq. (B.3), we substitute the two-mode ansatz Eq. (3.4) within Eq. (3.3), but this time we project onto ϕ_2

$$\begin{aligned}
i\frac{\partial\psi_2}{\partial t} &= \int d\mathbf{r}\ \phi_2\Big(-\frac{\nabla^2}{2m} + V_t(\mathbf{r})\Big)(\psi_1\phi_1 + \psi_2\phi_2) + \\
&+ g\int d\mathbf{r}\ \phi_2\Big(|\psi_1|^2\phi_1^2 + |\psi_2|^2\phi_2^2 + (\psi_1^*\psi_2 + \psi_1\psi_2^*)\phi_1\phi_2\Big)(\psi_1\phi_1 + \psi_2\phi_2) + \\
&+ \int d\mathbf{r}\phi_2(\psi_1\phi_1 + \psi_2\phi_2) \int d\mathbf{r}'\ V_{dd}(|\mathbf{r} - \mathbf{r}'|)\Big(|\psi_1|^2\phi_1'^2 + |\psi_2|^2\phi_2'^2 + (\psi_1^*\psi_2 + \psi_1\psi_2^*)\phi_1'\phi_2'\Big) + \\
&+ \gamma(\epsilon_{dd}) \int d\mathbf{r}\ \phi_2\Big(|\psi_1|^2\phi_1^2 + |\psi_2|^2\phi_2^2 + (\psi_1^*\psi_2 + \psi_1\psi_2^*)\phi_1\phi_2\Big)^{3/2}(\psi_1\phi_1 + \psi_2\phi_2)
\end{aligned} \tag{B.10}$$

Using the definitions Eq. (B.5) and Eq. (B.8), an equation similar to Eq. (B.4) is

[1] One might wonder why in the LHY term we are sending away integrals with overlaps, while in all others we are not. Actually we could do that, but I would like to wait as long as possible so that I can then generalise the calculus.

obtained

$$\begin{aligned} i\frac{\partial\psi_2}{\partial t} = &-\psi_1 K_{21} - \psi_2 K_{22} + |\psi_1|^2\psi_1 U_{2111} + |\psi_1|^2\psi_2 U_{2112} + |\psi_2|^2\psi_1 U_{2221} + |\psi_2|^2\psi_2 U_{2222} + \\ &+(\psi_1^*\psi_2 + \psi_1\psi_2^*)\psi_1 U_{2121} + (\psi_1^*\psi_2 + \psi_1\psi_2^*)\psi_2 U_{2122} + |\psi_1|^2\psi_1 D_{2111} + |\psi_1|^2\psi_2 D_{2211} + \\ &+|\psi_2|^2\psi_1 D_{2122} + |\psi_2|^2\psi_2 D_{2222} + (\psi_1^*\psi_2 + \psi_1\psi_2^*)\psi_1 D_{2112} + (\psi_1^*\psi_2 + \psi_1\psi_2^*)\psi_2 D_{2212} + \\ &+|\psi_2|^3\psi_2 L_2 \end{aligned} \tag{B.11}$$

where we treated the LHY as before.
Let us define the quantities we want to study the dynamics of, that is the population and phase imbalances between the two wells

$$Z \equiv \frac{N_1 - N_2}{N} \quad , \quad \Delta\theta \equiv \theta_2 - \theta_1 \quad . \tag{B.12}$$

Remembering Eq. (3.6), it is valid

$$\begin{aligned} |\psi_1|^2 = N_1 &= \frac{N}{2}(1+Z) \\ |\psi_2|^2 = N_2 &= \frac{N}{2}(1-Z) \\ (\psi_1^*\psi_2 + \psi_1\psi_2^*) = 2\sqrt{N_1 N_2}\cos\Delta\theta &= N\sqrt{1-Z^2}\cos\Delta\theta \end{aligned} \tag{B.13}$$

The goal now is to rewrite both Eq. (B.4) and Eq. (B.11) as a function only of z and $\Delta\theta$. Let us start gathering the terms containing ψ_1 and ψ_2

$$\begin{aligned} i\frac{\partial\psi_1}{\partial t} = \psi_1\Bigg[&- K_{11} + \frac{N}{2}(1+Z)U_{1111} + \frac{N}{2}(1-Z)U_{1122} + N\sqrt{1-Z^2}\cos\Delta\theta U_{1112} + \\ &+\frac{N}{2}(1+Z)D_{1111} + \frac{N}{2}(1-Z)D_{1122} + N\sqrt{1-Z^2}\cos\Delta\theta D_{1112} + \frac{N\sqrt{N}}{2\sqrt{2}}(1+Z)^{3/2}L_1\Bigg] + \\ +\psi_2\Bigg[&- K_{12} + \frac{N}{2}(1+Z)U_{1112} + \frac{N}{2}(1-Z)U_{1222} + N\sqrt{1-Z^2}\cos\Delta\theta U_{1122} + \\ &+\frac{N}{2}(1+Z)D_{1211} + \frac{N}{2}(1-Z)D_{1222} + N\sqrt{1-Z^2}\cos\Delta\theta D_{1212}\Bigg] \\ &\equiv C_1\psi_1 + C_2\psi_2 \end{aligned} \tag{B.14}$$

$$
\begin{aligned}
i\frac{\partial\psi_2}{\partial t} = \psi_1\Bigg[&- K_{21} + \frac{N}{2}(1+Z)U_{2111} + \frac{N}{2}(1-Z)U_{1222} + N\sqrt{1-Z^2}\cos\Delta\theta U_{1212} + \\
&+\frac{N}{2}(1+Z)D_{2111} + \frac{N}{2}(1-Z)D_{2122} + N\sqrt{1-Z^2}\cos\Delta\theta D_{2112}\Bigg] + \\
+\psi_2\Bigg[&- K_{22} + \frac{N}{2}(1+Z)U_{2112} + \frac{N}{2}(1-Z)U_{2222} + N\sqrt{1-Z^2}\cos\Delta\theta U_{2122} + \\
+\frac{N}{2}(1+Z)D_{2211} &+ \frac{N}{2}(1-Z)D_{2222} + N\sqrt{1-Z^2}\cos\Delta\theta D_{2212} + \frac{N\sqrt{N}}{2\sqrt{2}}(1-Z)^{3/2}L_2\Bigg] \\
&\equiv C_2\psi_1 + C_3\psi_2
\end{aligned}
\tag{B.15}
$$

where we have called C_1, C_2, C_3 the coefficients inside the square brakets and we have noticed that two of them are equal (C_2). Calculating the derivatives of $\psi_{1,2}$

$$
\frac{\partial\psi_j}{\partial t} = \frac{\dot{N}_j}{2\sqrt{N_j}}e^{i\theta_j} + i\sqrt{N_j}\dot{\theta}_j e^{i\theta_j} \qquad \forall j = 1{,}2 \tag{B.16}
$$

we can rewrite Eq. (B.14) and Eq. (B.15) as

$$
\begin{cases}
i\frac{\dot{N}_1}{2\sqrt{N_1}}e^{i\theta_1} - \sqrt{N_1}\dot{\theta}_1 e^{i\theta_1} = \sqrt{N_1}e^{i\theta_1}C_1 + \sqrt{N_2}e^{i\theta_2}C_2 \\
i\frac{\dot{N}_2}{2\sqrt{N_2}}e^{i\theta_2} - \sqrt{N_2}\dot{\theta}_2 e^{i\theta_2} = \sqrt{N_1}e^{i\theta_1}C_2 + \sqrt{N_2}e^{i\theta_2}C_3
\end{cases}
\tag{B.17}
$$

Simplifying the exponentials and multiplying by the square root of the particles number, we have

$$
\begin{cases}
i\frac{\dot{N}_1}{2} - N_1\dot{\theta}_1 = N_1C_1 + \sqrt{N_1N_2}e^{i\Delta\theta}C_2 \\
i\frac{\dot{N}_2}{2} - N_2\dot{\theta}_2 = \sqrt{N_1N_2}e^{-i\Delta\theta}C_2 + N_2C_3
\end{cases}
\tag{B.18}
$$

In order to obtain an equation for $\dot{Z}$, let us subtract the imaginary parts of the two equations (first minus second)

$$
\begin{aligned}
\frac{\dot{N}_1 - \dot{N}_2}{2} &= 2C_2\sqrt{N_1N_2}\sin\Delta\theta \\
\dot{Z} &= 2C_2\sqrt{1-Z^2}\sin\Delta\theta
\end{aligned}
\tag{B.19}
$$

Let us calculate the explicit form of the coefficient, isolating the dependences from Z and $\Delta\theta$

$$
\begin{aligned}
C_2 = -K_{12} + \frac{N}{2}(U_{1112} + U_{1222} + D_{1211} + D_{1222}) + Z(U_{1112} - U_{1222} + D_{1211} - D_{1222}) + \\
+N\sqrt{1-Z^2}\cos\Delta\theta(U_{1212} + D_{1212})
\end{aligned}
\tag{B.20}
$$

This means that, in the zero overlap limit, the lowest order is

$$\dot{Z} = -2K_{12}\sqrt{1-Z^2}\sin\Delta\theta \tag{B.21}$$

Going back to the system Eq. (B.18), this time we look for the phase evolution, so we isolate the terms containing $\dot{\theta}$. In order to do that, we divide the first equations by N_1 and the second one by N_2. After, we subtract their real parts (first minus second one)

$$\begin{aligned}\dot{\Delta\theta} &= C_1 + C_2\sqrt{\frac{N_2}{N_1}}\cos\Delta\theta - C_2\sqrt{\frac{N_1}{N_2}}\cos\Delta\theta - C_3 = \\ &= C_1 - C_3 + C_2\left(\sqrt{\frac{1-Z}{1+Z}} - \sqrt{\frac{1+Z}{1-Z}}\right)\cos\Delta\theta = \\ &= C_1 - C_3 - 2C_2\frac{Z}{\sqrt{1-Z^2}}\cos\Delta\theta\end{aligned} \tag{B.22}$$

The xeplicit form of $C_1 - C_3$ is

$$\begin{aligned}C_1 - C_3 = -K_{11} + K_{22} + \frac{N}{2}\Big(U_{1111} - BU_{2222} + D_{1111} - D_{2222} - D_{2211} + D_{1122}\Big) + \\ + Z\frac{N}{2}\Big(U_{1111} + U_{2222} - 2U_{1122} + D_{1111} + D_{2222} - D_{2211} - D_{1122}\Big) + \\ + N\sqrt{1-Z^2}\cos\Delta\theta\,\Big(U_{1112} - U_{1222} + D_{1112} - D_{2212}\Big) + \qquad \text{(B.23)} \\ \left(\frac{N}{2}\right)^{3/2}\Big((1+Z)^{3/2}L_1 - (1-Z)^{3/2}L_2\Big) \qquad \text{(B.24)}\end{aligned}$$

which, still in the zero-overlap limit, becomes

$$\begin{aligned}C_1 - C_3 \cong K_{22} - K_{11} + \frac{N}{2}\Big(U_{1111} - U_{2222} + D_{1111} - D_{2222}\Big) + \\ + Z\frac{N}{2}\Big(U_{1111} + U_{2222} + D_{1111} + D_{2222}\Big) + \left(\frac{N}{2}\right)^{3/2}\Big((1+Z)^{3/2}L_1 - (1-Z)^{3/2}L_2\Big) \equiv \\ \equiv A + BZ + C(1+Z)^{3/2} + D(1-Z)^{3/2}\end{aligned} \tag{B.25}$$

where we have defined A, B, C and D in order to highlight the Z dependency. In this way, the equation for $\dot{\Delta\theta}$ is

$$\dot{\Delta\theta} = A + BZ + 2K_{12}\frac{Z}{\sqrt{1-Z^2}}\cos\Delta\theta + C(1+Z)^{3/2} + D(1-Z)^{3/2} \tag{B.26}$$

Rescaling the time variable as for the BJJ

$$t \to 2K_{12}t \quad , \tag{B.27}$$

we obtain a two equations system for Z and $\Delta\theta$

$$\begin{cases} \dot{Z} = -\sqrt{1-Z^2}\sin\Delta\theta \\ \dot{\Delta\theta} = A' + B'Z + \frac{Z}{\sqrt{1-Z^2}}\cos\Delta\theta + C'(1+Z)^{3/2} + D'(1-Z)^{3/2} \end{cases} \tag{B.28}$$

with adimensional coefficients

$$\begin{aligned} A' = \frac{A}{2K_{12}} &= \frac{K_{22}-K_{11}}{2K_{12}} + \frac{N\left(U_{1111}-U_{2222}+D_{1111}-D_{2222}\right)}{4K_{12}} \\ B' = \frac{B}{2K_{12}} &= \frac{N\left(U_{1111}+U_{2222}+D_{1111}+D_{2222}\right)}{4K_{12}} \\ C' = \frac{C}{2K_{12}} &= \frac{N^{3/2}L_1}{2^{5/2}K_{12}} \\ D' = \frac{D}{2K_{12}} &= -\frac{N^{3/2}L_2}{2^{5/2}K_{12}} \quad . \end{aligned} \tag{B.29}$$

The variables Z and $\Delta\theta$ are canonically conjugate with $\dot{Z} = -\frac{\partial H}{\partial\Delta\theta}$ and $\dot{\Delta\theta} = \frac{\partial H}{\partial z}$, where the Hamiltonian is

$$H = A'Z + B'\frac{Z^2}{2} - \sqrt{1-Z^2}\cos\Delta\theta + \frac{2}{5}C'(1+Z)^{5/2} + \frac{2}{5}D'(1-Z)^{5/2} \tag{B.30}$$

which is the Hamiltonian found in subsection 3.2.2.

Implemented two-mode model (I2M)

Following Ananikian's approach, another way of dealing with the two-mode model is to use the symmetries of the wave functions. If before, in fact, we wrote the total wave function as the sum of two wave functions located in the two wells, we now take a further step and write

$$\phi_{1,2} = \frac{\phi_+ \pm \phi_-}{\sqrt{2}} \tag{B.31}$$

where $\phi_{+,-}$ are respectively the ground state, which is symmetrical in space, and the first excited state, which, on the other hand, is antisymmetrical. Their sum or difference results in the $\phi_{1,2}$ located in the two wells. The procedure then is as follows: first we substitute the ansatz Eq. (3.4), then we do the substitution Eq. (B.31), so that we have the spatial part with $\phi_{+,-}$, but the coefficients $\psi_{1,2}$ which we can write as a function of Z and $\Delta\theta$. At this point, we project onto ϕ_+ and ϕ_- in order to use the symmetries of the wave functions to cancel integrals.

The difference with the previous standard two-mode method, consists in cancelling terms exactly, the only approximation clearly remains in the ansatz. Finally, having obtained two equations from the two projections exactly as in the previous case, we calculate the difference between real and imaginary terms, obtaining a system of two equations for Z and $\Delta\theta$. Before going on to write it down explicitly, let us make some further considerations about the coefficients under the symmetric trap hypothesis. Indeed, in this model, we no longer only have the coefficients Eq. (B.29), but we are also going to have

$$\begin{gathered} -K_{12} \equiv K \\ U_{1122} \equiv U_1 \\ U_{1112} = U_{2221} \equiv U_2 \\ D_{1212} \equiv D_1 \\ D_{1122} \equiv D_2 \\ D_{1211} = D_{1222} = D_{2212} = D_{1112} \equiv D_3 \end{gathered} \tag{B.32}$$

where we have used $V_{dd}(\mathbf{r} - \mathbf{r}') = V_{dd}(\mathbf{r}' - \mathbf{r})$. The system assumes the form

$$\begin{cases} \dot{Z} = A\sqrt{1 - Z^2}\sin\phi + D(1 - Z^2)\sin 2\phi \\ \dot{\phi} = BZ + e\frac{Z}{\sqrt{1-Z^2}}\cos\phi + fZ\cos 2\phi + C\Big((1+Z)^{3/2} - (1-Z)^{3/2}\Big) \\ A = 2\Big(K + N(U_2 + D_3)\Big) \\ B = N(U + D - D_1 - D_2 - 2U_1) \\ C = (N/2)^{3/2}L \\ D = N(U_1 + D_1) \\ e = -A \\ f = -D \end{cases} \tag{B.33}$$

where we put ourselves directly into the symmetrical trap case. However, the term multiplying C, which is the contribution of LHY, could not be developed using the symmetries of the wave functions. This is because it contains a cube modulus, so it can be written as the square modulus raised to $3/2$ and the presence of the square root breaks any spatial symmetry. We have therefore calculated that term as in the previous case, i.e. remaining with $\psi_{1,2}$ and using the zero overlap approximation. Rescaling time by $-A$

$$t \to -At \quad , \tag{B.34}$$

we have

$$\begin{cases} \dot{Z} = -\sqrt{1-Z^2}\sin\phi + D'(1-Z^2)\sin 2\phi \\ \dot{\phi} = B'Z + \frac{Z}{\sqrt{1-Z^2}}\cos\phi - D'Z\cos 2\phi + C'\Big((1+Z)^{3/2} - (1-Z)^{3/2}\Big) \end{cases} \tag{B.35}$$

where we used the prime index to indicate the coefficient divided by $-A$

$$\begin{aligned} B' &= \frac{N(U + D - D_1 - D_2 - 2U_1)}{-2\Big(K + N(U_2 + D_3)\Big)} \\ C' &= \frac{(N/2)^{3/2}L}{-2\Big(K + N(U_2 + D_3)\Big)} \\ D' &= \frac{N(U_1 + D_1)}{-2\Big(K + N(U_2 + D_3)\Big)} \end{aligned} \tag{B.36}$$

Let us comment on what these coefficients mean. First of all, D is the new coefficient, the one that quantifies the effects at the next order with respect to the standard two-mode model, in fact it multiplies both terms oscillating at twice the frequency. This also fits with the fact that it contains the terms U_1 and D_1 which are the contact and dipolar interactions with two ϕ_1 and two ϕ_2. The coefficient B, on the other hand, is the analogue of the coefficient of the same name that we had before, i.e. it contains the mean field due to the self-interaction of the individual ϕ, but this time it is corrected, to be precise subtracted by the interaction between the two ϕ (the factor two comes from the fact that I have both the interaction of ϕ_1 on ϕ_2 and vice versa). Finally, C is identical to the previous case, i.e. it is the contribution of LHY. The proof of the correctness of these coefficients is obtained by setting the terms Eq. (B.32) equal to zero.

Considering Z and $\Delta\theta$ as canonically conjugate variables, the related Hamiltonian is

$$H = B'\frac{Z^2}{2} - \sqrt{1-Z^2}\cos\phi + \frac{D'}{2}(1-Z^2)\cos 2\phi + \frac{2}{5}C'\Big((1+Z)^{5/2} + (1-Z)^{5/2}\Big) \tag{B.37}$$

which is equal to the Hamiltonian of the standard two-mode model Eq. (B.30), with the addition of the term oscillating at twice the frequency.

At this point we can calculate the frequency of small oscillations

$$\begin{aligned}
\ddot{Z} &= \frac{Z}{\sqrt{1-Z^2}}\dot{Z}\sin\phi - \sqrt{1-Z^2}\cos\phi\dot{\phi} - 2ZD'\dot{Z}\sin 2\phi + 2D'(1-Z^2)\cos 2\phi\dot{\phi} = \\
&= \left(\frac{Z}{\sqrt{1-Z^2}}\sin\phi - 2ZD'\sin 2\phi\right)\Big(-\sqrt{1-Z^2}\sin\phi + D'(1-Z^2)\sin 2\phi\Big) + \\
&+ \Big(-\sqrt{1-Z^2}\cos\phi + 2D'(1-Z^2)\cos 2\phi\Big)\left(B'Z + \frac{Z}{\sqrt{1-Z^2}}\cos\phi\right. \\
&\quad \left. - D'Z\cos 2\phi + C'\Big((1+Z)^{3/2} - (1-Z)^{3/2}\Big)\right) = \\
&= -Z\sin^2\phi + 3DZ\sqrt{1-Z^2}\sin\phi\sin 2\phi - 2D^2Z(1-Z^2)\sin^2 2\phi \\
&- BZ\sqrt{1-Z^2}\cos\phi \quad - Z\cos^2\phi + 3DZ\sqrt{1-Z^2}\cos\phi\cos 2\phi \\
&+ 2BDZ(1-Z^2)\cos 2\phi - 2D^2Z(1-Z^2)\cos^2 2\phi + \\
&\quad + C\Big((1+Z)^{3/2} - (1-Z)^{3/2}\Big)\Big(-\sqrt{1-Z^2}\cos\phi + 2D'(1-Z^2)\cos 2\phi\Big) = \\
&= -Z + (3D-B)Z\sqrt{1-Z^2}\cos\phi - 2D^2Z(1-Z^2) + 2BDZ(1-Z^2)\cos 2\phi + \\
&\quad + C\Big((1+Z)^{3/2} - (1-Z)^{3/2}\Big)\Big(-\sqrt{1-Z^2}\cos\phi + 2D'(1-Z^2)\cos 2\phi\Big)
\end{aligned} \tag{B.38}$$

where we eliminated the superscript for simplicity and in the last step we used $\cos\phi\cos 2\phi + \sin\phi\sin 2\phi = \cos\phi$. Let us approximate $Z \cong 0$ and $\Delta\theta \cong 0$, so that

$$\begin{aligned}
\ddot{Z} &\cong -Z + (3D-B)Z - 2D^2Z + 2BDZ + C3Z(-1+2D) = \\
&= -Z\Big(1 + B + 3C - 3D - 2BD - 6CD + 2D^2\Big)
\end{aligned} \tag{B.39}$$

The adimensional expression for the small oscillations frequency is therefore

$$\omega_{I2M} = \sqrt{1 + \Lambda - D(3 + 2B - 6C + 2D)} \tag{B.40}$$

where $\Lambda = B + 3C$ as before. Putting $D = 0$, thus cancelling the higher order terms, we recover the Josephson frequency of the standard two-mode model Eq. (2.40).

C

2M-mode model: derivation of the Josephson equations

We have seen in subsection 3.2.4 that a supersolid can be modelled as a linear array of clusters, each of them with a localized wavefunction $\psi_j = \sqrt{N_j}\exp(i\theta_j)$ with population N_j and phase θ_j. The population-phase dynamics following a quench of these variables is described by the 2M-mode model written in Eq. (3.18)

$$\begin{aligned}
i\frac{\partial\psi_1}{\partial t} &= (E_1 + U_1N_1)\psi_1 - K_{12}\psi_2 \\
i\frac{\partial\psi_2}{\partial t} &= (E_2 + U_2N_2)\psi_2 - K_{12}\psi_1 - K_{23}\psi_3 \\
&\vdots \\
i\frac{\partial\psi_j}{\partial t} &= (E_j + U_jN_j)\psi_j - K_{j,j-1}\psi_{j-1} - K_{j,j+1}\psi_{j+1} \\
&\vdots \\
i\frac{\partial\psi_{2M}}{\partial t} &= (E_{2M} + U_{2M}N_{2M})\psi_{2M} - K_{2M,2M-1}\psi_{2M-1}
\end{aligned} \tag{C.1}$$

where U_j is the on-site interaction of the jth cluster and $K_{j,j-1}$ is the coupling coefficient between clusters j and $j-1$ [23, 27]. The terms E_j account for the energy offset of the jth cluster due to the external trapping [27], see Figure 3.1. Substituting the expression for the wavefunction inside the system Eq. (C.1) and dividing real and imaginary parts, we obtain 4M equations, 2M for the populations

and 2M for the phases. Let us start from the populations

$$\begin{aligned}
\dot{N}_1 &= -2K_{12}\sqrt{N_1N_2}\sin(\Delta\theta_{12}) \\
\dot{N}_2 &= 2K_{12}\sqrt{N_1N_2}\sin(\Delta\theta_{12}) - 2K_{23}\sqrt{N_2N_3}\sin(\Delta\theta_{23}) \\
&\vdots \\
\dot{N}_j &= 2K_{j,j-1}\sqrt{N_jN_{j-1}}\sin(\Delta\theta_{j,j-1}) - 2K_{j,j+1}\sqrt{N_jN_{j+1}}\sin(\Delta\theta_{j+1,j}) \\
&\vdots \\
\dot{N_{2M}} &= 2K_{2M,2M-1}\sqrt{N_{2M}N_{2M-1}}\sin(\Delta\theta_{2M,2M-1})
\end{aligned} \tag{C.2}$$

where we have defined $\Delta\theta_{i,j} \equiv \theta_j - \theta_i$. We can focus on the two central clusters M and $M+1$ by writing the dynamics of thier populations and by summing all the other populations on their left (from 1 to $M-1$) and on their right (from $M+1$ to $2M$)

$$\begin{aligned}
\sum_{j=1}^{M-1}\dot{N}_j &= -2K_{M,M-1}\sqrt{N_MN_{M-1}}\sin(\Delta\theta_{M,M-1}) \\
\dot{N_M} &= 2K_{M,M-1}\sqrt{N_MN_{M-1}}\sin(\Delta\theta_{M,M-1}) - 2K_{M+1,M}\sqrt{N_MN_{M+1}}\sin(\Delta\theta_{M+1,M}) \\
\dot{N_{M+1}} &= 2K_{M,M+1}\sqrt{N_MN_{M+1}}\sin(\Delta\theta_{M+1,M}) - 2K_{M+2,M+1}\sqrt{N_{M+1}N_{M+2}}\sin(\Delta\theta_{M+2,M+1}) \\
\sum_{j=M+1}^{2M}\dot{N}_j &= 2K_{M+2,M+1}\sqrt{N_{M+2}N_{M+1}}\sin(\Delta\theta_{M+2,M+1})
\end{aligned} \tag{C.3}$$

The population current between central clusters assume the form

$$\begin{aligned}
\dot{N_{M+1}} - \dot{N_M} &= 4K_{M+1,M}\sqrt{N_MN_{M+1}}\sin(\Delta\theta_{M+1,M}) \\
&\quad - 2K_{M+2,M+1}\sqrt{N_{M+2}N_{M+1}}\sin(\Delta\theta_{M+2,M+1}) \\
&\quad - 2K_{M,M-1}\sqrt{N_MN_{M-1}}\sin(\Delta\theta_{M,M-1}) \\
&= 4K_{M+1,M}\sqrt{N_MN_{M+1}}\sin(\Delta\theta_{M+1,M}) + \sum_{j=1}^{M-1}\dot{N}_j + \sum_{j=M+1}^{2M}\dot{N}_j
\end{aligned} \tag{C.4}$$

In order to isolate a single harmonic oscillation of the population and phase differences, we need to use the hypothesis Eq. (3.25)

$$\alpha = \left(\sum_{j=1}^{M-1}(-1)^{j-M+1}\frac{U_M}{U_j}\right)^{-1}. \tag{C.5}$$

Using this equality between currents, we rewrite Eq. (C.3) as

$$\dot{N_{M+1}} - \dot{N_M} = 4K_{M+1,M}\frac{\alpha}{\alpha-1}\sqrt{N_MN_{M+1}}\sin(\Delta\theta_{M+1,M}) \tag{C.6}$$

Defining the variable

$$z \equiv \frac{N_{M+1} - N_M}{N_{M+1} + N_M} \tag{C.7}$$

we finally derive the first Josephson equation

$$\dot{z} = 2K \frac{\alpha}{\alpha - 1} \sqrt{1 - z^2} \sin(\Delta\theta) \tag{C.8}$$

where we have defined, as in subsection 3.2.4, $K \equiv K_{M+1,M}$ and $\Delta\theta \equiv \theta_{M+1,M}$. To be noticed, that in order to derive this equation, we need the sum $N_M + N_{M+1}$ to be constant in time. It could seem counterintuitive thinking that the central clusters are not isolated, but it makes sense because we are asking the two clusters to have a Josephson oscillation between them, thus a symmetric exchange of atoms.
With regard to phases, the $2M$ equations assume the form

$$\begin{aligned} \dot{\theta_1} &= -(E_1 + U_1 N_1) \\ \dot{\theta_2} &= -(E_2 + U_2 N_2) \\ &\vdots \\ \dot{\theta_j} &= -(E_j + U_j N_j) \\ &\vdots \end{aligned} \tag{C.9}$$

Being in a symmetric system, we recall that we have the conditions

$$E_{j>M} = E_{2M-(j-1)} \qquad U_{j>M} = U_{2M-(j-1)} \tag{C.10}$$

Thus, the central phase difference $\Delta\theta \equiv \theta_{M+1} - \theta_M$ evolves as

$$\dot{\Delta\theta} = -U(N_{M+1} - N_M) \tag{C.11}$$

where we have defined, as in subsection 3.2.4, $U \equiv U_M$. As a function of z, we have

$$\dot{\Delta\theta} = -U(N_{M+1} + N_M)z \tag{C.12}$$

that is exactly the Eq. (3.22).

D

Ansatz: derivation of Josephson frequency and critical imbalance

In this appendix we are going to start deriving Eq. (3.24) and Eq. (3.25). Let us recall the oscillations ansatz

$$\begin{aligned} N_j(t) &= N_j^0 + (-1)^{j+1}\Delta_j \sin(\omega_J t) \\ \Delta\theta_{j+1,j}(t) &= (-1)^j \delta\phi \cos(\omega_J t) \end{aligned} \tag{D.1}$$

and their derivatives

$$\begin{aligned} \dot{N}_j(t) &= (-1)^{j+1}\Delta_j \omega_J \cos(\omega_J t) \\ \dot{\Delta\theta}_{j+1,j}(t) &= (-1)^{j+1}\delta\phi\omega_J \sin(\omega_J t) \end{aligned} \tag{D.2}$$

We need to insert these expressions inside the evolution equations Eq. (C.2) and Eq. (C.9). Let us start from the phases Eq. (C.9)

$$\dot{\Delta\theta}_{j+1,j}(t) = (-1)^{j+1}\delta\phi\omega_J \sin(\omega_J t) = -(E_{j+1} - E_j) - (U_{j+1}N_{j+1} - U_j N_j) \tag{D.3}$$

The energy offsets E_j can be found in the equilibrium condition

$$\begin{aligned} \dot{\theta}_j(t) = 0 &= -E_j - U_j N_j^0 \\ E_j &= U_j N_j^0 \end{aligned} \tag{D.4}$$

where N_j^0 is the equilibrium population. Thus we can write

$$\begin{gathered}(-1)^{j+1}\delta\phi\omega_J \sin(\omega_J t) = -(U_{j+1}N_{j+1}^0 - U_j N_j^0) - [U_{j+1}(N_{j+1}^0 + (-1)^{j+2}\Delta_j \sin(\omega_J t)) \\ -U_j(N_j^0 + (-1)^{j+1}\Delta_j \sin(\omega_J t))] \\ \delta\phi\ \omega_J = U_j\Delta_j + U_{j+1}\Delta_{j+1}\end{gathered} \tag{D.5}$$

In the special case $j = M$, we have equal interactions and equal amplitudes of the population oscillations

$$\begin{gathered}\delta\phi\ \omega_J = U_M\Delta_M + U_{M+1}\Delta_{M+1} = 2U_M\Delta_M = 2U_{M+1}\Delta_{M+1} \\ U_M\Delta_M = U_{M+1}\Delta_{M+1}\end{gathered} \tag{D.6}$$

In the subsequent case $j = M + 1$, we have

$$\begin{gathered}\delta\phi\ \omega_J = U_{M+1}\Delta_{M+1} + U_{M+2}\Delta_{M+2} = 2U_{M+1}\Delta_{M+1} \\ U_{M+2}\Delta_{M+2} = U_{M+1}\Delta_{M+1}\end{gathered} \tag{D.7}$$

so that we can ricursively say

$$U_j\Delta_j = U_{j+1}\Delta_{j+1} \qquad \forall j \tag{D.8}$$

and

$$\frac{\delta\phi\ \omega_J}{2} = U_j\Delta_j \qquad \forall j \tag{D.9}$$

Let us pass to the population evlution Eq. (C.2) in the limit of small phase and population imbalances

$$\begin{gathered}\dot{N}_j(t) = (-1)^{j+1}\Delta_j\omega_J \cos(\omega_J t) = \\ = 2K_{j,j-1}\sqrt{N_j^0 N_{j-1}^0}(\Delta\theta_{j,j-1}) - 2K_{j,j+1}\sqrt{N_j^0 N_{j+1}^0}(\Delta\theta_{j+1,j}) = \\ = 2K_{j,j-1}\sqrt{N_j^0 N_{j-1}^0}(-1)^{j-1}\delta\phi\cos(\omega_J t) - 2K_{j,j+1}\sqrt{N_j^0 N_{j+1}^0}(-1)^j\delta\phi\cos(\omega_J t)\end{gathered} \tag{D.10}$$

so that

$$-\Delta_j\omega_J = \left(2K_{j,j-1}\sqrt{N_j^0 N_{j-1}^0} + 2K_{j,j+1}\sqrt{N_j^0 N_{j+1}^0}\right)\delta\phi \tag{D.11}$$

Using Eq. (D.9) to cancel Δ_j and $\delta\phi$ from the equality, we obtain an expression for the Josephson frequency

$$\omega_J^2 = 4K_{j,j-1}U_j\sqrt{N_j^0 N_{j-1}^0} + 4K_{j,j+1}U_j\sqrt{N_j^0 N_{j+1}^0} \tag{D.12}$$

Starting from $\dot{N}_1$ instead of $\dot{N}_j$ and following the same procedure, we obtain another expression for the Josephson frequency

$$\omega_j^2 = 4K_{12}U_1\sqrt{N_1N_2} \tag{D.13}$$

Equating the two expressions for the frequencies Eq. (D.13) and Eq. (D.12) in the case $j = 2$, we obtain the first condition on the parameters

$$\frac{U_1}{U_2} = 1 + \frac{K_{23}}{K_{12}}\sqrt{\frac{N_3^0}{N_1^0}} \tag{D.14}$$

In order to derive the second condition, we equalise ω_J obtained starting by $\dot{N}_j$ and the one starting from $\dot{N_{j+1}}$

$$\begin{aligned} &4K_{j,j-1}U_j\sqrt{N_j^0N_{j-1}^0} + 4K_{j,j+1}U_j\sqrt{N_j^0N_{j+1}^0} = \\ &= 4K_{j+1,j}U_{j+1}\sqrt{N_{j+1}^0N_j^0} + 4K_{j+1,j+2}U_{j+1}\sqrt{N_{j+1}^0N_{j+2}^0} \\ &\frac{U_j}{U_{j+1}} = \frac{4K_{j,j-1}\sqrt{N_j^0N_{j-1}^0} + 4K_{j,j+1}\sqrt{N_j^0N_{j+1}^0}}{4K_{j+1,j}\sqrt{N_{j+1}^0N_j^0} + 4K_{j+1,j+2}} \end{aligned} \tag{D.15}$$

so that with few math we obtain the second condition in Eq. (3.24)

$$\frac{U_j}{U_{j+1}} = \frac{1 + \frac{K_{j+1,j+2}}{K_{j,j-1}}\sqrt{\frac{N_{j+2}^0}{N_j^0}}}{1 + \frac{K_{j,j-1}}{K_{j,j+1}}\sqrt{\frac{N_{j-1}^0}{N_{j+1}^0}}}, \quad \forall j. \tag{D.16}$$

Having these conditions on the parameters, we can also derive an expression of the α coefficient that appears in our hypothesis Eq. (3.21). Let us start imposing the conservation of the total atom number in the system $N_{tot} = \sum_{j=1}^{2M} N_j$, so that

$$\sum_{j=1}^{M-1}\dot{N}_j + \dot{N}_M + \dot{N_{M+1}} + \sum_{j=M+2}^{2M}\dot{N}_j = 0 \tag{D.17}$$

We can rewrite Eq. (3.21) as

$$\dot{N}_{M+1} - \dot{N}_M = \alpha\left(2\sum_{j=1}^{M-1}\dot{N}_j + \dot{N}_M + \dot{N_{M+1}}\right) \tag{D.18}$$

$$\dot{N}_{M+1}(1-\alpha) - \dot{N}_M(1+\alpha) = 2\alpha\sum_{j=1}^{M-1}\dot{N}_j \tag{D.19}$$

By substituting Eq. (D.1) inside Eq. (D.19), we have

$$(-1)^{M+2}\Delta_{M+1}\omega_J\cos(\omega_J t)(1-\alpha)-(-1)^{M+1}\Delta_M\omega_J\cos(\omega_J t)(1+\alpha)= 2\alpha\sum_{j=1}^{M-1}(-1)^{j+1}\Delta_j\omega_J\cos(\omega_J t) \tag{D.20}$$

that recalling $\Delta_M=\Delta_{M+1}$ becomes

$$\alpha=\left(\sum_{j=1}^{M-1}(-1)^{j-M+1}\frac{\Delta_j}{\Delta_M}\right)^{-1} \tag{D.21}$$

At this point, we can use Eq. (D.8) to remove the Δs. In order to do that, we can look for a recursively equality. We know that

$$\frac{U_j}{U_{j+1}}=\frac{\Delta_{j+1}}{\Delta_j} \tag{D.22}$$

that for $j=M-1$ is

$$\frac{U_{M-1}}{U_M}=\frac{\Delta_M}{\Delta_{M-1}} \tag{D.23}$$

Multiplying on both sides by the equality Eq. (D.22) for $j=M-2$, we have

$$\frac{U_{M-2}}{\cancel{U_{M-1}}}\frac{\cancel{U_{M-1}}}{U_M}=\frac{\Delta_M}{\cancel{\Delta_{M-1}}}\frac{\cancel{\Delta_{M-1}}}{\Delta_{M-2}} \tag{D.24}$$

and we can reiterate this multiplication diminuishing the index until 1, so that

$$\frac{U_j}{U_M}=\frac{\Delta_M}{\Delta_j}\qquad\forall j\leq M \tag{D.25}$$

Finally, we can use this relation to write α as a function only of the parameters of the system, as Eq. (3.25)

$$\alpha=\left(\sum_{j=1}^{M-1}(-1)^{j-M+1}\frac{U_M}{U_j}\right)^{-1} \tag{D.26}$$

Starting from the Josephson system Eq. (3.22), we can now derive both Josephson frequency ω_J and the critical population imbalance z_c marking the transition to the MQST as a function of the parameters of the system. To derive ω_J, we perform the second derivative of z

$$\ddot{z}\cong 2K\frac{\alpha}{\alpha-1}\dot{\Delta\theta}=2K\frac{\alpha}{\alpha-1}U(N_M+N_{M+1})z \tag{D.27}$$

and we have immediately the expression

$$\omega_J = \sqrt{2K\frac{\alpha}{\alpha-1}U(N_M + N_{M+1})} \tag{D.28}$$

A procedure to derive z_c is the one resembling the search for the separatrix in the pendulum phase space. Considering z and $\Delta\theta$ as conjugate variables

$$\dot{z} = -\frac{\partial H}{\partial \Delta\theta} \qquad \dot{\Delta\theta} = \frac{\partial H}{\partial z} \tag{D.29}$$

we have the hamiltonian

$$H = U(N_M + N_{M+1})\frac{z^2}{2} - 2K\frac{\alpha}{\alpha-1}\sqrt{1-z^2}\cos(\Delta\theta) \tag{D.30}$$

This is the hamiltonian of a simple pendulum. The energy of the separatrix can be found by maximizing over $\Delta\theta$ on the axis $z = 0$

$$H_0 \equiv \max_{\Delta\theta}(H(z=0), \Delta\theta) = \max_{\Delta\theta}\left(2K\frac{\alpha}{\alpha-1}\cos(\Delta\theta)\right) = 2K\frac{\alpha}{\alpha-1} \tag{D.31}$$

We need to calculate $H > H_0$, but on the axis $\Delta\theta = 0$ in order to find out z_c

$$H(z, \Delta\theta = 0) = U(N_M + N_{M+1})\frac{z^2}{2} - 2K\frac{\alpha}{\alpha-1}\sqrt{1-z^2} = H_0 = 2K\frac{\alpha}{\alpha-1} \tag{D.32}$$

Doing some math in the limit of weak coupling, thus neglecting terms of order K^2, we obtain

$$z^2 > \frac{8K\alpha/(\alpha-1)}{U(N_M + N_{M+1})} \equiv z_c^2 \tag{D.33}$$

so that the critical imbalance z_c is exactly the one in Eq. (3.27).

E

Numerical methods for dipolar supersolid

Runge-Kutta integration methods

The differential equation Eq. (3.29) is an ordinary differential equation (ODE) in time of the type:

$$\frac{dy}{dt} = f(y,t) \qquad y(t_0) = y_0 \tag{E.1}$$

where y is the unknown function of t, whose evolution is described by the function f that depends both on t and y itself, while y_0 is the initial condition. Actually, since we will then use the ITP method, the initial condition is not important, in fact in principle we could choose it at random.
We have solved the Eq. (E.1) using the 4th order Runge-Kutta method. In general, the Runge-Kutta methods, developed around 1900 by the German mathematicians Carl Runge [220] and Wilhelm Kutta [221], are numerical iterative methods to solve ODEs. They essentially propagate a solution over an interval by combining the information from several Euler-style steps (each involving one evaluation of the right-hand f's), and then use the information obtained to match a Taylor series expansion up to some higher order. To understand it better, let us start from the Euler method:

$$y_{n+1} = y_n + hf(t_n, y_n) \tag{E.2}$$

where h is the time step and n is the index that run over time. This method advances the solution from y_n to y_{n+1} asymmetrically because it uses derivative information only at the beginning of the interval h. This method is the easiest, but it is not that accurate and is also unstable.

One way to improve it might be to do a half step test and calculate the derivative there to better understand the true derivative of the total step. This is the second-order Runge-Kutta (RK2) method:

$$\begin{cases} k_1 = hf(t_n, y_n) \\ k_2 = hf\left(t_n + \frac{1}{2}h, y_n + \frac{1}{2}k_1\right) \\ y_{n+1} = y_n + (k_1 + k_2)/2 + O(h^3) \end{cases} \tag{E.3}$$

Proof The first step to demonstrate the explicit expression of RK2 is writing down the Taylor series expansion of y in the neighborhood of t_n correct to the h^2 term:

$$y(t_{n+1}) = y(t_n) + h\frac{dy}{dt}\bigg|_{t_n} + \frac{h^2}{2}\frac{d^2y}{dt^2}\bigg|_{t_n} + O(h^3) \tag{E.4}$$

The first derivative of y is simply given by f, but the second one written only in

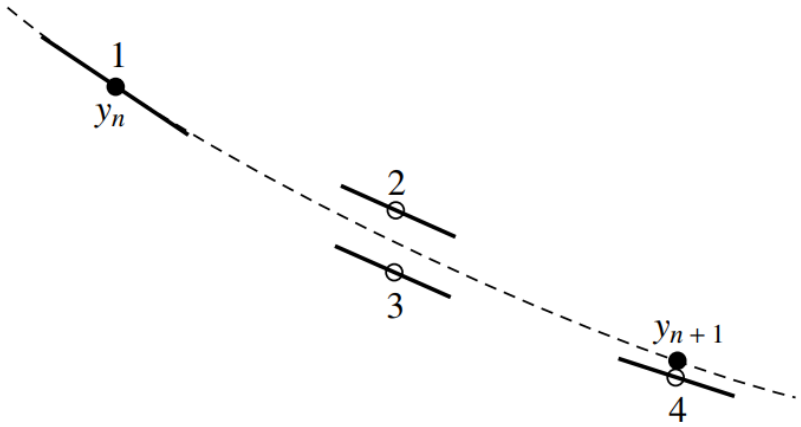

Figure E.1: Fourth-order Runge-Kutta method. In each step the derivative is evaluated four times: once at the initial point, twice at trial midpoints, and once at a trial endpoint. From these derivatives the final function value (shown as a filled dot) is calculated.

terms of f is given by:

$$\left.\frac{d^2y}{dt^2}\right|_{t_n} = \frac{d}{dt}f(y_n,t_n) = \frac{\partial f}{\partial t} + \frac{\partial f}{\partial y}\frac{dy}{dt} = \frac{\partial f}{\partial t} + \frac{\partial f}{\partial y}f \tag{E.5}$$

Substituting these derivatives in E.4, y has the expansion:

$$y(t_{n+1}) = y(t_n) + hf(y_n,t_n) + \frac{h^2}{2}\left[\frac{\partial f}{\partial t} + \frac{\partial f}{\partial y}f\right]\Big|_{t_n} + O(h^3) \tag{E.6}$$

On the other side, y can also be written as the result of two derivatives with generic steps and generic weights:

$$\begin{cases} k_1 = hf(t_n,y_n) \\ k_2 = hf\big(t_n+\alpha h, y_n+\beta k_1\big) \\ y_{n+1} = y_n + ak_1 + bk_2 + O(h^3) \end{cases} \tag{E.7}$$

It is notable that the case with $k_2 = 0$ and $a = 1$ returns exactly the Euler method. The next step consists in writing down y_{n+1} with the explicit Taylor serie expansion of k_2:

$$\begin{aligned} y_{n+1} &= y_n + ahf(t_n,y_n) + bh\left[f(y_n,t_n) + \alpha h\frac{\partial f}{\partial t}\Big|_{t_n} + \beta hf(y_n,t_n)\frac{\partial f}{\partial y}\Big|_{t_n}\right] + O(h^3) = \\ &= y_n + h(a+b)f(t_n,y_n) + \frac{h^2}{2}\left[2\alpha b\frac{\partial f}{\partial t}\Big|_{t_n} + 2\beta bf(y_n,t_n)\frac{\partial f}{\partial y}\Big|_{t_n}\right] + O(h^3) \end{aligned} \tag{E.8}$$

The comparison between (E.6) and (E.8) establishes the conditions for the coefficients:

$$\begin{cases} a+b=1 \\ 2\alpha b = 1 \\ 2\beta b = 1 \end{cases} \quad\Longrightarrow\quad \begin{cases} a = 1-b \\ \alpha = \beta = \dfrac{1}{2b} \end{cases} \tag{E.9}$$

In agreement with the fact that there are three equations and four coefficients, there is an arbitrariness, i.e. there are infinitely many possible choices of α, β, a, b which satisfy the above conditions. The choice with which we get the classical RK2 method is:

$$\begin{aligned} \alpha = \beta = 1 \\ a = b = 1/2 \end{aligned} \tag{E.10}$$

that lead exactly to (E.7).

$\mathcal{Q}.\mathcal{E}.\mathcal{D}.$

The simmetrization of the step has allowed us to gain an order of accuracy. Calculating the right hand side f with higher order coefficients, accuracy increases but the Runge-Kutta method becomes more and more complicated. The most used one is the fourth-order Runge-Kutta method:

$$\begin{cases} k_1 = hf(t_n, y_n) \\ k_2 = hf\left(t_n + \frac{1}{2}h, y_n + \frac{1}{2}k_1\right) \\ k_3 = hf\left(t_n + \frac{1}{2}h, y_n + \frac{1}{2}k_2\right) \\ k_4 = hf\left(t_n + h, y_n + k_3\right) \\ y_{n+1} = y_n + \frac{1}{6}k_1 + \frac{1}{3}k_2 + \frac{1}{3}k_3 + \frac{1}{6}k_4 + O(h^5) \end{cases} \tag{E.11}$$

This is the best compromise between precision and complexity, therefore time needed to run it.

As showed in Figure E.1, this method calculates the derivative twice at the midpoint of the interval and once at the endpoint. In fact, k_1 is the standard Euler's method increment, k_2 is the midpoint increment using k_1 for y, k_3 is still the increment at the midpoint but using k_2 for y and k_4 is the total increment at the endpoint. The final calculation of y is a weighted mean of these four steps, so that the midpoints increments have a greater weight.

Discretization

The application of these numerical methods requires the discretization of the right-hand side function f in Eq. (E.1), that in our case is the action of the hamiltonian over the wave function ψ. The first step is defining a space grid:

$$\begin{aligned} x &= -L_x : dx : L_x \\ y &= -L_y : dy : L_y \\ z &= -L_z : dz : L_z; \end{aligned} \tag{E.12}$$

i.e. a vector x starting from $-L_x$ and ending at L_x with a step equal to dx, and the same for y and z. The steps are defined using the number of them N_i in the corresponding direction:

$$dx_i = \frac{2L_i}{N_i - 1} \qquad i = x, y, z \tag{E.13}$$

with $N_x = 128$, $N_y = N_z = 64$. Notice that we have chosen numbers of points that are powers of two because it will be useful for the use of the Fast Fourier Transform (FFT), as we will need. Another necessary thing to do for FFT is to define another grid in momentum space

$$k_i = -\frac{N_i}{2}dk_i : dk_i : \frac{N_i}{2}dk_i \tag{E.14}$$

with the momentum steps defined with respect to the real space grid length

$$dk_i = \frac{\pi}{2L_i} \tag{E.15}$$

so that the k_i vectors are the same length of the corresponding x_i vectors. Now, we can discretize the hamiltonian.

The first term is the kinetic one, so, unless a numerical pre-factor, it essentially is the 3D laplacian:

$$\nabla^2 = \frac{\partial^2}{\partial x^2} + \frac{\partial^2}{\partial y^2} + \frac{\partial^2}{\partial z^2} \tag{E.16}$$

that can be written on the discrete grid using finite differences at different orders. We have used the finite difference 5-point formula:

$$\frac{\partial^2 f}{\partial x^2} = \frac{-f(x-2dx) + 16f(x-dx) - 30f(x) + 16f(x+dx) - f(x+2dx)}{12dx^2} \tag{E.17}$$

in all three directions.

The external harmonic potential is easy because it explicitly contains the space vectors x_i:

$$V(x,y,z) = \frac{1}{2}m(\omega_x^2 x^2 + \omega_y^2 y^2 + \omega_z^2 z^2) \tag{E.18}$$

with the mass $m \cong 161.9268u$ of the ^{162}Dy, where u is the atomic mass $u = 1.67 \cdot 10^{-27} Kg$ and the frequencies are the ones used by [16]:

$$\omega = 2\pi(18.5, 53, 81) \text{ Hz} \tag{E.19}$$

From these frequencies derive the natural length scales:

$$a^i_{h.o.} = \sqrt{\frac{\hbar}{m\omega_i}} \tag{E.20}$$

which are the widths of the Gaussian solutions of the quantum harmonic oscillator. Fixed the external potential, we also have a good reasonable choice for the starting wave function:

$$\phi(\mathbf{r}, 0) = \left(\frac{m}{\pi\hbar}\right)^{3/4} (\omega_x\omega_y\omega_z)^{1/4} e^{-\frac{1}{4}\left(\frac{x^2}{a_x^2} + \frac{y^2}{a_y^2} + \frac{z^2}{a_z^2}\right)} \tag{E.21}$$

i.e. the harmonic oscillator solutions.
The LHY term contains the integral $F(\epsilon_{dd})$ that cannot be evaluated analitically, so we numerically integrated it in the code.
The dipolar term is described in subsection 3.3.3.

F

Fourier transform of dipolar interaction

Consider the dipole-dipole interaction Eq. (1.77):

$$V_{dd}(\mathbf{r}) = \frac{C_{dd}}{4\pi}\frac{1-3\cos^2\beta}{r^3} \tag{F.1}$$

where β is the angle between the $\mathbf{r}$ vector connecting the two dipoles and the direction $\hat{d}$ where they point. Its Fourier transform is defined as:

$$\tilde{V}_{dd}(\mathbf{k}) = \int d\mathbf{r} V_{dd}(\mathbf{r}) e^{-i\mathbf{k}\cdot\mathbf{r}} \tag{F.2}$$

Let us choose spherical coordinates and the direction of $\mathbf{k}$ along the z-axis this time, as shown in Figure F.1.

In particular, we can choose the dipole vector to be in the $y-z$ plan:

$$\mathbf{d} = d\ (\sin\alpha\ \hat{y} + \cos\alpha\ \hat{z}) \tag{F.3}$$

and then the $\mathbf{r}$ vector must point in a generic direction:

$$\mathbf{r} = r\ (\sin\theta\cos\phi\ \hat{x} + \sin\theta\sin\phi\ \hat{y} + \cos\theta\ \hat{z}) \tag{F.4}$$

The Eq. (F.2) in these special coordinates becomes:

$$\tilde{V}_{dd}(\mathbf{k}) = \int_0^{2\pi} d\phi \int_0^{\pi} d\theta \sin\theta \int_b^{+\infty} dr\ r^2 \frac{C_{dd}}{4\pi}\frac{1-3\cos^2\beta}{r^3} e^{-ikr\cos\theta} \tag{F.5}$$

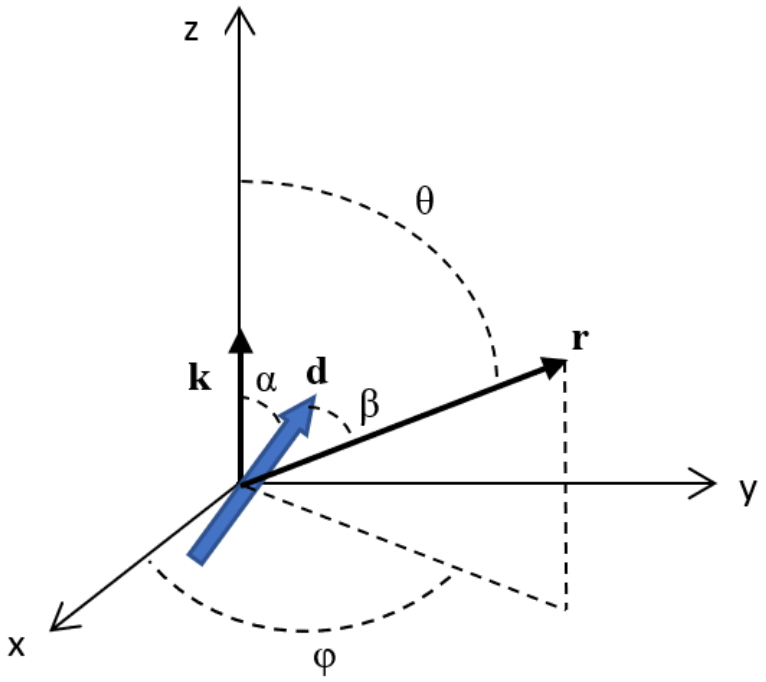

Figure F.1: Representation of the coordinate system used in the analytical calculation of the Fourier transform of the dipolar interaction. The z-axes is oriented along the **k** vector, the y-axes is so that the dipoles orientation is in the $y-z$ plan, while the vector **r** that unites two dipoles is in a generic direction. The coordinates are spherical and the angles are all indicated in the figure.

where we have introduced b, a cut-off in r to avoid divergences. The last step in this calculation will be the limit $b \to 0$ to restore the right solution.

The cosine function of beta can be reformulated in terms of ϕ and θ integration angles:

$$\cos\beta = \frac{\mathbf{d}\cdot\mathbf{r}}{|\mathbf{d}||\mathbf{r}|} = \sin\alpha\ \sin\phi\ \sin\theta\ + \cos\alpha\ \cos\theta \tag{F.6}$$

so that the integral in ϕ can be evaluated:

$$\begin{aligned}\int_0^{2\pi} d\phi(1-3\cos^2\beta) = \int_0^{2\pi} d\phi(1-3(\sin\alpha\ \sin\phi\ \sin\theta\ + \cos\alpha\ \cos\theta)^2) = \\ = \int_0^{2\pi} d\phi(1-3\sin^2\alpha\sin^2\phi\sin^2\theta - 3\cos^2\alpha\cos^2\theta - 6\sin\alpha\cos\alpha\sin\theta\cos\theta\sin\phi) = \\ = 2\pi - 3\pi\ \sin^2\alpha\ \sin^2\theta - 6\pi\ \cos^2\alpha\ \cos^2\alpha\end{aligned} \tag{F.7}$$

Then, the integral in θ in Eq. (F.5) involves also the exponential factor:

$$\int_0^\pi d\theta \sin\theta \ (2\pi - 3\pi \ \sin^2\alpha \ \sin^2\theta - 6\pi \ \cos^2\alpha \ \cos^2\alpha) \ e^{-ikr\cos\theta} \tag{F.8}$$

that, with the substitutions $x = \cos\theta$ and $u = kr$, becomes:

$$\begin{aligned}
&\int_{-1}^{1} dx \ (2\pi - 3\pi\sin^2\alpha(1-x^2) - 6\pi\cos^2\alpha x^2) \ e^{-iux} = \\
&= \pi \int_{-1}^{1} dx \ (2 - 3(1-x^2) + 3\cos^2\alpha(1-x^2) - 6\cos^2\alpha x^2) \ e^{-iux} = \\
&= \pi \int_{-1}^{1} dx \ (-1 + 3x^2 + 3\cos^2\alpha(1-3x^2)) \ e^{-iux} = \\
&= \pi(3\cos^2\alpha - 1) \int_{-1}^{1} dx(1-3x^2) \ e^{-iux} = \\
&= \pi(3\cos^2\alpha - 1)\left[2 \ \frac{\sin u}{u} - 3 \ \frac{2((u^2-2)\sin u + 2u\cos u)}{u^3}\right] = \\
&= -4\pi(3\cos^2\alpha - 1)\left[\frac{\sin u}{u} + 3 \ \frac{\cos u}{u^2} - 3 \ \frac{\sin u}{u^3}\right]
\end{aligned} \tag{F.9}$$

The only integral left is the one in $u = kr$, but the three addendums in the expression Eq. (F.9), taken individually, diverge. Writing the whole Fourier transform at this point:

$$\tilde{V}_{dd}(\mathbf{k}) = C_{dd}(1 - 3\cos^2\alpha) \int_{kb}^{+\infty} du \left[\frac{\sin u}{u^2} + 3 \ \frac{\cos u}{u^3} - 3 \ \frac{\sin u}{u^4}\right] \tag{F.10}$$

we can notice that, using integration by parts, some terms eliminates. In fact, the trick to eliminate these divergences consists in evaluating them together, because they balance each other out. So, let us start writing the first addendum in the integral Eq. (F.10):

$$\int_{kb}^{+\infty} \frac{\sin u}{u^2} = -\frac{\cos u}{u^2}\bigg|_{kb}^{+\infty} - 2\int_{kb}^{+\infty} \frac{\cos u}{u^3} \tag{F.11}$$

The first term evaluated in $+\infty$ goes to zero, but in the other extreme remains. The second one can add to the second term of Eq. (F.10), giving:

$$\int_{kb}^{+\infty} \frac{\cos u}{u^3} = \frac{\sin u}{u^3}\bigg|_{kb}^{+\infty} + 3\int_{kb}^{+\infty} \frac{\sin u}{u^4} \tag{F.12}$$

As before, the first term evaluated in $+\infty$ goes to zero, but in kb remains. The second term exactly cancel out the last term in Eq. (F.10). Finally, we have:

$$\tilde{V}_{dd}(\mathbf{k}) = C_{dd}(1 - 3\cos^2\alpha)\left[\frac{\cos(kb)}{(kb)^2} - \frac{\sin(kb)}{(kb)^3}\right] \tag{F.13}$$

The last thing left to do is the limit:

$$\begin{aligned} &\lim_{b\to 0} \frac{\cos(kb)}{(kb)^2} - \frac{\sin(kb)}{(kb)^3} = \\ &= \lim_{b\to 0} \frac{1}{(kb)^3}\left((kb)\left(\cancel{1} - \frac{(kb)^2}{2}\right) - \left(\cancel{(kb)} - \frac{(kb)^3}{6}\right)\right) = -\frac{1}{3} \end{aligned} \tag{F.14}$$

that, as expected, assumes a finite value.

The Fourier transform of the dipolar interaction is at last:

$$\tilde{V}_{dd}(\mathbf{k}) = \frac{C_{dd}}{3}(3\cos^2\alpha - 1) \tag{F.15}$$

G

Numerical methods of the JJN

We discuss here numerical methods used to obtain the results discussed in the main text.

1D GPE. The 1D simulations shown in Figure 5.1 and 5.2 refer to static solutions of the GPE equation:

$$\tilde{\mu} f(\theta) = \left(-\frac{1}{2}\frac{\partial^2}{\partial\theta^2} - \frac{1}{2}\frac{\tilde{J}^2}{\rho(\theta)^2} + \tilde{V}(\theta) + \tilde{g}\rho(\theta) \right) f(\theta), \tag{G.1}$$

where $f(\theta) = \sqrt{\rho(\theta)}$, $\tilde{J} = 2\pi(w - \tilde{\Omega})/\int_0^{2\pi} d\theta/\rho(\theta)$ and $\tilde{\Omega} = \Omega/J_R$. Here energies are rescaled in units of $\hbar^2/(mR^2)$, $\tilde{\mu}$ is the rescaled chemical potential, $\tilde{g}$ is the interaction strength, $\tilde{V}(\theta) = \tilde{V}_0 \sum_{j=1}^{n} \exp[-2(\theta - \theta_j)^2/\sigma^2]$ is the sum of Gaussian barriers centered at $\theta_j = 2\pi j/n$, and θ is the azimuthal angle along the ring. The free parameters $\tilde{g}$, σ and $\tilde{V}_0$ are chosen in order to match the experimental conditions: $\sigma/\xi = 1.2$, $\tilde{V}_0/\tilde{\mu}_0 = 1.4$ and $\xi/R = 0.056$ (with $R = 12$ μm being approximately the inner radius of the experimental system), where μ_0 is the chemical potential obtained in the homogeneous case (without barriers) and for $w = \Omega = 0$. For a given number of barriers, the solution of Eq. (G.1) is obtained by imaginary time evolution.

2D GPE We have performed 2D numerical simulations, assuming a Gaussian distribution of the BEC along the z-direction, perpendicular to the $x - y$ plane where the current is generated, and integrating along the z-direction. This was

made possible solely by the presence of a harmonic trapping potential in the z-direction. We have integrated the following equation

$$i\hbar\frac{\partial\psi(x,y,t)}{\partial t} = \left(-\frac{\hbar^2}{2M}\nabla^2_{x,y} + V(x,y) + g^{2D}|\psi(\mathbf{r},t)|^2\right)\psi(x,y,t) \tag{G.2}$$

where $\nabla^2_{x,y} = \partial^2/\partial x^2 + \partial^2/\partial y^2$ and $g^{2D} = 2\sqrt{2\pi}a_s N/\sigma_z$, with σ_z being the harmonic length $\sigma_z = \sqrt{\hbar/(m\omega_x)}$ and the other parameters explained below in the 3D section. We have found the ground states by solving the Eq. (G.2) using an imaginary propagation technique with barriers. We then performed a phase imprinting with a finite winding w_0 and allowed the system to evolve in real time. The results are in agreement with the 3D numerical simulations which could be directly compared with the experimental data. These simulations enabled us to explore various regimes in a shorter time and perform 3D simulations in targeted regimes.

3D GPE. In order to better capture the experimental procedure and the dynamics of the system, in 3D we solve numerically the time-dependent GPE for static barriers,

$$i\hbar\frac{\partial\psi(\mathbf{r},t)}{\partial t} = \left(-\frac{\hbar^2}{2M}\nabla^2 + V(\boldsymbol{r}) + g|\psi(\mathbf{r},t)|^2\right)\psi(\mathbf{r},t), \tag{G.3}$$

with $\psi(\mathbf{r},t)$ being the condensate order parameter, M the molecule mass, $g = 4\pi\hbar^2 a/M$ the interaction strength, $a = 1010\,a_0$ the s-wave scattering length and a_0 the Bohr radius. The external trapping potential is $V(\boldsymbol{r}) = V_{\text{harm}}(\boldsymbol{r}) + V_{\text{ring}}(\boldsymbol{r}) + V_{\text{barr}}(\boldsymbol{r})$. Here, $V_{\text{harm}}(\boldsymbol{r}) = M(\omega_\perp^2 r^2 + \omega_z^2 z^2)/2$ is an harmonic confinement with $\{\omega_\perp, \omega_z\} = 2\pi \times \{2.5\,, 396\}$ Hz. The hard-wall potential creating the ring confinement in the x-y plane is given by

$$V_{\text{ring}}(\boldsymbol{r}) = V_r\left[\tanh\left(\frac{r - R_{out}}{d}\right) + 1\right] + V_r\left[\tanh\left(\frac{R_{\text{in}} - r}{d}\right) + 1\right]. \tag{G.4}$$

with $R_{in} = 10.09\,\mu$m and $R_{out} = 21.82\,\mu$m being the inner and outer radius, respectively. The parameter $d = 1.1\,\mu$m characterizes the stiffness of the hard walls, fixed such that the numerical density profiles match the in-situ experimental ones. We take V_r larger than the chemical potential μ such that the density goes to zero at the boundary. The n barriers are modelled as identical Gaussian peaks of trapping potential

$$V_{\text{barr}} = V_0\sum_{i=1}^{n/2}\exp\left[-2(x\cos(i2\pi/n) + y\sin(i2\pi/n))^2/\sigma^2\right]. \tag{G.5}$$

with constant width $\sigma = 0.8\,\mu$m. We first find the system ground state by solving the GPE by imaginary time evolution and in the presence of n barriers. We then instantaneously imprint a current of winding w_0 by multiplying the ground state wavefunction by the phase factor $\exp(-i2\pi w_0\theta)$, where θ is the azimuthal angle. We finally study the system dynamics by solving the time-dependent GPE. For a particle number $N = 6.8 \times 10^3$ (corresponding to the experimental condensate number), we obtain $\mu = 1.09$ kHz leading to a value of the healing length $\xi = 0.59\,\mu$m. Equation G.3 is solved numerically by the Fourier split-step method on a Cartesian grid of $\{N_x, N_y, N_z\} = \{256, 256, 80\}$ points dividing a grid size of length $-34.846\,\mu\text{m} \leq r \leq 34.846\,\mu\text{m}$ and $-11.0\,\mu\text{m} \leq z \leq 11.0\,\mu$m in the radial plane and axial direction, respectively. The time step is set to $\Delta t = 1 \times 10^{-5}\,\omega_\perp^{-1}$.

Bibliography

[1] L. D. Broglie. *Recherches sur la théorie des Quanta*. Annales de Physique **10**, 22 (1925). (pages 1 and 5).

[2] S. N. Bose. *Plancks Gesetz und Lichtquantenhypothese*. Zeitschrift fur Physik **26**, 178 (1924). (pages 1 and 6).

[3] A. Einstein. *Quantentheorie des einatomigen idealen Gases*. Sitzungsberichte der Preussischen Akademie der Wissenschaften **22**, 237 (1924). (page 6).

[4] A. Einstein. *Quantentheorie des einatomigen idealen Gases, Zweite Abhandlung*. Sitzungsberichte der Preussischen Akademie der Wissenschaften **1**, 245 (1925). (pages 1 and 6).

[5] F. Dalfovo, S. Giorgini, L. P. Pitaevskii and S. Stringari. *Theory of Bose-Einstein condensation in trapped gases*. Rev. Mod. Phys. **71**, 463 (1999). (pages 1 and 18).

[6] L. P. Pitaevskiĭ and S. Stringari. *Bose-Einstein condensation and superfluidity*. Number 164 in International series of monographs on physics. Oxford University Press, Oxford, United Kingdom, first edition edition (2016), oCLC: ocn919186901. (pages 6, 7, 8, 12, and 47).

[7] C. Pethick and H. Smith. *Bose-Einstein condensation in dilute gases*. Cambridge university press, Cambridge, 2nd ed edition (2008). (pages 1, 8, 9, and 18).

[8] M. Inguscio and L. Fallani. *Atomic physics: precise measurements and ultracold matter*. Oxford University Press, Oxford, 1st ed edition (2013), oCLC: ocn853505673. (pages 1, 7, and 48).

[9] C. Cohen-Tannoudji and D. Guéry-Odelin. *Advances in atomic physics: an overview*. World Scientific, Singapore ; Hackensack, NJ (2011), oCLC: ocn708357016. (pages 6, 7, 8, and 18).

[10] M. Lewenstein, A. Sanpera and V. Ahufinger. *Ultracold Atoms in Optical Lattices: Simulating quantum many-body systems*. Oxford University Press (2012). (pages 1 and 8).

[11] D. Tilley and J. Tilley. *Superfluidity and Superconductivity*. Graduate Student Series in Physics. Taylor & Francis (1990). (pages 1, 9, and 100).

[12] M. Boninsegni and N. V. Prokof'ev. *Colloquium: Supersolids: What and where are they?* Rev. Mod. Phys. **84**, 759 (2012). (pages 1 and 38).

[13] A. J. Leggett. *Superfluidity*. Rev. Mod. Phys. **71**, S318 (1999). Publisher: American Physical Society. (pages 1, 81, and 96).

[14] A. F. Andreev and I. M. Lifshitz. *Quantum Theory of Defects in Crystals*. Sov. Phys. JETP 29, 1107 **13** (1969). Publisher: IOP Publishing. (pages 1, 33, and 81).

[15] A. J. Leggett. *Can a Solid Be "Superfluid"?* Phys. Rev. Lett. **25 (22)**, 1543 (1970). (pages 1, 33, 34, 80, 81, 82, 83, 84, 91, 93, 96, 99, 105, and 106).

[16] L. Tanzi, E. Lucioni, F. Famà, J. Catani, A. Fioretti, C. Gabbanini, R. N. Bisset, L. Santos and G. Modugno. *Observation of a Dipolar Quantum Gas with Metastable Supersolid Properties*. Phys. Rev. Lett. **122**, 130405 (2019). (pages 1, 36, 37, 38, 54, 56, 68, 81, 85, 87, and 136).

[17] F. Böttcher, J.-N. Schmidt, M. Wenzel, J. Hertkorn, M. Guo, T. Langen and T. Pfau. *Transient Supersolid Properties in an Array of Dipolar Quantum Droplets*. Phys. Rev. X **9**, 011051 (2019). (pages 36 and 37).

[18] L. Chomaz, D. Petter, P. Ilzhöfer, G. Natale, A. Trautmann, C. Politi, G. Durastante, R. M. W. van Bijnen, A. Patscheider, M. Sohmen, M. J. Mark and F. Ferlaino. *Long-Lived and Transient Supersolid Behaviors in Dipolar Quantum Gases*. Phys. Rev. X **9**, 021012 (2019). (pages 1, 36, 37, 54, and 81).

[19] G. Biagioni, N. Antolini, B. Donelli, L. Pezzè, A. Smerzi, M. Fattori, A. Fioretti, C. Gabbanini, M. Inguscio, L. Tanzi and G. Modugno. Sub-unity superfluid fraction of a supersolid from self-induced josephson effect (2023). (pages 1, 3, 39, 54, 55, 56, 78, 80, 90, 99, 105, 107, and 108).

[20] B. D. Josephson. *Possible new effects in superconductive tunnelling*. Physics Letters **1**, 251 (1962). ISSN 0031-9163. (pages 1, 2, 40, 43, 54, 82, and 85).

[21] A. Barone and G. Paternò. *Physics and Applications of the Josephson Effect*. John Wiley & Sons, London (1982). (pages 1, 2, 40, 95, and 100).

[22] F. Tafuri. *Fundamentals and Frontiers of the Josephson Effect (2019)*. (pages 40, 41, 47, and 48).

[23] The Feynman Lectures on Physics Vol. III Ch. 21: The Schrödinger Equation in a Classical Context: A Seminar on Superconductivity. (pages 1, 42, 46, 49, 55, 60, and 124).

[24] P. W. Anderson. *Considerations on the Flow of Superfluid Helium*. Rev. Mod. Phys. **38**, 298 (1966). (pages 2, 47, and 54).

[25] E. Varoquaux. *Anderson's considerations on the flow of superfluid helium: Some offshoots*. Rev. Mod. Phys. **87**, 803 (2015). (pages 47 and 54).

[26] R. E. Packard. *The role of the Josephson-Anderson equation in superfluid helium*. Rev. Mod. Phys. **70**, 641 (1998). (pages 2 and 47).

[27] A. Smerzi, S. Fantoni, S. Giovanazzi and S. R. Shenoy. *Quantum Coherent Atomic Tunneling between Two Trapped Bose-Einstein Condensates*. Phys. Rev. Lett. **79**, 4950 (1997). (pages 2, 41, 48, 49, 50, 52, 54, 55, 56, 59, 60, 61, 72, 76, 84, 85, 90, and 124).

[28] G. Spagnolli, G. Semeghini, L. Masi, G. Ferioli, A. Trenkwalder, S. Coop, M. Landini, L. Pezzè, G. Modugno, M. Inguscio, A. Smerzi and M. Fattori. *Crossing Over from Attractive to Repulsive Interactions in a Tunneling Bosonic Josephson Junction*. Phys. Rev. Lett. **118**, 230403 (2017). (pages 41, 60, and 76).

[29] M. Albiez, R. Gati, J. Fölling, S. Hunsmann, M. Cristiani and M. K. Oberthaler. *Direct Observation of Tunneling and Nonlinear Self-Trapping*

in a Single Bosonic Josephson Junction. Phys. Rev. Lett. **95**, 010402 (2005). (pages 2, 48, 54, 60, 61, and 85).

[30] X. Gu, A. F. Kockum, A. Miranowicz, Y.-x. Liu and F. Nori. *Microwave photonics with superconducting quantum circuits*. Physics Reports **718–719**, 1–102 (2017). ISSN 0370-1573. (page 2).

[31] G. Wendin. *Quantum information processing with superconducting circuits: a review*. Reports on Progress in Physics **80**, 106001 (2017). ISSN 1361-6633. (page 2).

[32] J. Clarke and A. Braginski. *The SQUID Handbook: Fundamentals and Technology of SQUIDs and SQUID Systems*. Wiley (2006). (pages 2 and 41).

[33] Y.-h. Tang, N. Belecki and J. Mayo-Wells. *A Pratical Josephson Voltage Standard at One Volt*. Special Publication (NIST SP), National Institute of Standards and Technology, Gaithersburg, MD (2001). (pages 2 and 41).

[34] L. Pezzè, K. Xhani, C. Daix, N. Grani, B. Donelli, F. Scazza, D. Hernandez-Rajkov, W. J. Kwon, G. D. Pace and G. Roati. Stabilizing persistent currents in an atomtronic josephson junction necklace (2023). (pages 3, 94, 99, 105, and 108).

[35] G. P. Thomson and A. Reid. *Diffraction of Cathode Rays by a Thin Film*. Nature **119**, 890 (1927). ISSN 1476-4687. (page 5).

[36] W. Ketterle. *Nobel lecture: When atoms behave as waves: Bose-Einstein condensation and the atom laser*. Reviews of Modern Physics **74**, 1131 (2002). (pages 5 and 7).

[37] M. H. Anderson, J. R. Ensher, M. R. Matthews, C. E. Wieman and E. A. Cornell. *Observation of Bose-Einstein Condensation in a Dilute Atomic Vapor*. Science **269**, 198 (1995). ISSN 0036-8075, 1095-9203. (page 7).

[38] K. B. Davis, M. O. Mewes, M. R. Andrews, N. J. van Druten, D. S. Durfee, D. M. Kurn and W. Ketterle. *Bose-Einstein Condensation in a Gas of Sodium Atoms*. Phys. Rev. Lett. **75**, 3969 (1995). (page 7).

[39] E. A. Cornell and C. E. Wieman. *Nobel Lecture: Bose-Einstein condensation in a dilute gas, the first 70 years and some recent experiments*. Rev. Mod. Phys. **74**, 875 (2002). (page 7).

[40] I. Bloch, J. Dalibard and W. Zwerger. *Many-body physics with ultracold gases.* Rev. Mod. Phys. **80**, 885 (2008). (page 8).

[41] L. D. Carr, D. DeMille, R. V. Krems and J. Ye. *Cold and ultracold molecules: science, technology and applications.* New Journal of Physics **11**, 055049 (2009). ISSN 1367-2630. (page 8).

[42] G. Semeghini, G. Ferioli, L. Masi, C. Mazzinghi, L. Wolswijk, F. Minardi, M. Modugno, G. Modugno, M. Inguscio and M. Fattori. *Self-Bound Quantum Droplets of Atomic Mixtures in Free Space.* Phys. Rev. Lett. **120**, 235301 (2018). (pages 8, 26, and 28).

[43] K. Huang and C. N. Yang. *Quantum-Mechanical Many-Body Problem with Hard-Sphere Interaction.* Phys. Rev. **105**, 767 (1957). Publisher: American Physical Society. (page 8).

[44] C. Chin, R. Grimm, P. Julienne and E. Tiesinga. *Feshbach resonances in ultracold gases.* Rev. Mod. Phys. **82**, 1225 (2010). Publisher: American Physical Society. (page 8).

[45] S. Inouye, M. R. Andrews, J. Stenger, H.-J. Miesner, D. M. Stamper-Kurn and W. Ketterle. *Observation of Feshbach resonances in a Bose–Einstein condensate.* Nature **392**, 151–154 (1998). ISSN 1476-4687.

[46] S. L. Cornish, N. R. Claussen, J. L. Roberts, E. A. Cornell and C. E. Wieman. *Stable<mml:math xmlns:mml="http://www.w3.org/1998/Math/MathML" display="inline"><mml:mrow><mml:msup><mml:mrow /><mml:mrow><mml:mn>85</mml:mn></mml:mrow></mml:msup></mml:mrow><mr Einstein Condensates with Widely Tunable Interactions.* Physical Review Letters **85**, 1795–1798 (2000). ISSN 1079-7114.

[47] E. Timmermans. *Feshbach resonances in atomic Bose–Einstein condensates.* Physics Reports **315**, 199–230 (1999). ISSN 0370-1573. (page 8).

[48] P. O. Fedichev, Y. Kagan, G. V. Shlyapnikov and J. T. M. Walraven. *Influence of Nearly Resonant Light on the Scattering Length in Low-Temperature Atomic Gases.* Physical Review Letters **77**, 2913–2916 (1996). ISSN 1079-7114. (page 8).

[49] G. Thalhammer, M. Theis, K. Winkler, R. Grimm and J. H. Denschlag. *Inducing an optical Feshbach resonance via stimulated Raman coupling*. Physical Review A **71** (2005). ISSN 1094-1622.

[50] M. Theis, G. Thalhammer, K. Winkler, M. Hellwig, G. Ruff, R. Grimm and J. H. Denschlag. *Tuning the Scattering Length with an Optically Induced Feshbach Resonance*. Physical Review Letters **93** (2004). ISSN 1079-7114. (page 8).

[51] K. Huang. *Statistical mechanics*. Wiley (1987). (pages 9, 11, and 12).

[52] P. Kapitsa. *Viscosity of Liquid Helium below the -Point*. Nature **141**, 74 (1938). (page 10).

[53] J. F. Allen and A. D. Misener. *Flow of Liquid Helium II*. Nature **141**, 75 (1938). (page 10).

[54] P. Kapitsa. *The Nobel Prize in Physics*. NobelPrize.org (1978). (page 10).

[55] L. Landau. *Theory of the Superfluidity of Helium II*. Phys. Rev. **60**, 356 (1941). (page 10).

[56] C. Raman, M. Köhl, R. Onofrio, D. S. Durfee, C. E. Kuklewicz, Z. Hadzibabic and W. Ketterle. *Evidence for a Critical Velocity in a Bose-Einstein Condensed Gas*. Phys. Rev. Lett. **83**, 2502 (1999). (page 11).

[57] H. Palevsky, K. Otnes and K. E. Larsson. *Excitation of Rotons in Helium II by Cold Neutrons*. Phys. Rev. **112**, 11 (1958). (page 11).

[58] J. L. Yarnell, G. P. Arnold, P. J. Bendt and E. C. Kerr. *Excitations in Liquid Helium: Neutron Scattering Measurements*. Phys. Rev. **113**, 1379 (1959). (page 11).

[59] L. Onsager. *Statistical hydrodynamics*. Il Nuovo Cimento **6**, 279–287 (1949). ISSN 1827-6121. (page 14).

[60] R. Feynman. *Chapter II Application of Quantum Mechanics to Liquid Helium*, 17–53. Elsevier (1955). (page 14).

[61] A. L. Fetter and J. D. Walecka. *Quantum Theory of Many-Particle Systems*. McGraw-Hill, Boston (1971). (pages 15 and 28).

[62] J. Negele and H. Orland. *Quantum many-particle systems.* Frontiers in physics. Addison-Wesley Pub. Co. (1988). (pages 16 and 17).

[63] E. P. Gross. *Structure of a quantized vortex in boson systems.* Il Nuovo Cimento **20 (3)**, 454 (1961). (page 18).

[64] L. P. Pitaevskiĭ. *Vortex lines in an imperfect Bose gas.* Soviet. Phys. JETP **13 (2)**, 451 (1961). (page 18).

[65] N. N. Bogoljubov. *On a new method in the theory of superconductivity.* Il Nuovo Cimento **7**, 794 (1958). (page 21).

[66] T. D. Lee and C. N. Yang. *Many-Body Problem in Quantum Mechanics and Quantum Statistical Mechanics.* Phys. Rev. **105**, 1119 (1957). (page 23).

[67] T. D. Lee, K. Huang and C. N. Yang. *Eigenvalues and Eigenfunctions of a Bose System of Hard Spheres and Its Low-Temperature Properties.* Phys. Rev. **106**, 1135 (1957). (page 23).

[68] C. D'Errico, A. Burchianti, M. Prevedelli, L. Salasnich, F. Ancilotto, M. Modugno, F. Minardi and C. Fort. *Observation of quantum droplets in a heteronuclear bosonic mixture.* Phys. Rev. Res. **1**, 033155 (2019). (page 26).

[69] T. Lahaye, C. Menotti, L. Santos, M. Lewenstein and T. Pfau. *The physics of dipolar bosonic quantum gases.* Reports on Progress in Physics **72**, 126401 (2009). (page 27).

[70] A. R. P. Lima and A. Pelster. *Quantum fluctuations in dipolar Bose gases.* Phys. Rev. A **84**, 041604 (2011). (pages 28, 56, and 57).

[71] A. R. P. Lima and A. Pelster. *Beyond mean-field low-lying excitations of dipolar Bose gases.* Phys. Rev. A **86**, 063609 (2012). (pages 28, 29, 56, and 57).

[72] S. Ronen, D. C. E. Bortolotti, D. Blume and J. L. Bohn. *Dipolar Bose-Einstein condensates with dipole-dependent scattering length.* Phys. Rev. A **74**, 033611 (2006). (page 28).

[73] B. Deb and L. You. *Low-energy atomic collision with dipole interactions.* Phys. Rev. A **64**, 022717 (2001). (page 28).

[74] I. S. Gradshteyn and I. M. Ryzhik. *Table of Integrals, Series, and Products*. Academic Press, New York (2007). (page 29).

[75] M. Schmitt, M. Wenzel, F. Böttcher, I. Ferrier-Barbut and T. Pfau. *Self-bound droplets of a dilute magnetic quantum liquid*. Nature **539**, 259 (2016). (page 30).

[76] I. Ferrier-Barbut, H. Kadau, M. Schmitt, M. Wenzel and T. Pfau. *Observation of Quantum Droplets in a Strongly Dipolar Bose Gas*. Phys. Rev. Lett. **116**, 215301 (2016). (page 30).

[77] L. Santos, G. V. Shlyapnikov and M. Lewenstein. *Roton-Maxon Spectrum and Stability of Trapped Dipolar Bose-Einstein Condensates*. Phys. Rev. Lett. **90**, 250403 (2003). (pages 31 and 35).

[78] D. H. J. O'Dell, S. Giovanazzi and G. Kurizki. *Rotons in Gaseous Bose-Einstein Condensates Irradiated by a Laser*. Phys. Rev. Lett. **90**, 110402 (2003). (pages 31 and 35).

[79] L. Chomaz, R. M. W. van Bijnen, D. Petter, G. Faraoni, S. Baier, J. H. Becher, M. J. Mark, F. Wächtler, L. Santos and F. Ferlaino. *Observation of roton mode population in a dipolar quantum gas*. Nature Physics **14**, 442 (2018). (pages 31, 32, 33, and 68).

[80] O. Penrose and L. Onsager. *Bose-Einstein Condensation and Liquid Helium*. Phys. Rev. **104 (3)**, 576 (1956). (page 33).

[81] H. Matsuda and T. Tsuneto. *Off-Diagonal Long-Range Order in Solids*. Progress of Theoretical Physics Supplement **46**, 411 (1970). (page 34).

[82] W. J. Mullin. *Cell Model of a Bose-Condensed Solid*. Phys. Rev. Lett. **26**, 611 (1971). (page 34).

[83] D. Thouless. *The flow of a dense superfluid*. Annals of Physics **52**, 403 (1969). (page 34).

[84] G. V. Chester. *Speculations on Bose-Einstein Condensation and Quantum Crystals*. Phys. Rev. A **2 (1)**, 256 (1970). (page 34).

[85] E. Kim and M. H. W. Chan. *Probable observation of a supersolid helium phase*. Nature **427**, 225– (2004). (pages 34 and 39).

[86] E. Kim and M. H. W. Chan. *Observation of Superflow in Solid Helium.* Science **305**, 1941 (2004). (pages 34 and 39).

[87] J. Day and J. Beamish. *Low-temperature shear modulus changes in solid 4He and connection to supersolidity.* Nature **450**, 853– (2007). (page 35).

[88] D. Y. Kim and M. H. W. Chan. *Absence of Supersolidity in Solid Helium in Porous Vycor Glass.* Phys. Rev. Lett. **109**, 155301 (2012). (page 35).

[89] K. Baumann, C. Guerlin, F. Brennecke and T. Esslinger. *Dicke quantum phase transition with a superfluid gas in an optical cavity.* Nature **464**, 1301 (2010). (page 35).

[90] J. R. Li, J. Lee, W. Huang, S. Burchesky, B. Shteynas, F. Ç. Top, A. O. Jamison and W. Ketterle. *A stripe phase with supersolid properties in spin–orbit-coupled Bose–Einstein condensates.* Nature **543**, 91 (2017). (page 35).

[91] J. Léonard, A. Morales, P. Zupancic, T. Esslinger and T. Donner. *Supersolid formation in a quantum gas breaking a continuous translational symmetry.* Nature **543**, 87 (2017). (page 35).

[92] G. Natale, R. M. W. van Bijnen, A. Patscheider, D. Petter, M. J. Mark, L. Chomaz and F. Ferlaino. *Excitation Spectrum of a Trapped Dipolar Supersolid and Its Experimental Evidence.* Phys. Rev. Lett. **123**, 050402 (2019). (page 38).

[93] M. Guo, F. Böttcher, J. Hertkorn, J.-N. Schmidt, M. Wenzel, H. P. Büchler, T. Langen and T. Pfau. *The low-energy Goldstone mode in a trapped dipolar supersolid.* Nature **574**, 386 (2019). (pages 38 and 81).

[94] L. Tanzi, S. M. Roccuzzo, E. Lucioni, F. Famà, A. Fioretti, C. Gabbanini, G. Modugno, A. Recati and S. Stringari. *Supersolid symmetry breaking from compressional oscillations in a dipolar quantum gas.* Nature **574**, 382 (2019). (pages 38, 39, and 81).

[95] L. Tanzi, J. G. Maloberti, G. Biagioni, A. Fioretti, C. Gabbanini and G. Modugno. *Evidence of superfluidity in a dipolar supersolid from nonclassical rotational inertia.* Science **371**, 1162–1165 (2021). ISSN 1095-9203. (pages 39, 56, and 82).

[96] M. A. Norcia, E. Poli, C. Politi, L. Klaus, T. Bland, M. J. Mark, L. Santos, R. N. Bisset and F. Ferlaino. *Can angular oscillations probe superfluidity in dipolar supersolids?* Phys. Rev. Lett. **129**, 040403 (2022). (pages 39 and 82).

[97] S. M. Roccuzzo, A. Recati and S. Stringari. *Moment of inertia and dynamical rotational response of a supersolid dipolar gas.* Phys. Rev. Lett. **105**, 023316 (2022). (pages 39 and 82).

[98] S. V. Pereverzev, A. Loshak, S. Backhaus, J. C. Davis and R. E. Packard. *Quantum oscillations between two weakly coupled reservoirs of superfluid 3He.* Nature **388**, 449 (1997). (page 41).

[99] F. M. Araujo-Moreira. *Josephson Junction, the Quantum Engine: from S.QU.I.D. Sensors to Qubits for Quantum Computers.* RDMS **18** (2023). ISSN 25768840. (page 41).

[100] F. M Araujo Moreira. *Quantum Technologies and the Engineering of Josephson JunctionBased Sensors: Disruptive Innovation as a Strategic Differential for National Security and Defense.* Current Trends in Eng Sc **4**, 1 (2023). (page 41).

[101] C. Kittel. *Introduction to solid state physics.* Wiley, Hoboken, NJ, 8th ed edition (2005). (page 42).

[102] S. Shapiro. *Josephson Currents in Superconducting Tunneling: The Effect of Microwaves and Other Observations.* Phys. Rev. Lett. **11**, 80 (1963). (page 44).

[103] T. Zibold, E. Nicklas, C. Gross and M. K. Oberthaler. *Classical Bifurcation at the Transition from Rabi to Josephson Dynamics.* Phys. Rev. Lett. **105**, 204101 (2010). (page 48).

[104] S. Raghavan, A. Smerzi, S. Fantoni and S. R. Shenoy. *Coherent oscillations between two weakly coupled Bose-Einstein condensates: Josephson effects, π oscillations, and macroscopic quantum self-trapping.* Phys. Rev. A **59**, 620 (1999). (pages 49, 54, and 59).

[105] I. Zapata, F. Sols and A. J. Leggett. *Josephson effect between trapped Bose-Einstein condensates.* Phys. Rev. A **57**, R28 (1998). (pages 49, 84, 99, and 105).

[106] S. M. Roccuzzo and F. Ancilotto. *Supersolid behavior of a dipolar Bose-Einstein condensate confined in a tube*. Physical Review A **99** (2019). (pages 54 and 56).

[107] P. Ilzhöfer, M. Sohmen, G. Durastante, C. Politi, A. Trautmann, G. Morpurgo, T. Giamarchi, L. Chomaz, M. J. Mark and F. Ferlaino. Phase coherence in out-of-equilibrium supersolid states of ultracold dipolar atoms (2019). (page 54).

[108] M. Abad, M. Guilleumas, R. Mayol, M. Pi and D. M. Jezek. *A dipolar self-induced bosonic Josephson junction*. EPL (Europhysics Letters) **94**, 10004 (2011). (page 55).

[109] D. S. Petrov. *Quantum Mechanical Stabilization of a Collapsing Bose-Bose Mixture*. Phys. Rev. Lett. **115**, 155302 (2015). (page 56).

[110] S. Roccuzzo, A. Gallemí, A. Recati and S. Stringari. *Rotating a Supersolid Dipolar Gas*. Physical Review Letters **124** (2020). (page 56).

[111] G. Biagioni, N. Antolini, A. Alaña, M. Modugno, A. Fioretti, C. Gabbanini, L. Tanzi and G. Modugno. *Dimensional Crossover in the Superfluid-Supersolid Quantum Phase Transition*. Physical Review X **12** (2022). (pages 56, 69, and 85).

[112] S. Levy, E. Lahoud, I. Shomroni and J. Steinhauer. *The a.c. and d.c. Josephson effects in a Bose–Einstein condensate*. Nature **449**, 579 (2007). (page 60).

[113] S. A. Chin and E. Krotscheck. *Fourth-order algorithms for solving the imaginary - time Gross-Pitaevskii equation in a rotating anisotropic trap*. Phys. Rev. E **72**, 036705 (2005). (page 63).

[114] L. Lehtovaara, J. Toivanen and J. Eloranta. *Solution of time-independent Schrödinger equation by the imaginary time propagation method*. Journal of Computational Physics **221**, 148 (2007). (pages 64 and 65).

[115] P. Luukko and E. Räsänen. *Imaginary time propagation code for large-scale two-dimensional eigenvalue problems in magnetic fields*. Computer Physics Communications **184**, 769 (2013).

[116] P. Bader, S. Blanes and F. Casas. *Solving the Schrödinger eigenvalue problem by the imaginary time propagation technique using splitting methods with complex coefficients.* The Journal of Chemical Physics **139**, 124117 (2013). (page 63).

[117] G. C. Wick. *Properties of Bethe-Salpeter Wave Functions.* Phys. Rev. **96**, 1124 (1954). (page 63).

[118] Convolution theorem. (page 67).

[119] A. Alaña, N. Antolini, G. Biagioni, I. L. Egusquiza and M. Modugno. *Crossing the superfluid-supersolid transition of an elongated dipolar condensate.* Physical Review A **106** (2022). (page 69).

[120] A. J. Leggett. *On the superfluid fraction of an arbitrary many-body system at $T = 0$.* J. Stat. Phys **93**, 927 (1998). (pages 80, 84, 91, 96, 99, 105, and 106).

[121] E. P. Gross. *Unified theory of interacting bosons.* Phys. Rev. **106**, 161 (1957). (page 81).

[122] G. V. Chester. *Speculations on Bose–Einstein condensation and quantum crystals.* Phys. Rev. A **2**, 256 (1970). (page 81).

[123] J. Nyéki, A. Phillis, A. Ho, D. Lee, P. Coleman, J. Parpia, B. Cowan and J. Saunders. *Intertwined superfluid and density wave order in two-dimensional 4He.* Nat. Phys. **13**, 455 (2017). (pages 81, 82, and 93).

[124] J. Choi, A. A. Zadorozhko, J. Choi and E. Kim. *Spatially modulated superfluid state in two-dimensional 4He films.* Phys. Rev. Lett. **127**, 1 (2021). (pages 81, 82, and 93).

[125] J. Léonard, A. Morales, P. Zupancic, T. Esslinger and T. Donner. *Supersolid formation in a quantum gas breaking a continuous translational symmetry.* Nature **543**, 87 (2017). (page 81).

[126] J.-R. Li, J. Lee, W. Huang, S. Burchesky, B. Shteynas, F. Ç. Top, A. O. Jamison and W. Ketterle. *A stripe phase with supersolid properties in spin–orbit-coupled Bose–Einstein condensates.* Nature **543**, 91 (2017). (page 81).

[127] M. A. Norcia, C. Politi, L. Klaus, M. Sohmen, M. J. Mark, R. N. Bisset, L. Santos and F. Ferlaino. *Two-dimensional supersolidity in a dipolar quantum gas.* Nature **596**, 357 (2021). (page 81).

[128] L. V. Levitin, B. Yager, L. Sumner, B. Cowan, A. J. Casey, J. Saunders, N. Zhelev, R. G. Bennett and J. M. Parpia. *Evidence for a spatially modulated superfluid phase of 3He under confinement.* Phys. Rev. Lett. **122**, 085301 (2019). (page 81).

[129] A. J. Shook, V. Vadakkumbatt, P. S. Yapa, C. Doolin, R. Boyack, P. H. Kim, G. G. Popowich, F. Souris, H. Christani, J. Maciejko and J. P. Davis. *Stabilized pair density wave via nanoscale confinement of superfluid 3He.* Phys. Rev. Lett. **124**, 015301 (2020). (page 81).

[130] M. H. Hamidian, S. D. Edkins, S. H. Joo, A. Kostin, H. Eisaki, S. Uchida, M. J. Lawler, E.-A. Kim, A. P. Mackenzie, K. Fujita, J. Lee and J. C. S. Davis. *Detection of a Cooper-pair density wave in Bi2Sr2CaCu2O8+x.* Nature **532**, 343 (2016). (pages 81 and 93).

[131] Y. Liu, T. Wei, G. He, Y. Zhang, Z. Wang and J. Wang. *Pair density wave state in a monolayer high-Tc iron-based superconductor.* Nature **618**, 934 (2023).

[132] D. F. Agterberg, J. C. S. Davis, S. D. Edkins, E. Fradkin, D. J. V. Harlingen, S. A. Kivelson, P. A. Lee, L. Radzihovsky, J. M. Tranquada and Y. Wang. *The physics of pair density waves: cuprate superconductors and beyond.* Annual Review of Condensed Matter Physics **11**, 231 (2020). (pages 81 and 93).

[133] C. J. Pethick, N. Chamel and S. Reddy. *Superfluid dynamics in neutron star crusts.* Progress of Theoretical Physics Supplement **186**, 9 (2010). (page 81).

[134] S. Conti, A. Perali, A. R. Hamilton, M. V. Milošević, F. M. Peeters and D. Neilson. *Chester supersolid of spatially indirect excitons in double-layer semiconductor heterostructures.* Phys. Rev. Lett. **130**, 057001 (2023). (page 81).

[135] A. Gallemì, S. M. Roccuzzo, S. Stringari and A. Recati. *Quantized vortices in dipolar supersolid Bose-Einstein-condensed gases.* Phys. Rev. A **102**, 023322 (2020). (pages 82 and 93).

[136] M. N. Tengstrand, D. Boholm, R. Sachdeva, J. Bengtsson and S. M. Reimann. *Persistent currents in toroidal dipolar supersolids.* Phys. Rev. A **103**, 013313 (2021). (page 93).

[137] G. Biagioni. *Evidence of superfluidity in a dipolar supersolid.* Il Nuovo Cimento **44 C**, 121 (2021). (page 82).

[138] L. Landau. *Theory of the superfluidity of helium II.* Phys. Rev. **60**, 356 (1941). (page 82).

[139] I. Božović, X. He, J. Wu and A. T. Bollinger. *Dependence of the critical temperature in overdoped copper oxides on superfluid density.* Nature **536**, 309 (2016). (page 82).

[140] M. E. Fisher, M. N. Barber and D. Jasnow. *Helicity modulus, superfluidity, and scaling in isotropic systems.* Phys. Rev. A **8**, 1111 (1973). (page 83).

[141] F. S. Cataliotti, S. Burger, C. Fort, P. Maddaloni, F. Minardi, A. Trombettoni, A. Smerzi and M. Inguscio. *Josephson junction arrays with Bose-Einstein condensates.* Science **293**, 843 (2001). (pages 85, 93, and 95).

[142] S. Levy, E. Lahoud, I. Shomroni and J. Steinhauer. *The a.c. and d.c Josephson effects in a Bose–Einstein condensate,.* Nature **449**, 579 (2007).

[143] G. Valtolina, A. Burchianti, A. Amico, E. Neri, K. Xhani, J. A. Seman, A. Trombettoni, A. Smerzi, M. Zaccanti, M. Inguscio and G. Roati. *Josephson effect in fermionic superfluids across the BEC-BCS crossover.* Science **350**, 6267 (2015). (page 85).

[144] J. Tao, M. Zhao and I. B. Spielman. Observation of anisotropic superfluid density in an artificial crystal. (page 93).

[145] G. Chauveau, C. Maury, F. Rabec, C. Heintze, G. Brochier, S. Nascimbene, J. Dalibard, J. Beugnon, S. M. Roccuzzo and S. Stringari. *Superfluid fraction in an interacting spatially modulated Bose-Einstein condensate.* Phys. Rev. Lett. **130**, 3 (2023). (page 93).

[146] T. Berrada, S. van Frank, R. B"ucker, T. Schumm, J.-F. Schaff and J. Schmiedmayer. *Integrated Mach-Zehnder interferometer for Bose-Einstein condensates.* Nat Comm **4**, 2077 (2013). (page 93).

[147] R. Gati, B. Hemmerling, J. Fo¨lling, M. Albiez and M. K. Oberthaler. *Noise thermometry with two weakly coupled Bose-Einstein condensates.* Phys. Rev. Lett. **96**, 4 (2006). (page 93).

[148] L. Pezzè, A. Smerzi, M. K. Oberthaler, R. Schmied and P. Treutlein. *Quantum metrology with nonclassical states of atomic ensembles.* Rev Mod Phys **90**, 035005 (2018). (page 93).

[149] Q. You and F. Nori. *Superconducting Circuits and Quantum Information.* Physics Today **58**, 42 (2005). (page 95).

[150] J. Clarke and F. K. Wilhelm. *Superconducting quantum bits.* Nature **453**, 1031 (2008).

[151] H. Devoret and R. J. Schoelkopf. *Superconducting circuits for quantum information: An outlook.* Science **339**, 1169 (2013).

[152] M. Kjaergaard, M. E. Schwartz, J. B. üller, P. Krantz, J. I.-J. Wang, S. Gustavsson and W. D. Oliver. *Superconducting qubits: Current state of play.* Annual Review of Condensed Matter Physics **11**, 369 (2020).

[153] S. Rasmussen, K. Christensen, S. Pedersen, L. Kristensen, T. Bækkegaard, N. Loft and N. Zinner. *Superconducting circuit companion — an introduction with worked examples.* PRX Quantum **2**, 040204 (2021). (page 95).

[154] K. Jain, K. K. Likharev, J. E. Lukens and J. E. Sauvageau. *Mutual phase-locking in Josephson junction arrays.* Physics Reports **109**, 309 (1984). (page 95).

[155] K. Wiesenfeld, P. Colet and S. H. Strogatz. *Frequency locking in Josephson arrays: Connection with the kuramoto model.* Phys. Rev. E **57**, 1563 (1998).

[156] V. M. Vinokur, T. I. Baturina, M. V. Fistul, A. Y. Mironov, M. R. Baklanov and C. Strunk. *Superinsulator and quantum synchronization.* Nature **452**, 613 (2008).

[157] S. Y. Grebenchuk, R. Cattaneo and V. M. Krasnov. *Nonlocal long-range synchronization of planar Josephson-junction arrays.* Phys. Rev. Appl **17**, 064032 (2022). (page 95).

[158] B. P. Anderson and M. A. Kasevich. *Macroscopic quantum interference from atomic tunnel arrays.* Science **282**, 1686 (1998). (page 95).

[159] L. B. Ioffe, M. V. Feigel'man, A. Ioselevich, D. Ivanov, M. Troyer and G. Blatter. *Topologically protected quantum bits using Josephson junction arrays.* Nature **415**, 503 (2002). (page 95).

[160] H. Hilgenkamp and J. Mannhart. *Grain boundaries in high-Tc superconductors.* Rev. Mod. Phys **74**, 485 (2002). (page 95).

[161] F. Tafuri and J. R. Kirtley. *Weak links in high critical temperature superconductors.* Rep. Prog. Phys **68**, 2573 (2005). (page 95).

[162] J. Clarke and A. I. Braginski. *The SQUID Handbook.* John Wiley & Sons, London (2004). (page 95).

[163] R. L. Fagaly. *Superconducting quantum interference device instruments and applications.* Rev. Sci. Instrum **77**, 101101 (2006). (page 95).

[164] K. Schwab, N. Bruckner and R. E. Packard. *Detection of the earth's rotation using superfluid phase coherence.* Nature **386**, 585 (1997). (page 95).

[165] Y. Sato and R. E. Packard. *Superfluid helium quantum interference devices: physics and applications.* Rep. Prog. Phys **75**, 016401 (2011). (page 95).

[166] R. C. Jaklevic, J. Lambe, A. H. Silver and J. E. Mercereau. *Quantum interference effects in Josephson tunneling.* Phys. Rev. Lett **12**, 159 (1964). (page 95).

[167] L. Amico, A. Osterloh and F. Cataliotti. *Quantum many particle systems in ring-shaped optical lattices.* Phys. Rev. Lett **95**, 063201 (2005). (page 95).

[168] B. T. Seaman, M. Krämer, D. Z. Anderson and M. J. Holland. *Atomtronics: Ultracold-atom analogs of electronic devices.* Phys. Rev. A **75**, 023615 (2007).

[169] L. Amico. *et al., "Roadmap on atomtronics: State of the art and perspective".* AVS Quantum Science **3**, 039201 (2021). (page 96).

[170] L. Amico, D. Anderson, M. Boshier, J.-P. Brantut, L.-C. Kwek, A. Minguzzi and W. von Klitzing. *Atomtronic circuits: From many-body physics to quantum technologies.* Rev. Mod. Phys **94**, 041001 (2022). (page 95).

[171] A. Ramanathan, K. C. Wright, S. R. Muniz, M. Zelan, W. T. Hill, C. J. Lobb, K. Helmerson, W. D. Phillips and G. K. Campbell. *Superflow in a toroidal Bose-Einstein condensate: An atom circuit with a tunable weak link.* Phys. Rev. Lett **106**, 130401 (2011). (pages 95 and 97).

[172] S. Moulder, S. Beattie, R. P. Smith, N. Tammuz and Z. Hadzibabic. *Quantized supercurrent decay in an annular Bose-Einstein condensate.* Phys. Rev. A **86**, 013629 (2012). (page 97).

[173] Y. Cai, D. G. Allman, P. Sabharwal and K. C. Wright. *Persistent currents in rings of ultracold fermionic atoms.* Phys. Rev. Lett **128**, 150401 (2022). (page 107).

[174] G. D. Pace, K. Xhani, A. M. Falconi, M. Fedrizzi, N. Grani, D. H. Rajkov, M. Inguscio, F. Scazza, W. Kwon and G. Roati. *Imprinting persistent currents in tunable fermionic rings.* Phys. Rev. X **12**, 041037 (2022). (pages 95, 97, 103, and 107).

[175] K. C. Wright, R. B. Blakestad, C. J. Lobb, W. D. Phillips and G. K. Campbell. *Driving phase slips in a superfluid atom circuit with a rotating weak link.* Phys. Rev. Lett **110**, 025302 (2013). (pages 95 and 100).

[176] K. C. Wright, R. B. Blakestad, C. J. Lobb, W. D. Phillips and G. K. Campbell. *Threshold for creating excitations in a stirred superfluid ring.* Phys. Rev. A **88**, 063633 (2013).

[177] J. Polo, R. Dubessy, P. Pedri, H. Perrin and A. Minguzzi. *Oscillations and decay of superfluid currents in a one-dimensional Bose gas on a ring.* Phys. Rev. Lett **123**, 195301 (2019). (page 95).

[178] S. Eckel, F. Jendrzejewski, A. Kumar, C. J. Lobb and G. K. Campbell. *Interferometric measurement of the current-phase relationship of a superfluid weak link.* Phys. Rev. X **4**, 031052 (2014). (pages 95 and 103).

[179] S. Eckel, J. G. Lee, F. Jendrzejewski, N. Murray, C. W. Clark, C. J. Lobb, W. D. Phillips, M. Edwards and G. K. Campbell. *Hysteresis in a quantized superfluid 'atomtronic' circuit.* Nature **506**, 200 (2014). (page 95).

[180] G. Watanabe, F. Dalfovo, F. Piazza, L. P. Pitaevskii and S. Stringari. *Critical velocity of superfluid flow through single-barrier and periodic potentials.* Phys. Rev. A **80**, 053602 (2009). (page 95).

[181] F. Piazza, L. A. Collins and A. Smerzi. *Vortex-induced phase-slip dissipation in a toroidal Bose-Einstein condensate flowing through a barrier.* Phys. Rev. A **80**, 021601 (2009).

[182] F. Piazza, L. A. Collins and A. Smerzi. *Current-phase relation of a Bose-Einstein condensate flowing through a weak link.* Phys. Rev. A **81**, 033613 (2010).

[183] R. Dubessy, T. Liennard, P. Pedri and H. Perrin. *Critical rotation of an annular superfluid Bose-Einstein condensate.* Phys. Rev. A **86**, 011602 (2012).

[184] Z. Mehdi, A. S. Bradley, J. J. Hope and S. S. Szigeti. *Superflow decay in a toroidal Bose gas: The effect of quantum and thermal fluctuations.* SciPost Phys **11**, 080 (2021).

[185] A. M. noz Mateo, A. Gallemí, M. Guilleumas and R. Mayol. *Persistent currents supported by solitary waves in toroidal Bose-Einstein condensates.* Phys. Rev. A **91**, 063625 (2015). (page 100).

[186] A. Pérez-Obiol and T. Cheon. *Bose-Einstein condensate confined in a one-dimensional ring stirred with a rotating delta link.* Phys. Rev. E **101**, 022212 (2020). (page 100).

[187] K. Xhani, G. D. Pace, F. Scazza and G. Roati. *Decay of persistent currents in annular atomic superfluids.* Atoms **11**, 109 (2023). (pages 95 and 103).

[188] C. Ryu, P. W. Blackburn, A. A. Blinova and M. G. Boshier. *Experimental realization of Josephson junctions for an atom squid.* Phys. Rev. Lett **111**, 205301 (2013). (page 95).

[189] F. Jendrzejewski, S. Eckel, N. Murray, C. Lanier, M. Edwards, C. J. Lobb and G. K. Campbell. *Resistive flow in a weakly interacting Bose-Einstein condensate.* Phys. Rev. Lett **113**, 045305 (2014). (page 95).

[190] C. Ryu, E. C. Samson and M. G. Boshier. *Quantum interference of currents in an atomtronic squid.* Nat. Comm **11**, 3338 (2020). (page 95).

[191] R. Feynman, R. B. Leighton and M. Sands. *The Feynman Lectures on Physics, Volume III.* Addison–Wesley, London Ch. 21. Available online at (2005). (page 96).

[192] A. Y. Meltzer, A. Uri and E. Zeldov. *Multi-terminal multi-junction dc SQUID for nanoscale magnetometry.* Supercond. Sci. Technol **29**, 114001 (2016). (page 96).

[193] A. Uri, A. Y. Meltzer, Y. Anahory, L. Embon, E. O. Lachman, D. Halbertal, N. Hr, Y. Myasoedov, M. E. Huber, A. F. Young and E. Zeldov. *Electrically tunable multiterminal SQUID-on-tip.* Nano Lett **16**, 6910 (2016).

[194] S. Wolter, J. Linek, T. Weimann, D. Koelle, R. Kleiner and O. Kieler. *Static and dynamic transport properties of multi-terminal, multi-junction microSQUIDs realized with nb/HfTi/nb Josephson junctions.* Supercond. Sci. Technol **35**, 085006 (2022).

[195] A. Zagoskin. *Quantum engineering of superconducting structures: Principles, promise and problems.* Low Temp. Phys **43**, 751 (2017).

[196] V. K. Kornev, N. V. Kolotinskiy, A. V. Sharafiev, I. I. Soloviev and O. A. Mukhanov. *From single SQUID to superconducting quantum arrays.* Low Temp. Phys **43**, 829 (2017). (page 96).

[197] G. Gauthier, I. Lenton, N. M. Parry, M. Baker, M. J. Davis, H. Rubinsztein-Dunlop and T. W. Neely. *Direct imaging of a digital-micromirror device for configurable microscopic optical potentials.* Optica **3**, 1136 (2016). (page 96).

[198] P. Zupancic, P. M. Preiss, R. Ma, A. Lukin, M. E. Tai, M. Rispoli, R. Islam and M. Greiner. *Ultra-precise holographic beam shaping for microscopic quantum control.* Opt. Express **24**, 13881 (2016).

[199] N. Navon, R. P. Smith and Z. Hadzibabic. *Quantum gases in optical boxes.* Nature Physics **17**, 1334 (2021). (page 96).

[200] A. Nunnenkamp, A. M. Rey and K. Burnett. *Generation of macroscopic superposition states in ring superlattices.* Phys. Rev. A **77**, 023622 (2008). (pages 96 and 107).

[201] D. Solenov and D. Mozyrsky. *Metastable states and macroscopic quantum tunneling in a cold-atom Josephson ring.* Phys. Rev. Lett **104**, 150405 (2010).

[202] C. Schenke, A. Minguzzi and F. W. J. Hekking. *Nonadiabatic creation of macroscopic superpositions with strongly correlated one-dimensional bosons in a ring trap.* Phys. Rev. A **84**, 053636 (2011).

[203] D. W. Hallwood and J. Brand. *Engineering mesoscopic superpositions of superfluid flow.* Phys. Rev. A **84**, 043620 (2011).

[204] L. Amico, D. Aghamalyan, F. Auksztol, H. Crepaz, R. Dumke and L. C. Kwek. *Superfluid qubit systems with ring shaped optical lattices.* Sci. Rep **4**, 4298 (2014). (pages 96 and 107).

[205] A. L. Fetter. *Low-lying superfluid states in a rotating annulus.* Phys. Rev **153**, 285 (1967). (page 96).

[206] F. Bloch. *Superfluidity in a ring.* Phys. Rev. A **7**, 2187 (1973). (page 96).

[207] J. D. Reppy and D. Depatie. *Persistent Currents in Superfluid Helium.* Phys. Rev. Lett **12**, 187 (1964). (page 97).

[208] J. D. Reppy. *Superfluid helium in porous media.* J. Low. Temp. Phys **87**, 205 (1992). (page 97).

[209] C. Ryu, M. F. Andersen, P. Cladè, V. Natarajan, K. Helmerson and W. D. Phillips. *Observation of persistent flow of a Bose-Einstein condensate in a toroidal trap.* Phys. Rev. Lett **99**, 260401 (2007). (page 97).

[210] S. Beattie, S. Moulder, R. J. Fletcher and Z. Hadzibabic. *Persistent currents in spinor condensates.* Phys. Rev. Lett **110**, 025301 (2013).

[211] A. Kumar, R. Dubessy, T. Badr, C. D. Rossi, M. de Goër de Herve, L. Longchambon and H. Perrin. *Producing superfluid circulation states using phase imprinting.* Phys. Rev. A **97**, 043615 (2018). (pages 97 and 103).

[212] G. Chauveau, C. Maury, F. Rabec, C. Heintze, G. Brochier, S. Nascimbene, J. Dalibard, J. Beugnon, S. M. Roccuzzo and S. Stringari. *Superfluid fraction in an interacting spatially modulated Bose-Einstein condensate.* Phys. Rev. Lett **130**, 226003 (2023). (pages 99 and 105).

[213] J. Tao, M. Zhao and I. B. Spielman. *Observation of anisotropic superfluid density in an artificial crystal.* Phys. Rev. Lett **131**, 163401 (2023). (pages 99 and 105).

[214] L. Corman, L. Chomaz, T. Bienaimé, R. Desbuquois, C. Weitenberg, S. Nascimbène, J. Dalibard and J. Beugnon. *Quench-induced supercurrents in an annular Bose gas.* Phys. Rev. Lett **113**, 135302 (2014). (page 103).

[215] W. J. Kwon, G. D. Pace, R. Panza, M. Inguscio, W. Zwerger, M. Zaccanti, F. Scazza and G. Roati. *Strongly correlated superfluid order parameters from dc Josephson supercurrents.* Science **369**, 84 (2020). (pages 106 and 107).

[216] M. N. Tengstrand, D. Boholm, R. Sachdeva, J. Bengtsson and S. M. Reimann. *Persistent currents in toroidal dipolar supersolids.* Phys. Rev. A **103**, 013313 (2021). (page 107).

[217] G. Wlazłowski, K. Xhani, M. Tylutki, N. P. Proukakis and P. Magierski. *Dissipation mechanisms in fermionic Josephson junction.* Phys. Rev. Lett **130**, 023003 (2023). (page 107).

[218] L. Pisani, V. Piselli and G. C. Strinati. Critical current throughout the bcs-bec crossover with the inclusion of pairing fluctuations. (page 107).

[219] D. Ananikian and T. Bergeman. *Gross-Pitaevskii equation for Bose particles in a double-well potential: Two-mode models and beyond.* Phys. Rev. A **73**, 013604 (2006). (page 114).

[220] C. Runge. *Ueber die numerische Auflösung von Differentialgleichungen.* Mathematische Annalen **46**, 167 (1895). (page 132).

[221] W. Kutta. *Beitrag zur näherungsweisen Integration totaler Differentialgleichungen.* Zeit. Math. Phys. **46**, 435 (1901). (page 132).